POLITECNIOCO DI TORINO

Master's Degree in Electronic Engineering

Master's Degree Thesis

Body-Coupled Communication for Microscale Implants In Human Brain

Supervisors

Prof. Danilo DEMARCHI

Ph.D. Amin RASHIDI (TU Delft)

Candidate

Matteo POLA

April 2023

Abstract

This thesis investigates the application of body-coupled communication (BCC) for microscale implants inside the human brain. Brain-Computer Interface (BCI) platforms have received a lot of attention in the last decades, demonstrating to be an effective means of restoring sensory and motor functions (e.g. sight, movement, and cognitive abilities), in addition to their utility in neuroscience studies. Developing technologies to enable distributed massive neural interfaces is an active area of research to enhance the efficiency and efficacy of BCI systems. To this end, both wired solutions (e.g. Neuralink project), and wireless networks of micro-scale implants are explored. Most wireless solutions utilize far-field electromagnetic radiation, i.e. RF, for communications between implants. Alternatively, this thesis explores BCC as a promising technology for communication between distributed micro-scale implants. BCC intrinsically offers lower power consumption, higher efficiency, low interference, and higher security compared to RF solutions. In this thesis, the applicability of galvanic BCC is investigated, which is one of the popular BCC methods that involves coupling a rather low-frequency differential signal directly to the body through a pair of electrodes. Since the BCC transmission efficiency is highly dependent on the system's geometries and the electromagnetic properties of the tissue, finite element models (FEM) in COMSOL Multiphysics are heavily employed in this thesis. This enables the study of the impact of various parameters such as electrode size and orientation, implant location, operating frequency, and the number of devices in a network of miniaturized implants. FEM simulations revealed that for an electrode size of 200 um, the highest power gain can be achieved at frequencies above 50 MHz, which has a good margin to the model's validity limit. Thus, this thesis presents some noteworthy findings all at 50 MHz frequency. Firstly, concurrently scaling the inter-electrode distance in implants ("D_e"), channel length ("L_c", distance between two implants) and electrodes' dimension with a constant ratio, revealed that the voltage gain ("G_v") decreases from around -37 dB to -47 dB as D_e is reduced from 5 cm to 1 mm. This suggests that scaling of BCC for a network of micro-scale implants comes at the cost of more power consumption or a more sensitive receiver, but it is at an affordable level. Next, keeping D_e constant at 1 mm, as L_c is increased from 2 mm to 5 cm, G_v drops exponentially from about -47 dB to -120 dB due to the natural decay of the electric field intensity in the near-field region. On the other hand, increasing D_e from 0.5 mm to 2 mm, while maintaining L_c at 5 mm, leads to a rise in G_v from approximately -81 dB to -59 dB. Additionally, the study has found that the BCC design demonstrates good robustness against misalignment. An angular misalignment of up to 60 °, and a lateral displacement of up to 1 mm result in the maximum G_v attenuation of less than 5 dB, and 2 dB, respectively. Furthermore, the thesis covers a discussion on the frequency-dependent behavior of each tissue, the polarization impedance around the electrodes, the devices' equivalent circuits, and quasi-static approximation analysis. Based on the results obtained, the trade-offs between gain, maximum frequency and data rate, input impedance, and safety implications are explored and discussed.

Acknowledgements

ACKNOWLEDGMENTS

"HI"
Goofy, Google by Google

Table of Contents

List of Tables

List of Figures

Acronyms

BCC
: body-coupled communication

ICNIRP
: International Commission On Non-Ionizing Radiation Protection

SAR
: specific absorption rate

FEM
: finite element mmethod

RMS
: root mean square

ES
: electrostimulation

EPI
: electrode polarization impedance

BCI
: Brain-Computer Interface

RF
: radio-frequency

PAN
: personal area network

WBAN

wireless body area network

BMI

Brain-Machine Interface

DBS

deep brain stimulation

Chapter 1

Introduction

Brain-Computer Interface (BCI) is one of the most active and exciting fields of research nowadays and it is expanding with many different techniques, like invasive Brain-Machine Interface (BMI), Deep Brain Stimulation (DBS), distributed neural platforms, etc. Not only it is used to study the still hidden mechanisms of the human brain and biomedical signals but also it is already demonstrated effective in a lot of medical applications improving the quality of life of the patient affected by serious diseases. The successful implementations vary among the recording of detailed EEG signals and various neural potentials, treatment of Parkinson, Epilepsy, and Alzheimer, chronic pain and psychological disorders relief, interfacing with computers, controlling arms after paralysis or prosthetics, and restoring partial sensory functions like sight and touch.
The trend already moved from external devices that record with low resolution to invasive implanted platforms in direct contact with the brain cortex, capable of recording and stimulating with precision. Important steps have been made in the sector, but they presented new challenges. The need for small devices, high-resolution arrays of electrodes, connection with external apparatus, and limited invasiveness is fundamental in the most recent advances. One possible solution to the new requirements is represented by distributed neural platforms, consisting of several independent devices spread over a large portion of the brain and connected in a network. This method allows for greater insight and control over specific areas of the brain, making major progress impossible beforehand. Wired solutions have been proposed, but they have additional disadvantages such as the risk of infection and damage to tissue that is unable to heal after surgery, together with limited depth. Making stand-alone network components completely wireless both in terms of communication and power delivery is becoming a reality and it is very promising as the natural evolution of BCI systems. This leads to the concept of a wireless network of micro-scale implantable devices, capable of deeper locations, higher density, and less damage. It also includes the limits of very constrained power

and volume for implementing such a platform, which a RF implementation is not always able to respect due to the high complexity and the frequency-size trade-off given by the antennas.
Body-coupled communication (BCC) is an innovative wireless technology that is trying to propose a new approach for implantable and wearable devices, with low power, absence of antennas and low attenuation through the body. Even if BCC has not already been successfully applied to a network of several devices, this thesis has the scope of an investigation of its use in the BCI scenario.

1.1 State Of The Art And Challenges

In the area of distributed neural platforms, some remarkable projects are Neural Dust ([1]), Micreobead ([2]), Neuralink ([3]), and Neurograin ([4]). Neural Dust has been presented as able to massive scale the number of neural recordings in the brain cortex thanks to thousands of nodes with ultrasonic power and communication link. The application then moved to single devices on the peripheral nerves due to the too large dimensions. The strength of Neuralink is to provide thousands of channels thanks to electrodes arranged on arrays of flexible threads, implanted thanks to a specific robotic process. The huge number of channels has no rivals but still, it is a wired solution. Microbead proposed the idea of arbitrarily placing single-channel electrodes inside the brain instead of arranged in arrays, allowing for recording and stimulation with an excellent depth-to-volume ratio. An inductive link is established between an external coil and a very small coil on each of the devices, which limits its performance. Neurograin, on the other hand, involves the use of an intermediate relay coil between independent recording/stimulating devices inside it and an external hub to deliver RF power and communicate through back-scattering. TDMA approach is used to communicate with a single frequency and distinguish between devices.
All these works focus on the scalability of the number of distributed devices inside the brain, with the motivation of placing them far from each other to cover wider areas of the brain and obtain more resolute recordings and stimulations. The challenges addressed by them are the number of channels, the depth of the implants, their dimension, the power delivery, and the communication technology for telemetry, which typically relies on RF.

1.2 Research Questions

Thanks to the well-known advantages of BCC over RF, this thesis aims to understand whether it can be a replacement wireless technique for a lightweight network of individually addressable implanted devices. The main desired advantage is the low consumption, achieved by low-power transceivers, which use rather low-frequency signals. Along with power advantages, BCC presents other key features like low absorption in the tissues, and no constraints related to the wavelength of the signals, leading to implants that could be smaller and transmit over longer distances with respect to the RF counterparts. Due to the still premature state of BCC, the questions addressed by this thesis concern a preliminary description of the applicability of such a technology in the field of scattered neural implants.

1.3 Thesis Structure

This thesis proceeds as follows: chapter 2 provides an insight into BCC, with sections related to its basics and the models to simulate it, the state of the art regarding the implants, and its application in this project, with research question and limitations; chapter 3 shows in detail the features used in the FEM model built to simulate different configurations of brain implants, and the results extracted from each of them; chapter 4 concludes with final discussions and suggestions for future works. Appendix A includes a step-by-step guide to build the model, with the hope it will be useful for further research.

Chapter 2

Body-Coupled Communication (BCC)

Body-coupled communication is a rather innovative and promising technique to let wearable and implantable devices communicate with each other, or even to make the body transmit a signal to an external apparatus. The final applications of such transmission can spread widely between medical, health, entertainment, biometric authentication, etc. The intrinsic characteristics of BCC are a rather low operating frequency, with consequent low power consumption and low absorption, high security and privacy, low interference, and high efficiency.

The very first appearance of BCC in literature has to be associated with the thesis by Zimmerman in 1995 ([5]), which proposed a "Personal Area Network" (PAN) where wearable devices could be connected by exploiting electrostatic fields directly coupled with human tissues instead of with electromagnetic waves radiation. He called this kind of wireless communication "Intra-Body Communication" (IBC), but the same concept lately has been referred to as "human body communication", "body channel communication", "body-coupled communication" (which has been adopted here), and many other names. The fundamental innovation taught by Zimmerman is to work in the near-field region instead of with radio frequency, meaning low frequency (in the range up to 1 MHz) and short haul (2 m maximum). That has several benefits when employed in a PAN: no need for large antennas to transmit low-frequency signals, limited interference between different networks due to the fast decay of the fields and the small area of the receivers, easy compliance with safety regulation of unintentional radiators, high security because of difficult detection of signals outside the body, and very low power consumption derived by low frequency and low absorption.
The principle of the Zimmerman BCC approach is the one that later has been named "Capacitive BCC" and it works like this: an electrode attached to the skin

couples a tiny electrostatic field into the body, leading to a very small current conducted by the tissues, another electrode with a certain distance from the first senses the field and the current generated and receives the signal, then it is the external environment that ensures a return path through the ground. In the years to come, other electrical coupling methods have been proposed, among which the one initially called "waveguide IBC" by Hachisuka *et al* in [6], referring to the idea in [7] already in 1997, has received a lot of attention and the name of "Galvanic BCC" in [8]. In galvanic BCC, the coupling with the tissue is achieved not by one but by two electrodes so that the signal is transmitted and received differentially and there is no need for common ground between the devices. Thanks to the ions contained in the biological material, a small current is primarily induced between the transmitter electrodes, but also a secondary portion of it flows through the surrounding tissue. The electric field and subsequent electric potential between two different points are then sensed with the receiving couple of electrodes. Another interesting mechanism is the magnetic coupling for BCC, based on a magnetostatic field instead of the electrostatic one, and requires coils instead of electrodes to couple the signal to the body. As in capacitive BCC, the loop in the transmission is closed through the external environment. Magnetic BCC has been proposed only recently in 2012 by Ogasawara *et al* in [9], and even though its results are promising, it is still in an early stage, with few data and tests related to interferences available. Because of that, only a focus on capacitive and galvanic BCC is extended in this work.

Apart from the coupling techniques, another important distinction that must be done is between the on-body and in-body communication. The former is related to wearable devices placed on the surface of the body which then make the signal propagate mainly through the skin and the tissues just below, it is the most common in the literature and available devices since it is the first to be proposed. The latter is instead the one of the implants, that usually are placed into an inner human tissue, like muscle, or even into an organ, like the stomach or heart. This has become common only in the last few years and is mostly achieved through galvanic coupling, but recently some capacitive solutions have been proposed too. There is also a combination of these two strategies, which means an in-body to on-body communication and vice versa, useful when an implant has to be linked to some other devices in the external world. In that case, for example, it is very efficient to let any signal that goes through the body exploit the BCC, and only when the signal comes at the receiver on the skin, to use wired or RF solutions to move the data into a computer to elaborate them. It is clear that talking about the constraints in terms of size, power delivery, longevity, etc there is a huge difference between an implanted BCC device and one on the skin that is easily accessible. Indeed, an implant has to be as least invasive as possible, typically, so it has to be as small as possible both for the implantation procedure and not to compromise the functioning of the specific tissue or organ where it is placed into; it has to be as long-lived as possible not to be replaced many times damaging the patient and making him suffer; it has to consume very low power since either its battery must be very small or the powering from the outside (like via ultrasound) is a delicate technique.

In this chapter, the basics of BCC technology will be explained, with a theoretical introduction and a survey on the existing models to simulate it, then the examples in the literature will be investigated and presented together with their figures of merit and challenges. In the last two sections, instead, the limiting factors to be taken into account for this project and the questions that have been tried to answer are included.

2.1 Theory And Models

BCC is a wireless technology that uses human tissues' electric characteristics to transmit low-power signals inside the body or on its surface. Typically it works in a spectrum between 0.1 MHz to 100 MHz because, at these low frequencies, the propagation loss through human tissues is smaller than through air, leading to low absorption and low power consumption. Another important intrinsic characteristic BCC is supposed to have is that, with specific considerations, it does not involve radiation of the fields outside the body, with an important consequence on the security of the information transmitted. This is the way Zimmerman intended the PAN in the first place, but then many attempts have been done trying to obtain higher performances and not always have included non-radiation as a constraint for the project. The fact that up to now there is not a specific regulation about BCC, only made things more confusing and not uniform throughout the literature. As an example, HBC ("Human Body Communication") has been included in the IEEE 802.15.6 standard, which assigns to BCC the band from 10 to 50 MHz only, but several examples can be found using a frequency out of this range. Moreover, recent descriptions of BCC include the possibility to use electrodes just in the vicinity of the body, instead of strictly in contact. Here in this thesis, it has been preferred to follow the original idea of BCC: the devices must exploit couplers and not antennas, and so transmit signals through the body and not radiate from it to keep the data safe from malicious attacks and respect the safety and low power consumption requirements. This is achieved by limiting BCC to work in the reactive near-field region, the portion of the space in real proximity to the source where reactive electric and magnetic fields are predominant.
Thinking of the transmitting BCC device as an infinitesimal electric dipole (since in our geometries its length will always be much shorter than the wavelength of the transmitted signal), and looking at the electric field distribution in any point

of the space (from [10]):

$$E_r = \frac{A}{2\pi r^2}\left[1 + \frac{1}{jkr}\right]e^{-jkr} \tag{2.1}$$

$$E_\theta = j\frac{kB}{4\pi r}\left[1 + \frac{1}{jkr} - \frac{1}{(kr)^2}\right]e^{-jkr} \tag{2.2}$$

where A and B are two parameters including quantities not relevant now, r is the radial distance from the source, and k is the wavenumber, it is possible to notice that depending on the value of r some terms are negligible with respect to others. Focusing on the value for which $kr = 1$ (so $r = 1/k = \lambda/2\pi$, where λ is the wavelength) it is possible to define three regions:

- at a distance $r \ll \lambda/2\pi$ the last terms within the brackets of 2.1 and 2.2 dominate on the others, and the energy computed is basically imaginary, so stored; this is called *reactive near-field* region.
- at a distance $r \gg \lambda/2\pi$ the first terms within the brackets of 2.1 and 2.2 dominate on the others, and the energy computed is basically real, so radiated; this is called *far-field* region.
- at the distances $r < \lambda/2\pi$ and $r > \lambda/2\pi$ the distinctions are not that strict and the *radiative near-field* and *intermediate-field* regions are defined respectively.

So, extending the analysis on the reactive near-field region 2.1 and 2.2 can be reduced in a simpler form:

$$E_r \simeq -j\frac{A}{2\pi kr^3}e^{-jkr} \tag{2.3}$$

$$E_\theta \simeq -j\frac{B}{4\pi kr^3}e^{-jkr} \tag{2.4}$$

The conclusions regarding the magnetic field are very similar to the ones exposed here. From these, it is possible to deduce that, in such a region, the energy, being imaginary and so reactive, is only exchanged between the source and the fields and not radiated, and the fields' intensity decays cubically with r meaning that the fields' distributions are highly dependent on the distance from the source. The dipole in the near-field region acts like a coupler, no longer like an antenna, and the signal's wavelength no longer constrains its length. What happens in the far-field is the opposite: the energy is radiated in the radial direction, the fields' distributions are less dependent on r and they can be approximated as spherical wavefronts.
In this context, it is useful to understand that the extension of the near-field region

in a medium depends on the frequency of the signal, which is directly related to λ, and it is possible to satisfy $r \ll \lambda/2\pi$ at moderate distances from the dipole keeping the frequency sufficiently low. This leads also to the fact that the contribution at the receiver is mainly given by quasi-static fields, whose change is not rapid enough to take into account a temporal delay between charges in the source and the electromagnetic field, so they can be considered static. It is possible to conclude that, respecting some compromise between transmitted frequency and distance of communication, BCC can be treated as an electrostatic coupling in the near-field region. The quantitative analysis of the relationship between frequency and the validity of this examination will be provided in 2.3.1.

As anticipated, the two main techniques BCC has been implemented are capacitive and galvanic coupling. Starting with the older, capacitive coupling uses a voltage potential applied to an electrode in direct contact with the body to create an electric field inside the tissue, thanks to its dielectric behavior. To have a reference, and to provide a return path to the signal, another electrode is needed, but it remains floated so that the environment is exploited for the purpose. It is the capacitive coupling of the body that naturally occurs with the Earth ground to close the loop and make the communication possible. The scope of the receiver is to detect the electric field induced in the body, which is highly dispersed in the surrounding space and highly dependent on the environment, and to do so another couple of electrodes are used, one touching the body and one floated as reference. From this description, implantation of such a device looks not possible because one electrode should be floating in the air, but recently some configurations proposed to insulate the reference electrode avoiding the short with the signal electrode through the body and they proved that the field distribution is compliant with one of the wearable devices.

Because the field spreads all over the body, the gain of the transmission is not sensitive to the channel length, or the distance between the electrodes either. Bigger electrode areas, instead, mean lower attenuation. Theoretically, the maximum frequency of the signal should be the one that avoids the antenna effect of the human body, around 150 MHz, since at that value a $\lambda/2$ dipole is around 1 m. In practice, it has been found that the gain peak happens around 50 MHz and many works exploit that, but also a lot of examples declare to create BCC at a frequency of hundreds of MHz, which would inevitably lead to radiation outside the body. In those cases, a capacitive coupling with the body is established, but speaking of BCC is not appropriate. The main source of attenuation and variability is given by the external environment, which has always, and in any case the essential role of permitting the return path. Problems of interference and security can arise for the same reason, exposing the signal to unwanted manipulation from the external world.

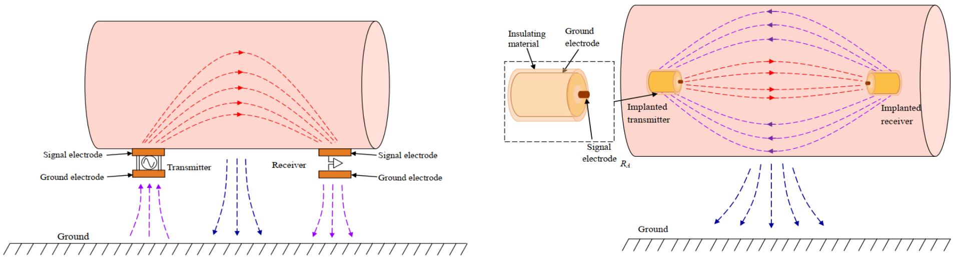

(a) **(b)**

Figure 2.1: Schematic of capacitive coupling BCC in wearable (left) or implantable (right) condition [11]

The galvanic BCC works differently, controlling the signal with a current that changes the phase from the electric current made by electrons in the device to the ionic current given by the ions in the biological medium. This mechanism is actuated with a pair of electrodes both in contact with the body and thanks to a differential voltage applied between them, making a current flow from the positive to the negative electrode through the tissue. Such a current is then divided into a primary flow, which goes directly from one electrode to the other of the transmitter without contributing to the communication itself, and a secondary flow, which arrives at the electrodes of the receiver and induces between them a voltage difference. This way, a differential signal is transmitted and received, and no ground is required either as a reference or to close the loop, as in the capacitive coupling, and so the environment is not involved at all. This way, the signal propagates completely inside the body and the location of the communication can be on-body or in-body, without any modification in the design of the electrodes, making galvanic coupling more suitable for implants.
The drawbacks come from the fact that it is much more sensitive to the geometry and the size of the devices with respect to capacitive BCC: the gain is highly dependent on the channel length, the attenuation is lower with bigger electrodes and larger distances between them, high current densities can arise around transmitting electrodes, limiting the operating frequency to lower values (typically near 1 MHz). The intrinsic advantages of galvanic coupling are lower power consumption, low susceptibility to interferences, and high security and privacy since only with direct contact with the body it is possible to intercept the signal.

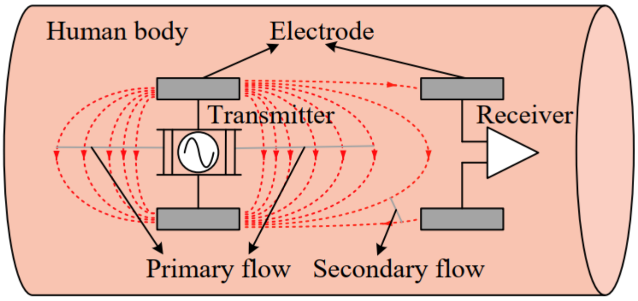

Figure 2.2: Schematic of galvanic coupling BCC [12]

To design a BCC system, it is essential to have a good model that could predict the behavior of the transmission before moving to experimental trials, especially in the case of implanted devices. Many modeling methods have been introduced over the years, and limiting to the ones useful to simulate implants, three main types are reported: analytical, circuit, and numerical models.

Analytical models mathematically derive solutions of Maxwell's equations related to the presented problem, often relying on simplifications of them or the geometry. The accuracy of these models is not very high in most cases, they are usually very complex and not easily adaptable to various situations with different parameters but provide good insight into the physical mechanisms and theory. An interesting example regarding galvanic coupling for implants can be found in [13], where authors considered the multi-layered structure of the human body and provide a model that can take into account many parameters depending on the location of the implant. No significant analytical models for capacitive implants have been found.

Circuit models are both lumped and distributed, depending on the length of the transmission considered (in quasi-static approximation discrete blocks are sufficient, otherwise a transmission-line approach must be adopted). They received many adjustments during the years, starting from a few elements and including more and more of them with increasing details. The principle is to describe a transmission channel assigning any specific part of it to an element that includes the dielectric properties of the tissues and parameters of the geometry. The elements are composed of resistances and capacitances, reflecting the losses and the ability to hold the charges of the tissues. Also, a representation of the characteristics of the electrodes and the polarization impedance is included in the most recent models. The results are frequency-dependent electrical circuits that easily provide a transfer function and the order of the attenuation received by the input signal. Their solutions are obtained quickly and they are valid for a large variety of frequencies and configurations. Regarding the implants, complete models for capacitive and galvanic coupling are proposed in [11] and [14] respectively.

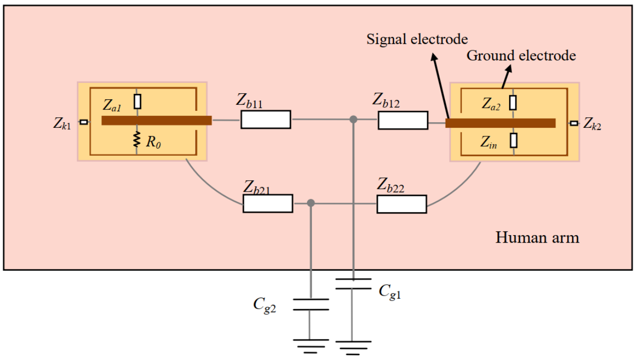

(a)

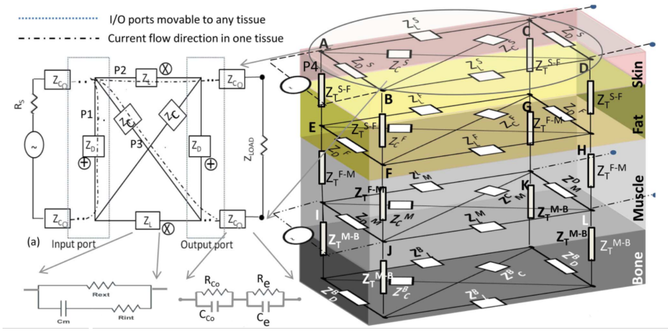

(b)

Figure 2.3: (a) Circuit model for capacitive implants [11] (b) Circuit model for galvanic implants [14]

Numerical models are the most powerful and versatile, allowing the creation of large and complex 3D representations of human parts without the need for simplifications and approximations. They are based on the division of the complete structure into simpler and smaller elements and the linearization of the problem through very big matrixes, and the most common are the ones working with finite-element modeling (FEM). The complexity of the task leads inevitably to long simulation times and a high computational cost, but the details of the underlying physics that can be obtained and analyzed have no comparison with the other methods. More complex simulations mean also that the settings and the conditions to be set are way more elaborated than the other models and the simulation programs to do that are very complex as well. Usually, in the range of frequencies common in BCC and due to the dimensions of human parts, such simulations use the quasi-static approximation to decouple electric and magnetic fields, which are then considered to be static and not time-varying, so it is always a good practice to study the validity of the models and the results, both in a theoretical way and with experimental tests. Very useful and detailed are the FEM models built in [15] and [16], because they include a variety of phenomena which well reflects real conditions and explain deeply how to set the simulations properly.

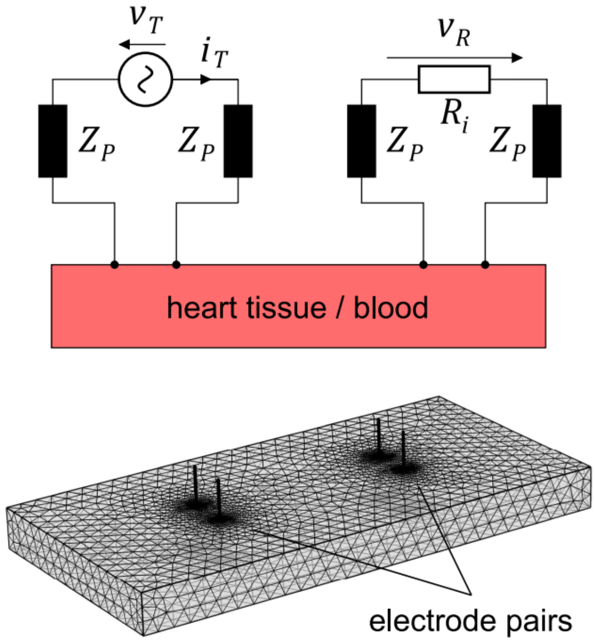

Figure 2.4: FEM model for leadless implanted pacemakers [15]

BCC vs RF

2.2 Examples

A list of remarkable papers in the field of BCC is presented here. They represent the state of the art of the technology, especially limiting to the implanted solutions.

Al-Ashmouny *et al* in [17] tested in vivo a communication between two different implants in a rat brain and an external receiver to simulate the exchange of data from a recording/stimulating system to a station to collect data. They used the brain itself as a medium and with BFSK modulation two separate digital signals with frequencies in the range $[100 - 400\,\text{kHz}]$ were simultaneously transmitted with success. The coupling with the brain tissue was achieved with one electrode only per device and a current from $2\,\mu A$ to $10\,\mu$A, so it is difficult to declare whether this is a proper BCC transmission but it has a lot of common characteristics with it, like low frequency, low power consumption, and coupling with biological tissues.

Sasagawa *et al* in [18] investigated the feasibility of extending the frequency window exploited in the previous work to transmit an image through the rat brain tissue. They succeeded in recovering the signal from an image sensor transmitting it at 50 MHz with an input power of -20 dBm between a couple of electrodes inserted in the brain surface ex vivo. The final goal of the work was to create a distributed implanted wireless system avoiding the use of antennas, very similar to this thesis, but they only tested one implant with an external receiver. However, it is interesting the selection of the transmitting frequency and the innovative application.

Lee *et al* in [19] designed and tested in vivo a 5 mm^2 neural implant on the cortex of a rat brain, which both communicates and is powered through a capacitive BCC link. The interesting aspect is that an external device with data receiver and power transmitter is positioned on the animal's back and still the prototype achieves a power delivery of 644 μW and an output frequency of 40.96 MHz, showing the common low attenuation of capacitive BCC systems.

Park *et al* in [20] proposed the first capsule endoscopy with BCC, with an in-body-to-on-body communication at 32 MHz towards one of the many receivers placed on the skin. Since it moves inside the body, some techniques were adopted to make the transmission happen between the two optimal couple of electrodes and with the best frequency. Indeed, the capsule itself has two different electrodes but only one transmits the signal while the other is for reference so it is not clear whether a galvanic or capacitive coupling is adopted. The performances obtained are satisfying with low power consumption (3.7 mW), high data rate (6 Mbps), long channel length ($10-20$ cm) and a transmitted image with high-resolution (480 x 480 byte at 3.13 fps).

Jang *et al* in [21] introduced another capsule endoscopy based on BCC transmission with better specifications. The cameras embedded increase to 4 to cover 360 °, the resolution is switched to VGA, the frequency is set to $100-180$ MHz, and a second link (at $20-60$ MHz) is established to track the position of the capsule in real-time. Even in this case, two electrodes are included in the capsule, but the signals are received on the skin with only one electrode, leaving uncertainty about the coupling mechanism but suggesting a capacitive one. However, good performance (80 Mbps thanks to the dual-band transmitter) and low power (less than 1 mW) requirements are met with success.

Reddy et al in [22] tested on humans a leadless peacemaker which is fixed to the right ventricle and ensures a 9 to 13 years lifetime with both pacing and stimulating functions. To communicate data with the external receiver on the skin uses a pulsed 250 kHz bidirectional conductive communication, basically capacitive BCC. The transmission must happen in the refractory period so that no physiological responses arise.

Khaleghi *et al* in [23] investigated the applicability of conductive BCC for dual-chamber peacemakers synchronization, with two electrodes per device. Since one of them is grounded, this is similar to a capacitive coupling with an operating frequency between 1 and 15 MHz, thanks to the fact that peacemakers need lower data rates than previous examples. In the simulations, some geometrical parameters are changed and their effect is analyzed on the voltage gain. The two implants are then tested in vivo with animal experiments, and they are attached to the heart tissue with surgery. The scope of the work is proven with low power consumption and good channel specifications.

Fahier *et al* in [24] and in [25] designed and tested bio-potential and cardiovascular monitoring systems relying on wearable capacitive BCC systems. Both use on-off-keying signals centered at 30 MHz that run through the body covering various distances and locations. Interesting aspects of the two studies are the presence of a ground electrode attached to the body to have a common reference for the physiological signals, the analysis of the compatibility with other BCC systems, and also with smart clothing.

Tomlison *et al* in [26] designed and implemented a transceiver to transmit secure biometric data via galvanic coupling between two wearable devices. Tests regard transmission distance (up to 15 cm), leakage of the signal through the air, additional adversarial receiver scenario, and how to detect it. The results are promising with an input power of -2 dBm, OOK modulation, and frequency in the range 200 to 500 kHz, obtaining a bit-error-rate of only 10^{-6}. Simulation and verification are performed with a very detailed circuit model and synthetic phantom.

Zhu *et al* in [27] used a capacitive BCC system to transmit an audio signal through the body. A continuous data rate of 1536 kbps is obtained between two battery-powered devices, showing the good feasibility of the project in a non-medical field, reaching even better sound quality than other wireless techniques.

Banou *et al* in [28] focused on a network of galvanic BCC implants, which simultaneously communicate with each other and then transfer the data to an external relay. The biggest contribution is the study of a collision-free protocol for BCC systems and near-field beamforming in human tissue, followed by experiments in a phantom. Considerations regarding safety limits are taken into account, selecting a frequency of 400 kHz and limiting the total current density when more devices are transmitting at the same time, a CDMA approach is chosen. Devices are 4 cm big and cover channel lengths up to 16 cm with good results.

Noormohammadi *et al* in [29] proved the galvanic BCC in the in-body-to-on-body scenario, designing and manufacturing an implant transmitting signals through wireless impulses. No high-frequency carrier is used and a baseband impulse technique allows obtaining a 64 kbps link with a total power consumption of 45 μW. The circuit is encapsulated in a 7 mm x 40 mm plastic capsule shell and implanted for an in vivo experiment 10 or 14 cm deep.

Bereuter *et al* in [15] simulated with precision a dual-chamber leadless pacemaker using galvanic coupling, testing parameters like channel length, inter-electrode distance, orientation between implants, and penetration into the tissue, also. They proposed to obtain data to measure the heart beating thanks to the variation of gain induced by the movement of the tissue, in a way that seems appropriate for the commercial leadless pacemakers.

Li *et al* in [16] built a model to compare the performances of implants communicating with galvanic and capacitive coupling in the same conditions. That is done by insulating the reference electrodes in the capacitive variant avoiding the short between the transmitting electrodes, a new approach to test the innovative electrode configuration from [11]. Thanks to the current flow in the tissue they proved that the return path is allowed through the air and the insulated electrodes, anyway. The known characteristics of the two techniques are highlighted in this work with more emphasis due to the same configuration and parameters: galvanic coupling is more sensitive to distance from the source, to the geometry of the electrodes, and shows lower gain, while capacitive coupling permits higher performances and longer distances with lower attenuation.

Shi *et al* in [30] showed the possibility of design a sub-dural implant for intracortical neural sensing which communicates with a cranial implant with galvanic BCC. The benefit is the lack of wires through CSF and dura mater and the limited size of the implant with respect to RF solutions in the same field. Very good performance up to 250 Mbps is achieved thanks to an impulse-based technique.

2.2.1 Figures Of Merit

Looking at the previous papers, here is a collection of FoM used to evaluate the performance of the BCC transmissions and the validity of the projects. In general, due to the large difference between the scenarios and situations of the BCC systems in the literature, it is difficult to compare FoM coming from different papers. They are highly dependent on many parameters and not many tests with similar configurations can be found. Moreover, a desired result obtained in a work may be used as a constraint for another, so it is always necessary to specify the conditions that lead to a certain result (transmission frequency, channel length, medium, etc). The most used and important is the magnitude of voltage gain G_v, defined as:

$$G_v = 20 \cdot log_{10} \left| \frac{V_t}{V_r} \right| \tag{2.5}$$

where V_t is the transmitted voltage, between the positive and the negative electrode of the transmitting device, and V_r is the received voltage, between the respective electrodes of the receiver. The logarithm is chosen to express the values in dB, and the factor of 20 comes from the fact that it is related to voltage and not power. When G_v is evaluated and plotted for a frequency range, the transfer function can be obtained and the same quantity is sometimes referred to as an S parameter common in the two-port networks. From that, the system's behavior as a filter can be analyzed and the best transmission frequency is deduced taking into account the value of the gain and where it has flat parts in function of frequency. An important FoM derived from the voltage gain when different channel lengths are considered is the pathloss. It shows how the voltage gain decreases depending on the distance between transceivers, and it is usually expressed in [dB/cm]. Common values of the voltage gain in communications between implants are: -42 dB in [16], -35 to -50 dB in [15], and -34 dB in [30]

The communication frequency of a BCC system is one of the key parameters because from it a lot of quantities are derived: the power consumption, the data rate, the bandwidth, etc. It is chosen depending on the transfer function mainly, looking at its peak value and also where it has flat parts not to have fluctuations and distortions in the received signal, but also on the specific application. Indeed, as one of the requirements for a BCC implant or wearable is to consume very low power, it is common to choose the minimum frequency value to obtain a certain performance, to reduce the consumption.

Data rate is the measure of actual data transmitted per second in communication between devices, very often it is the most important parameter since the application and the performances directly depend on it. Data rate value comes from the frequency, but also from the modulation technique, the bandwidth, and other functions of the entire system, so it is hard to evaluate it before the complete design is done. In BCC the range of achieved data rates is wide since different kinds of signals and information can be transferred. For example, in [23] 8 kbps is an acceptable data rate since BCC is used only to synchronize two peacemakers, in [25] 468 kbps are enough to transmit the ECG signal, while in [20] 6 Mbps are required to transmit the video signal from the endoscopy capsule, but they grow up to 80 Mbps when additional cameras and a position monitoring system are added

It is not common to find considerations about the received voltage amplitude, i.e. the amplitude of the signal at the electrodes of the receiver, in the literature. It is an important parameter to completely design a system since depending on it the sensitivity of the receiving device must be designed. For example, some amplification stages may be required at the receiver if its input voltage is too low, or different voltage amplitudes are received by changing simple parameters (from 5 to 40 mV_{pp} in [25], only by moving the reference electrode position).

Depending on the coupling mechanism and the system design, the input signal at the transmitter may be evaluated in terms of input current and input voltage introduced into the tissue, and, derived from that, also input power. Fixing some constraints, it is useful to compare the input quantities that produce the desired results and to try limiting them as much as possible for many reasons, like safety and power consumption. For example, in [26] a -2 bBm input power is enough to have a BER of 10^{-6} with a distance of 10 cm between the devices. Interestingly, the case studied in [28], where, exploiting the constructive or destructive interferences of the beamforming, different total input powers in the range $[2.6 - 6\,\mu W]$are obtained depending on the phase of the two transmitted signals.

When talking about BCC, an important parameter to evaluate the quality of a system is the maximum distance that allows for an acceptable gain. In fact, one of the frequent goals in the literature is to create a WBAN ("wireless body area network") that connects implantable and wearable devices all across the body. Thus, it is desired to create relatively long channels between different parts of the body and a solution can be preferred on another depending on the maximum covered distance from the source of the signal.

Other common FoM are power consumption, BER, SNR, and energy per bit.

2.2.2 Main Challenges

Since the first introduction of BCC, researchers have made progress with a focus on the models and methods for simulations, prototypes design, and final applications. Still, some open challenges need to be explored. Due to the lack of unified specifications, a large variety of different approaches and characteristics has been proposed up to now, making it difficult to compare projects and have a complete view of the state of the art regarding BCC. Therefore, there is a dire need to obtain standardization of the technology and unification of the results, to obtain clear attributes depending on the specific application. This is the reason why a lot of effort has been put into the research, but only a few works have led to everyday practical use and commercial devices. Studies towards greater miniaturization of implants, higher data rates, specific design of electrodes, and implementation together with modern technologies should be continued. Furthermore, the energy harvesting approach and the layering and networking techniques are two very underdeveloped aspects, and further advancement in the two fields is required for a breakthrough in the implementation of connected devices. Last but not least, personalized anatomical models, long-term use, and specific safety regulations are still missing in the literature

2.3 Limiting Factors

Some limitations have been taken into account during this work, both regarding the validity of the proposed study and the safety regulations implied.

2.3.1 Validity And Approximations

In 2.1 the concepts of reactive near-field and quasi-static approximation have been mentioned already. The first has been discussed in detail and relates the distance from the source with the wavelength of the signal to define the region where the electric and magnetic fields are mainly non-radiative. The second has been only introduced and is used to simplify the Maxwell equations to be used in numerical and mathematical analyses. As explained in 3.2, all the COMSOL® simulations done in this work are based on the quasi-static approximation. The reason is that, typically, in BCC the frequencies are relatively low and the sizes of the geometries are small, so the requirements of the applicability of the approximation are met. COMSOL® has a particular interface (*Electric Currents*) that allows using the approximation and in the AC/DC Module user's guide [31] they clearly explain the phenomena involved:

> A consequence of Maxwell's equations is that changes in time of currents and charges are not synchronized with changes of the electromagnetic fields. The changes of the fields are always delayed relative to the changes of the sources, reflecting the finite speed of propagation of electromagnetic waves. Under the assumption that this effect can be ignored, it is possible to obtain the electromagnetic fields by considering stationary currents at every instant. This is called the *quasistatic approximation.* The approximation is valid provided that the variations in time are small and that the studied geometries are considerably smaller than the wavelength.

Considering the fields static means that electric and magnetic fields can be decoupled, and since in human tissues no relevant magnetic interactions arise ($\mu_r = 1$ indeed), only the effects coming from the first are taken into account, with no evaluations of the second in the models.
In this section compliance with the requirements of the near-field region and the quasi-static approximation is evaluated, as both are based on a relation between a certain length in the model and the wavelength λ in the medium. To work in the reactive near-field the distance from the source, and so the channel length, in this case, must be $\ll \lambda/2\pi$, while to apply the quasi-static approximation the geometry must be significantly smaller than λ, let's say $< \lambda/10$. At the same time that is the limit to avoid the antenna effect of the geometry itself. From [32] the values of the wavelength as a function of frequency for many tissues can be downloaded, and the one in the white matter has been used because most of the simulations are done in it. In Fig. 2.5 the values of λ, $\lambda/2\pi$, and $\lambda/10$ are plotted together with the reference of the maximum dimensions used in the simulations, 5 cm and 10 cm for channel length and geometry respectively. Moreover, at the beginning of the near-field analysis in 2.1, it has been supposed that the length of the dipole, and so the inter-electrode distance, is much smaller than λ. Therefore, in the figure, the inter-electrode maximum value is plotted as well to prove that the supposition is true.

No issues come from the verification of the infinitesimal dipole, as supposed.

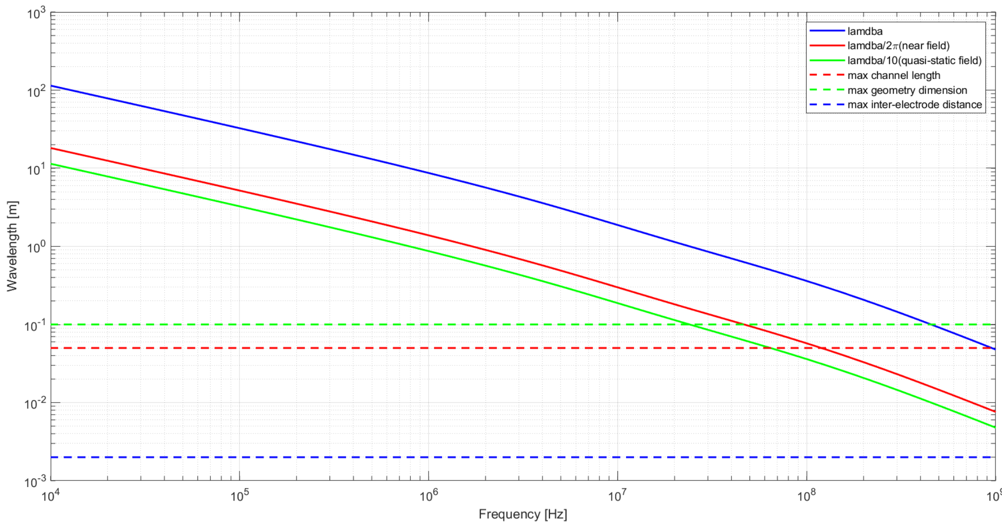

Figure 2.5: Reactive near-field and quasistatic approximation validity

The quasi-static approximation holds up to 25 MHz, but this limit can be slightly relaxed considering the factor 10 abundant. To be sure to work with non-radiative fields the frequency must be limited to 100 MHz at least, even if the margin can be lower considering that it should be $r \ll \lambda/2\pi$. As result, 10 MHz will be proposed here as the compromise to follow all the considerations above.

2.3.2 Safety Regulations

As already done in previous papers ([33] and [34]), the guidelines from ICNIRP are taken here as a reference to obtain the main limitations and requirements in terms of exposure of human tissues to electromagnetic fields. ICNIRP is the "International Commission On Non-Ionizing Radiation Protection" and focuses on studying the effects of time-varying electromagnetic fields exposure on humans, publishing instructions to protect people against any incident field with a frequency between 0 Hz and 300 GHz. The guidelines have been released many times, to update the indications in response to technological advances and more detailed measurements published year by year. Three versions of the guidelines are considered here: the very first one from 1998 [35], an intermediate one focused on the impact of low-frequency signals (100 kHz − 10 MHz) on nerve stimulation [36], and the most recent one from 2020 [37]. While [35] covers the widest range of frequency (from 0 Hz), its contents have been replaced by [37] for frequency higher than 100 kHz, so that in this specific work only the latter could be taken into account. It is also interesting to note that in 1998 current density was used as the evaluation criterion up to 10 MHz, but in 2010 they started to replace it with electric field

intensity. A different mention needs to be done for [36]: it has not been replaced by [37], but instead, it has been included in it since it treats specific cases of nerve stimulation not evaluated again in 2020. As explicitly written, [37] "valuated and set restrictions for adverse health effects other than direct effects on nerve stimulation from 100 kHz to 10 MHz, and for all adverse health effects from 10 MHz to 300 GHz."
In such guidelines mainly two kinds of limitations are defined: basic restrictions and reference levels. The first ones are based on physical quantities closely related to the adverse effects on the body itself, like induced electric field (E_{ind}) or Specific Absorption Rate (SAR), which are typically very difficult to measure precisely; the latter ones are derived from the previous and are based on quantities that are easy to evaluate and detect instead, like incident electric field (E_{inc}), so that it is possible to check the compliance with the restrictions in a practical way from the external of the body. It must be noted that, in general, the reference levels are more conservative than the relative basic restrictions, because they consider the worst-case scenario (assuming whole-body exposure to a uniform field distribution). Nevertheless, reference levels should provide an equivalent degree of protection to the basic restrictions, and thus an exposure is acceptable if it is below either the basic restrictions or the reference levels. Since through the FEM model it is possible to extract the values of any computed quantity in any point of the tissues, compliance with the basic restrictions can be checked, but also the reference levels related to the contact current are used.
Regarding all the different quantities used in the guidelines, here the electric intensity, the SAR, and the contact current are evaluated since only for frequency higher than 10 GHz other kinds of considerations must be done (typically related to power density). The field intensity is the strength of an electric field at any point and E_{ind}, taken into account in this thesis, is the intensity of the field inside a specific tissue caused by the exposition of the body to an external source. It is also computed automatically in the simulations by COMSOL® so it is straightforward to evaluate and extract from the FEM model. The basic restrictions about electric field intensity are related to any region of the body and must be averaged as root mean square (RMS) values over 2 mm x 2 mm x 2 mm contiguous tissue. The SAR, instead, shows the degree of absorption or consumption of electromagnetic energy per unit mass in biological tissue, it is expressed in [W/kg] and it is not computed by COMSOL® directly. Anyway, it is possible to evaluate it through the following equation:

$$SAR = \frac{\sigma|E|^2}{\rho} \tag{2.6}$$

where E is the E-field intensity, σ is the conductivity of the tissue, and ρ its density. ICNIRP also defines the local SAR in different regions of the body as average

(RMS) SAR in 10 g tissue, usually with higher values than the whole-body one. Values of SAR are provided only as basic restrictions.
The proper way to evaluate the spatial RMS value of the two quantities is provided by [37] itself, in the appendix. The equations for the electric field intensity and the SAR are:

$$E_{spatial\_average} = \sqrt{\frac{1}{V}\int_V |E|^2\,dv} \tag{2.7}$$

$$SAR_{10g} = \frac{\int_{V_{10g}} \sigma\,|E|^2\,dv}{\int_{V_{10g}} \rho dv} \tag{2.8}$$

where V is the volume of the box defined above and V_{10g} is the box containing 10 g of tissue.
The only mention of currents in [36] and [37] is related to the contact current I_c, i.e. the current flowing from a conductive object touched by a person, expressed in mA. It is not intended as the current flowing through the body itself but in this work it has been taken as a reference to check whether the current induced by the implant could produce some harmful effect. Indeed, contact current is inserted between the reference levels.

Moving to the actual values provided in the guidelines, some tables are reported here to summarize all the limitations with respect to the frequency. Fig. 2.6 summarizes the basic restrictions in a single picture. Fig. 2.7 shows the reference levels about contact current.

Frequency range	**Whole-body average SAR [W/kg]**	**Local head/torso SAR [W/kg]**
100 kHz to 1 GHz	0.08	2

Table 2.1: SAR basic restrictions for electromagnetic field exposure from 1 kHz to 1 GHz

Frequency range	**Induced electric field; E_{ind} [V/m]**
1 kHz to 3 kHz	0.4
3 kHz to 10 MHz	$1.35 \times 10^{-4} f$
1 kHz to 2.5 kHz	0.5

Table 2.2: Electric field intensity basic restrictions for electromagnetic field exposure from 1 kHz to 1 GHz

Frequency range	**Contact current I_c [mA]**
2.5 kHz to 100 kHz	$0.2f$
100 kHz to 10 MHz	20

Table 2.3: Contact current reference levels for electromagnetic field exposure from 1 kHz to 1 GHz

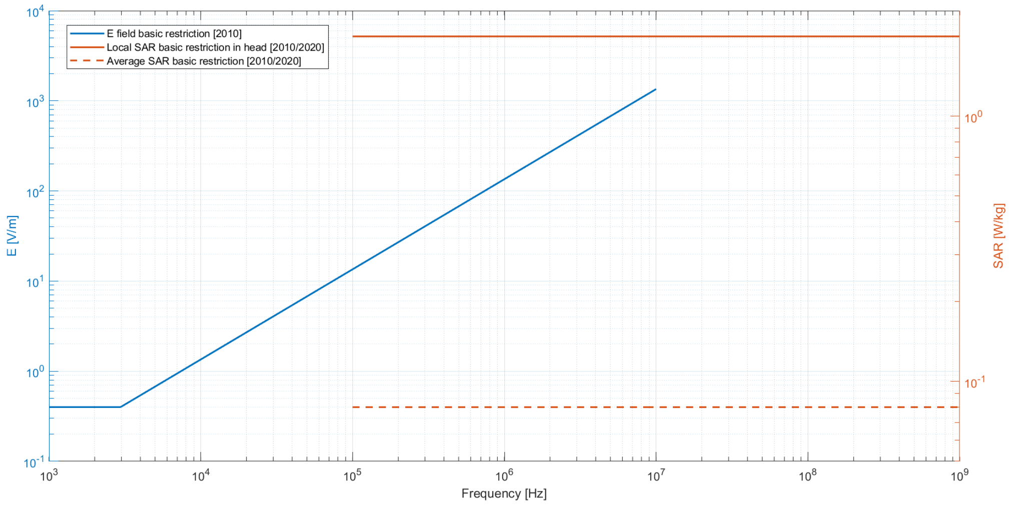

Figure 2.6: Basic restrictions

2.4 Questions To Answer

The direction this thesis is intended to investigate is the limits of BCC technology in a field not explored in detail up to now: the aim is to understand the characteristics of a communication inside the brain tissues, how small the brain implants can be, how far they can be placed each other, how the quality of the transmission is influenced by their orientation, how many of them it is possible to implant, and which harmful effects they can produce. However, it is out of the scope of this work to study the power delivery of the implants, their networking or channel access, their link to an external computer, the circuit design of any device, and also the final application, whether it is for recording or stimulation.

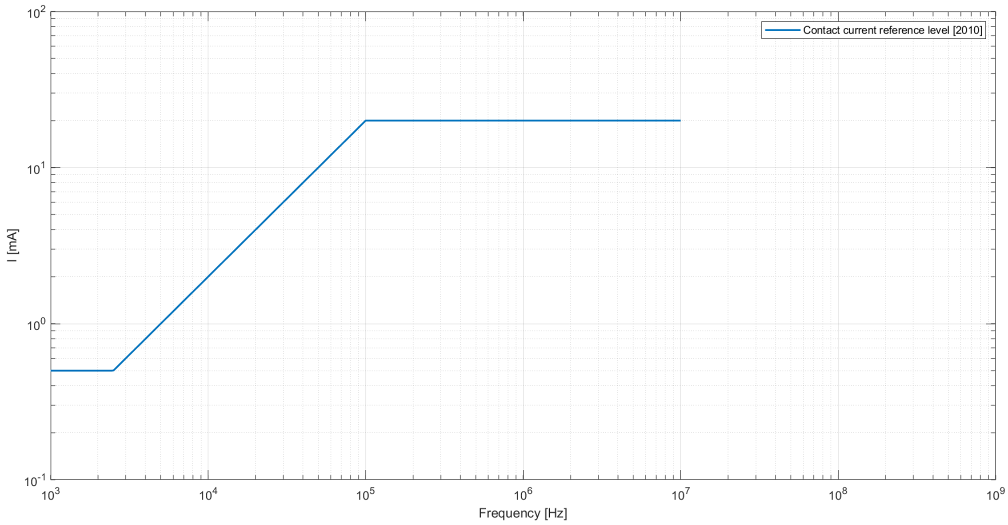

Figure 2.7: Reference levels

Chapter 3

Galvanic BCC For Microscale Implants In The Brain

The main contribution of this thesis is the study of the applicability of the BCC for a network of millimeter-scale implants in the human brain. To this end, the first step is to create an accurate model to simulate the scenario before carrying out rather costly and time-consuming experimental validation. As explained in section 2.1, there are different types of models for simulating specific transmission scenarios using BCC. After some attempts, this work has focused on finite-element modeling with COMSOL Multiphysics® among others. Although this choice comes with the cost of complex and long simulations, it has been taken because it has allowed obtaining a very detailed model, able to easily play with the geometrical parameters, and also to look at the effects the implants would cause in any point of the head. To properly approximate a human head, a sphere has been modeled in 3D with some layers representing the tissues inside it. For each layer, the relative permittivity and the conductivity have been evaluated and assigned manually. Then any implant has been simulated with a couple of cylindrical electrodes, placed inside the sphere in specific positions with different sizes, and coupled with an equivalent circuit to link the two electrodes in a single device with a certain internal resistance. Once the model has been completed (Fig. 3.1), various geometrical and electrical parameters are swept and their effect on the BCC metrics is studied. In more detail, the variations of the size and the location of the implants, the distance between different implants, different kinds of misalignments in the implantation, the internal and load resistances of the devices, and the electrodes' materials have been exhaustively studied, and the results are presented in the last section of this chapter.

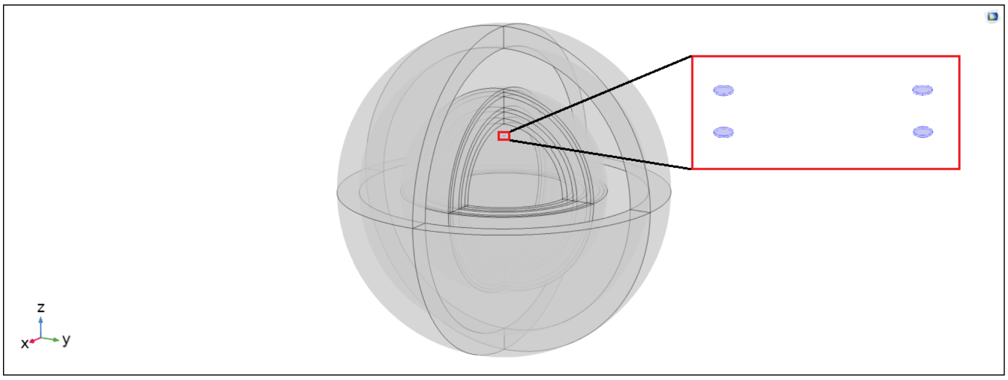

Figure 3.1: FEM model with focus on the electrodes

3.1 Dielectric Characteristics Of Human Tissues

Electromagnetic fields interact with human tissues, and relative permittivity (ϵ_r) and conductivity (σ) allow us to understand how such fields propagate through them and which effect they produce. For biological tissues, obtaining the frequency-dependent values of ϵ_r and σ has been a problem at the base of physics and biology for decades. There is an extensive number of examples in the literature to obtain data and build precise mathematical models for physical analyses. In 1996 Gabriel *et al*, published a parametric model based on the Cole-Cole equation, by adding experimental data to the literature. The Cole-Cole equation is a model used to describe the dielectric relaxation of materials, the delay in molecular polarization under the effect of a changing electric field. It expresses the complex dielectric constant ϵ^* as:

$$\epsilon^*(\omega) = \epsilon_\infty + \frac{\Delta\epsilon}{1 + (j\omega\tau)^{(1-\alpha)}} \tag{3.1}$$

where ϵ_∞ is the permittivity at infinite frequency, $\Delta\epsilon$ is the magnitude of the dispersion, τ is a time constant related to the polarization mechanism, and α is the dispersion broadening parameter that makes Cole-Cole equation differ from the Debye equation (where $\alpha = 0$). This is a reference when talking about dielectric dispersion, which means the dependence of materials' permittivity on the frequency, and many variants of it have been published. Cole-Cole equation, for example, is used when the dielectric loss peak shows symmetric broadening.
In [38], a more accurate parametric model has been obtained by taking into account the different relaxations at different frequency regions, as well as static ionic conductivity:

$$\epsilon^*(\omega) = \epsilon_\infty + \sum_n \frac{\Delta\epsilon_n}{1 + (j\omega\tau_n)^{(1-\alpha_n)}} + \frac{\sigma_i}{j\omega\epsilon_0} \tag{3.2}$$

where the summation of n terms is used to consider the contribution of any dispersion region, σ_i is the static ionic conductivity, and ϵ_0 is the permittivity of free space.
In order to extract the values of (ϵ_r) and (σ) from ϵ^* below two equations should be applied:

$$\epsilon_r = real(\epsilon^*) \tag{3.3}$$
$$\sigma = -\omega\epsilon_0 imag(\epsilon^*) \tag{3.4}$$

However, the biggest contribution of [38] is the evaluation and the collection of all the above parameters for a large variety of human tissues. They are reported in a table including four dispersion regions (i.e. n of 1 to 4 in equation 3.2) and allow anyone to evaluate the complex permittivity of 17 different tissues on a large frequency range. In this work, a frequency range of [1 kHz − 1 GHz] has been taken into account, and with a simple MATLAB script, the dielectric characteristics of skin, fat, muscle, and bone tissues have been evaluated with (3.2) and used to replicate the model in [16]. Then, because of the need for data referring to other tissues not included in [38] (i.e. cerebrospinal fluid and dura mater), the online database of the IT'IS Foundation has been explored. From [39] the values of ϵ_r and σ for skin, fat, muscle, bone, dura, cerebrospinal fluid (CSF from now on), grey matter, and white matter over the frequency range of [1 kHz − 1 GHz] have been downloaded. They are very similar to the ones calculated autonomously in MATLAB before but show some corrections due to recent updates in the literature and newer measurements. Just as a reference, Fig. 3.2 and Fig. 3.3 show the behavior of ϵ_r and σ with respect to the frequency, respectively.

3.2 FEM Model

Due to the quasi-stationarity of the fields treated in this analysis, inductive effects and wave propagation can be neglected inside the human body (as stated in [40]), so the electric and the magnetic fields can be decoupled in the FEM model. This leads to a simplification in the Maxwell equations and in the COMSOL®model itself: no magnetic fields are evaluated (in fact it will be $H = 0$ and $B = 0$) and no magnetic permeability μ has to be considered between the input parameters. Using COMSOL Multiphysics® 6.0, in the *AC/DC module* it has been enough to select only the *Electric Currents* and the *Electrical Circuit* interfaces, to exploit the quasi-static approximation, and to couple the 3D geometry with transmitter

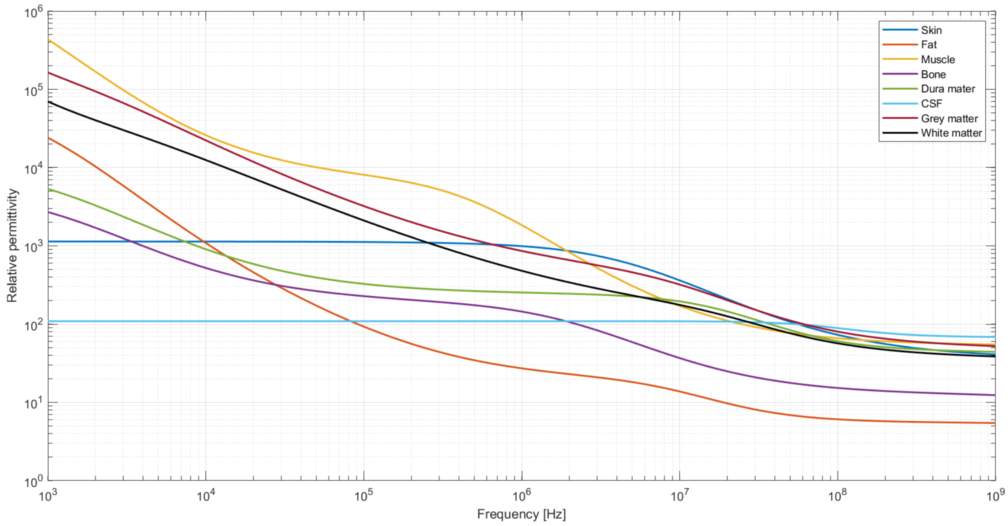

Figure 3.2: Relative permittivity of all the tissues used for this work

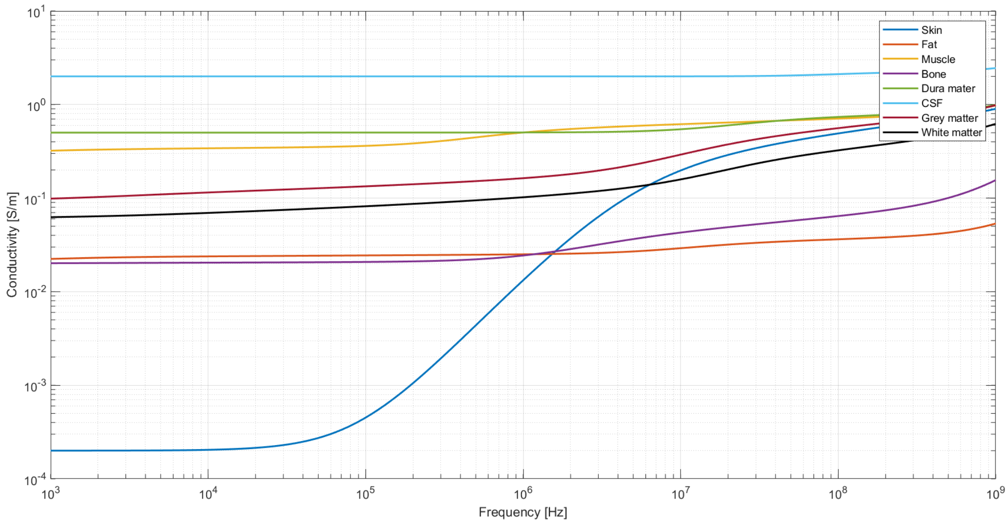

Figure 3.3: Conductivity of all the tissues used for this work

equivalent circuits respectively. Then the layered sphere approximating the human head and the cylindrical electrodes have been built, together with the definition of any parameter and setting related to the geometry, the materials, the polarization impedance, and the circuit. In the end, a *Frequency Domain* study has been set to compute the response to a harmonic excitation for a frequency range of $[10\,\mathrm{kHz} - 1\,\mathrm{GHz}]$ to obtain data on a wide spectrum.

3.2.1 Equation

Looking at the COMSOL®documentation, it is possible to understand which specific physical equations are used in the simulations to solve the FEM model that has been set. Starting from the Gauss' Law and the charge continuity equation, which are:

$$\nabla \cdot D = \rho \tag{3.5}$$

$$\nabla \cdot J = \nabla \cdot (\sigma E + J_{source}) = -\frac{d\rho}{dt} \tag{3.6}$$

and remembering that:

$$D = \epsilon E \tag{3.7}$$

$$E = -\nabla V \tag{3.8}$$

where D is the electric displacement, ρ is the electric charge density, J is the current density, σ is the electric conductivity, E is the electric field intensity, J_{source} is the current density coming from the external source (in this work it is equivalent to the current out of the electrodes), and ϵ is the permittivity; considering the fact that in the absence of inductive phenomena, the Maxwell equations in the frequency domain used in the model can be simplified to:

$$\nabla \cdot (j\omega\epsilon\nabla V) + \nabla \cdot (\sigma\nabla V) + \nabla \cdot J_{source} = 0 \tag{3.9}$$

where V is the scalar electric potential and ω is the angular frequency.

3.2.2 Geometry and Materials

In order to get confident with COMSOL®models related to BCC, the first step in this thesis has been to replicate the model built in [16]. That has helped a lot to understand how to assign to each material different sets of dielectric properties, but also which kind of geometrical variations apply to study their influence on the final results. The default electrodes' configuration in [16] has been taken also as a reference and a starting point for the specific application in the brain. In fact, Li *et al.* simulated a transmission between two implanted devices in a human arm, considering mainly two pairs of cylindrical copper electrodes with a radius of 5 mm, a height of 1 mm, a distance between electrodes of 5 cm and a distance between devices of 10 cm. The arm itself was modeled as a cylinder with four layers (from the outside assigned to skin, fat, muscle, and bone), and the implants were placed inside the layer representing the muscle tissue. It turned out to be very important to include in the simulation a cylinder of air surrounding the arm, to mimic the external environment. Even more, inside such a cylinder another thinner layer was included and assigned to be an *Infinite Element Domain* to reproduce the unbounded air. In Fig. 3.4 the replica built as an example for this work is shown, and it is possible to notice all the different layers just described.

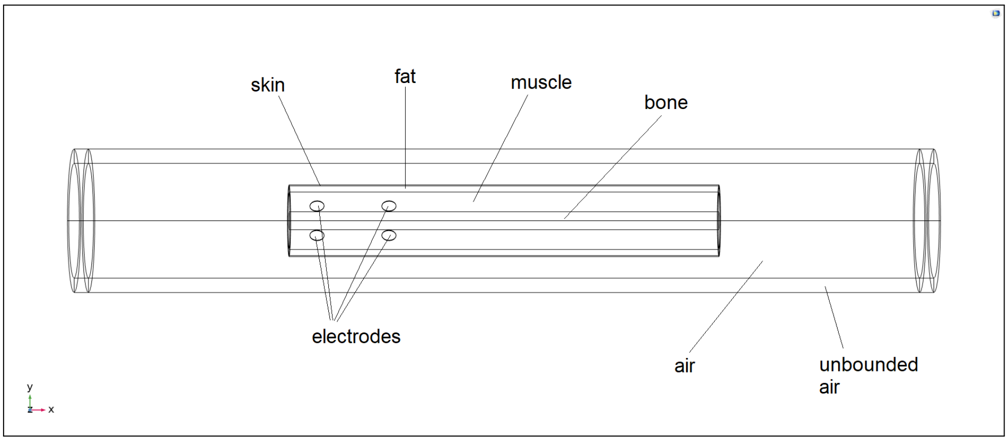

Figure 3.4: FEM model of human arm from [16]

Moving to the application of implants in the human brain, the model built by Shi *et al* in [30] has given additional useful examples and ideas to this project. They approximated the human head as a sphere with seven different layers, and the same geometry has been built here, even if they mainly focused on a trans-dural link (an up-link communication from the surface of the cortex toward the inner side of the skull) while here a communication limited to implants in the brain tissues is studied. Looking at the definite model used here, it is composed of a sphere with a radius of 93 mm and seven concentric layers with thickness expressed in the table below.

Tissue layer	**Thickness [mm]**
Skin	3
Fat	4
Skull	10
Dura	1-4
CSF	3-5
Grey Matter	5
White Matter	62-67

Table 3.1: Thicknesses of the considered tissues in the head

Note that dura and CSF together can largely vary between 4 and 9 mm depending on the location of the cortex, but also on the gender or the age of the subject; for simplicity, the maximum thickness of both has been considered for the FEM model, leaving only 62 mm to the radius of the most inner tissue, which is the white matter. Then an external sphere of air has been created with a radius of 150 mm, from which a 20 mm layer has been dedicated to the *Infinite Element Domain*. That helps to emulate the unbounded air that would surround a patient, without the need to explicitly define a huge domain of air that would increase a lot the simulation time and size. Fig. 3.5 displays the geometry described, where the air domains have been temporarily hidden to better focus on the layers defined.

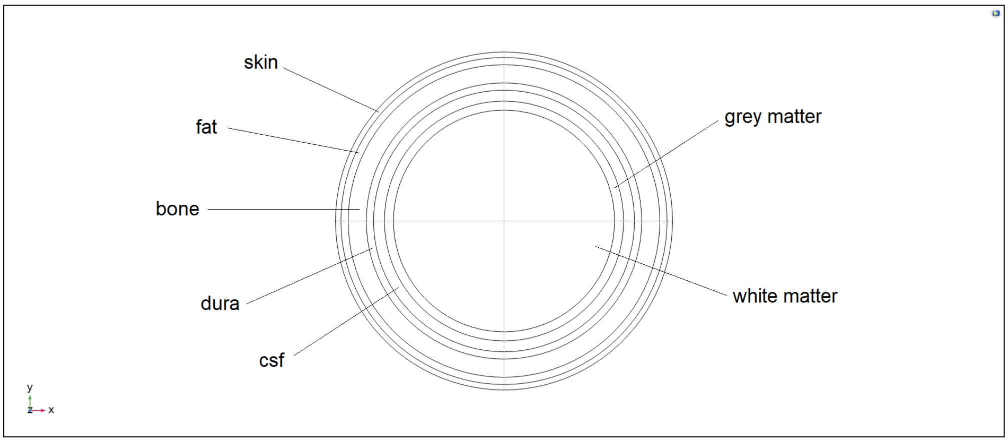

Figure 3.5: FEM model of human head

Regarding the electrodes, they have been initially designed equal to the ones in the arm example, so copper cylinders with 5 mm radius and 1 mm height. Electrodes with such dimensions are not employable for implantation in cerebral tissues, but that has been useful to make an examination of the effects of a different location inside the body keeping all the other variables unchanged. Then, the size and distance of the implants have been scaled, as exposed in the results section.

In order to complete the definition of the 3D model, the only thing remaining is the assignment to each domain of the respective material properties required by the physics selected for the simulation. In this case, and as already explained from the physical point of view, the only quantities needed to solve a frequency domain study with the *Electric Currents* interface in COMSOL®are the relative permittivity and the electrical conductivity. Thus, instead of getting existing materials from the library, blank materials have been added to the model. Their frequency-dependent ϵ_r and σ values previously downloaded have been imported into the model thanks to the *Interpolation function* while regarding Copper and Air, constant values have been given, respectively $\epsilon_r = 1$, $\sigma = 5.998 \times 10^7$ S/m and $\epsilon_r = 1$, $\sigma = 0$ S/m.

3.2.3 Circuit

Figure 3.6: Equivalent circuit of transmitter (left) and receiver (right)

An easy way to analyze the effects of BCC on the brain tissues is to simply apply a fixed voltage to the surfaces of the transmitting electrodes and monitor the voltage on the surfaces of the receiving electrodes. In this case, in a differential electrode pair like the one in galvanic BCC, for a signal amplitude of V_T, the positive and negative electrodes should get fixed to $V_T/2$ and $-V_T/2$, respectively. Then the electric potential of receiving electrodes should be monitored. The receiving voltage can be driven from $V_R = V_{Rp} - V_{Rn}$, where V_{Rp} and V_{Rn} are the voltages at the positive and negative receiving electrodes respectively. However, this method employed in some state-of-the-art papers ([41] for example), does not include the influence of the internal resistance of the transmitter and the receiver themselves, leaving the positive and negative electrodes uncoupled. Furthermore, the possible common ground effect between different devices cannot be implemented in this way.
In COMSOL, there is a *AC/DC Module* that allows for interface with *Electrical Circuit*, using a SPICE netlist description. This module includes, among others, the basic electrical component such as generators, resistors, etc. This has come to be very useful in this model, to study the effects of equivalent circuits representing the transmitting and receiving devices, instead of only focusing on the electric field and potential spreading through the tissues. In order to couple such ideal circuits with the 3D model, (i.e enable *Electric Current* and *Electrical Circuit* interfaces to communicate), the *Terminal* and *External I vs. U* function have been used. That makes it possible to connect a specific metallic object in the FEM model to a node of the netlist defined in the circuit, leading to the more sophisticated simulation of a transmitting device with a certain voltage/current AC source and related internal resistance and receiving devices with the proper load resistance. Following this approach, the configuration shown in Fig. 3.6 has been created in COMSOL, where $V_{IN} = 1\,\mathrm{V}$ between nodes 3 and 2, $R_S = 50\,\Omega$ between nodes 3 and 1, and $R_L = 50\,\Omega$ between nodes 4 and 5, and two different grounds have been placed and assigned to nodes 0 and 10. The presence of the grounds is essential in

a SPICE netlist and also required in the settings of *External I vs. U* to specify the reference node of any circuit connected to the electrodes.

3.2.4 Polarization Impedance

Whenever a metallic object, like an electrode, is put in contact with a solution a so-called “electrical double layer” is formed at the interface between the two. This phenomenon has been exhaustively studied and characterized in the electrochemistry field, so it is possible to explain it in detail.
In the first place, natural chemical reactions occur at the surface of the electrode touching the molecules inside the solution and they are reduction or oxidation processes that need an exchange of electrons to be completed. This aspect is governed by Faraday’s law, which in turn gives the name to the processes that cause the presence of a proper electric current flow at the interface, the “faradaic processes”. Since either the solution already has free ions or they emerge from the reactions just described, charged molecules will appear and concentrate at the surface obtaining a “surface charge”. Still, it is possible that under some circumstances this behavior does not happen by default unless an electric potential is applied at the electrode side. In that case, the formation of the current and the surface charge is not only helped, but even more, it is possible to control and vary them through the external voltage. The first layer is formed this way. The second layer is considered that of the charges which tend to be attracted to and repelled from the metal-solution interface, because of the variations in the structure after the reactions but also responding to the external voltage. In this case, there are no faradaic processes in place, and not even an actual exchange of charges happens at the interface, but external currents can flow (at least as transients). This takes the name of “double-layer charging”.
As explained, both the phenomena described appear in any situation where an electrode touches a solution, so they are relevant in the case of medical electrodes immersed in an electrolyte solution. In galvanic coupling, a pair of metallic electrodes is inserted into the biological tissue, creating two different electrode/electrolyte interfaces. Indeed, in a case like this, biological tissues can be treated as electrolytes supposing that the electrode is mainly in contact with the extracellular fluid, as expressed in [15]. Results from works using the physiological saline solution (0.9% NaCl) as the electrolyte can be used with a good approximation for this work (from [42]) because extracellular fluid and physiological saline solution have similar ionic content. Directly at the contact of metal and tissue the faradaic processes arise, due to the natural chemical reactions between them, favoring the creation of a first layer of surface charges coming from the redox reactions and from the free ions in the electrolyte. Then, thanks to the voltage that is applied to the electrodes, a second layer appears, composed of the ions in the solution that are attracted by the

Coulomb force provided by the electrode itself and the first layer too. Of course, this second layer is not firmly attached but is more probably composed of free ions of the electrolyte that move according to the voltage they are influenced by.

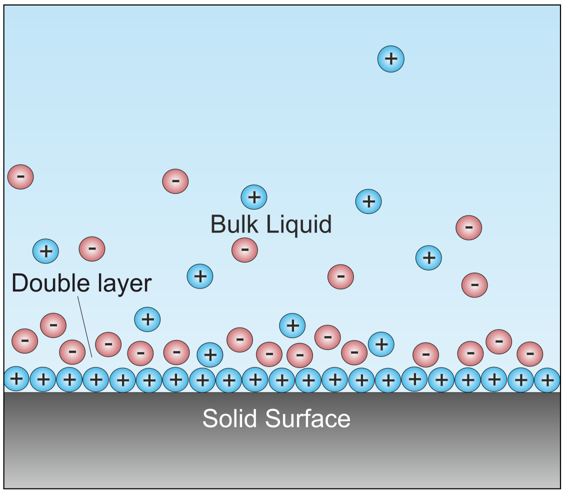

Figure 3.7: Scheme of the double layer [43]

From the electrochemical point of view, the explanation of the presence of the double layer in our application is now given. Instead, the electrical representation of it is still to be addressed. Thanks to [42] and [44], It has been possible to define an equivalent circuit to describe the electrical double layer in a way to be included in the FEM model that has been built. Throughout the literature regarding the topic, in [42] the best model of the double layer has been found since it well explains the correspondence between the physical phenomena and the electrical components and shows a good agreement with several experimental data. It simply consists of two elements in parallel: a pseudo-capacitance Z_{CPA} ("constant phase angle impedance", introduced by Richardot himself) representing the non-faradaic processes, so the ones responsible for a current flow via the redistribution of ions in the tissue and electrons in the electrode, and a proper resistance R_{CT} ("charge transfer resistance", derived from the Butler–Volmer equation), regulating the faradaic current given by electrons moving for the redox reactions at the interface. It is also required to specify the voltage across the double layer since its characteristics depend on that too, as said before. Looking at the mathematical description of the two elements, Z_{CPA} has the form

$$Z_{CPA} = K(j\omega)^{-\beta} \tag{3.10}$$

where K and β are constant, normalized for the electrode surface area and function of the electrode material. Their units are $[\Omega \mathrm{m}^2 \mathrm{s}^{-\beta}]$ and scalar respectively. Their values will be expressed below. ω is the angular frequency of the applied signal. Concerning R_{CT}, instead, it has been described as

$$R_{CT} = \frac{RT}{nFI_0} \tag{3.11}$$

where R is the gas constant ($8.3145\ \mathrm{J\,mol^{-1}\,K}$), T is the temperature in Kelvin, n is the number of electrons per molecule participating in the reaction, F is Faraday's constant ($96485\ \mathrm{A\,s\,mol^{-1}}$), I_0 is the exchange current normalized for electrode surface area, with $[\mathrm{A\,m^{-2}}]$ as unit.
The parallel combination of these two elements is defined as electrode polarization impedance (EPI) Z_P and calculated as:

$$Z_P = Z_{CPA}||R_{CT} \tag{3.12}$$

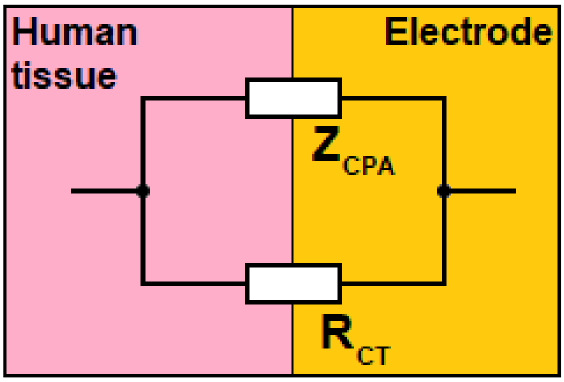

Figure 3.8: Scheme of the polarization impedance Z_P

Z_P has been incorporated in the COMSOL®model thanks to the *Distributed Impedance* function in the *Electric Currents* module. This approach consists of a surface impedance approximation without specifically defining a separate layer at the interface, which would be very thin (range of nm) and so extremely computationally costly. The only requirement is to select the surfaces (*boundaries* in COMSOL) where the double layer arises, and the parameters will be evaluated depending on their area. It is also needed to express the reference voltage, i.e. the voltage of the respective electrode.
As for the adopted values of the above parameters, examples with Platinum electrodes have been found more widely in the literature, for example in [15]. Still, thanks to [16] it has also been possible to obtain those of Copper electrodes. A table with a comparison of the different values is provided here:

Parameter	Copper	Platinum
K $[\Omega \mathrm{m}^2 \mathrm{s}^{-\beta}]$	0.08	1.57
β	0.48	0.91
n	2	2
I_0 $[\mathrm{A\,m}^{-2}]$	6.41×10^{-4}	6.41×10^{-4}

Table 3.2: Z_P parameters depending on electrode material

3.2.5 Complete model

To complete the description of the complete model, it has to be mentioned that the mesh has been managed by COMSOL®itself with the *Physics-controlled mesh* function, but an *extremely fine* quality of it has been necessary to avoid the minimum size of mesh elements to be comparable with the size of the electrodes. This has made the simulations very heavy and long in time, before moving to a simpler model as explained in the next section. Another important setting to obtain converging simulations has turned out to be the definition of ground not only in the circuits but also in the FEM model itself. That has been fixed to the outermost surface of the air sphere, so at the end of the infinite element domain, which represents the infinite space.

Following, a qualitative representation of the complete model with highlights of any function is given in Fig. 3.9

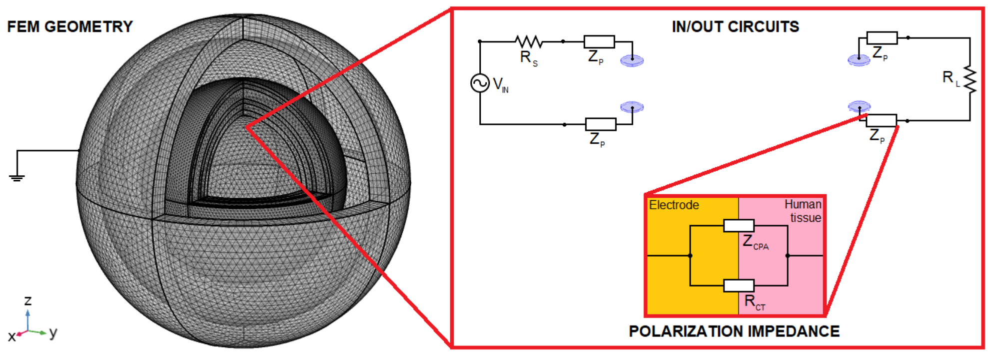

Figure 3.9: Scheme of the complete model with highlights of the key functions

3.3 Results

With the complete model including all the functions and characteristics explained in the last section, the exploration of the effects of any parameter has begun. In general, the main evaluation criterion used to analyze a specific configuration is the magnitude of voltage gain G_V defined in 2.5.

The first aspect investigated is the innovative transmission medium used in this thesis. While in [16] the devices were implanted in the muscle tissue of the arm, here the white matter of the brain has been used mainly as the possible location for implantation, and no previous examples of it have been found in the literature. So, reproducing the same geometrical configuration of the electrodes proposed by Li *et al*, the first simulation has been done in an impossible scenario for an invasive BCI: cylindrical electrodes with radius $R_e = 5\,\mathrm{mm}$, height $H_e = 1\,\mathrm{mm}$, inter-electrode distance (distance between the two electrodes of the same device) $D_e = 5\,\mathrm{cm}$ and channel length (distance between two different devices facing each other) $L_c = 10\,\mathrm{cm}$ have been built and placed inside the innermost layer of the sphere, as it is possible to see in Fig. 3.10a. This is unfeasible for any kind of implantable device in the human brain, but it has been done to look at the shape of the transfer function obtained in the medium characterized by the dielectric properties of the white matter. Observing Fig. 3.10b, at first sight, the shapes of the two transfer functions result similar, both showing a high-pass behavior in the selected frequency range, but while the gain in the muscle has higher amplitude in the rising part, the gain in the white matter has a higher peak in the flat part ($-37\,\mathrm{dB}$ with respect to $-42\,\mathrm{dB}$). Also, their cut-off frequencies are not the same: 30 kHz for the muscle tissue, 200 kHz for the white matter.

Then, trying to move toward an overall device dimension that could be suitable for a brain implant, the ratio between all the parameters R_e, H_e, D_e, and L_c has been fixed and a reduction factor k_{red} has been used to scale all of them so that a scaled system could be obtained without altering the initial configuration. The goal of the scaling has been set to a final inter-electrode distance of 1 mm, trying to simulate a device with a full size of such value which can be considered good for a brain implant. k_{red} has been changed from 1 to 0.02, leading to D_e in the range $[5\,\mathrm{cm} - 1\,\mathrm{mm}]$. The final values of the others are $R_e = 0.1\,\mathrm{mm}$, $H_e = 0.02\,\mathrm{mm}$, and $L_c = 2\,\mathrm{mm}$, and from now on the model built with these characteristics will be referred as "MODEL_1". Fig. 3.11 shows the effect of the scaling on the voltage gain over the entire frequency range. As one can expect, the peak value of the gain decreases with a scaled geometry, but some interesting phenomena show up: the first is that the decrease seems constant up to $k_{red} = 0.2$ (so up to $D_e = 50 \cdot 0.2 = 10\,\mathrm{mm}$) but then it saturates, and the second is that the cut-off frequency of the transfer function moves to higher values with the increased scaling. Focusing on the peak of the voltage gain Fig. 3.12 highlights its behavior depending on the reduction factor. From it, the decrease with constant slope is even better displayed up to $k_{red} = 0.3$, and after that, a sort of saturation appears. Looking at

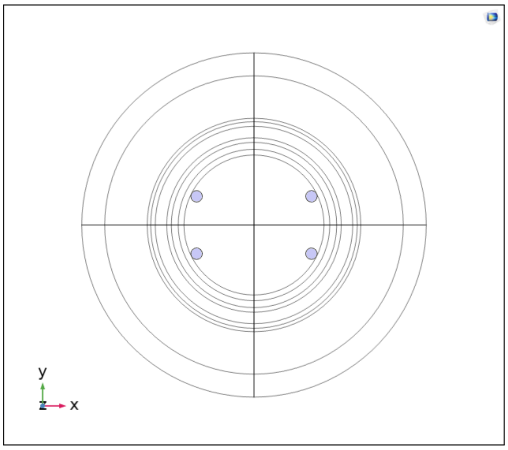

(a)

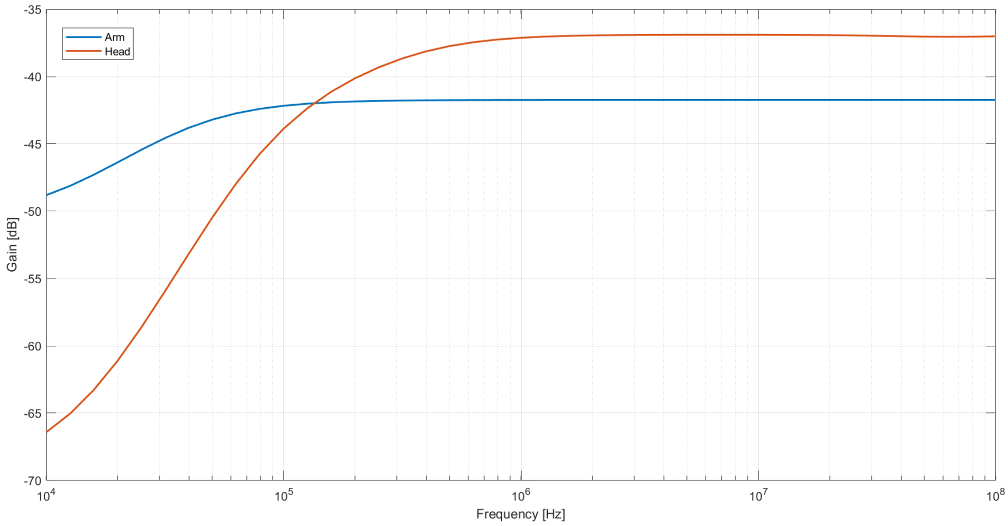

(b)

Figure 3.10: (a) Geometry of the model with electrodes' configuration equal to the one in the arm (b) Comparison of the voltage gain obtained in the arm and in the head

the amplitude values, when the dimensions go from 100% to 30% of their initial values, the gain drops constantly from −37 dB to −46 dB, but then from 30% to 2% it loses only 1 dB more. The cut-off frequency moves with a constant ratio too, ranging from 200 kHz to 10 MHz.

To have a deeper insight into the impact of the scaling, the received voltage $V_R = V_{Rp} - V_{Rn}$, where V_{Rp} and V_{Rn} are the voltages at the positive and negative receiving electrodes respectively, have been observed as well. Fig. 3.13 compares all the V_R curves for increasing scaling, showing that they all grow up to a peak

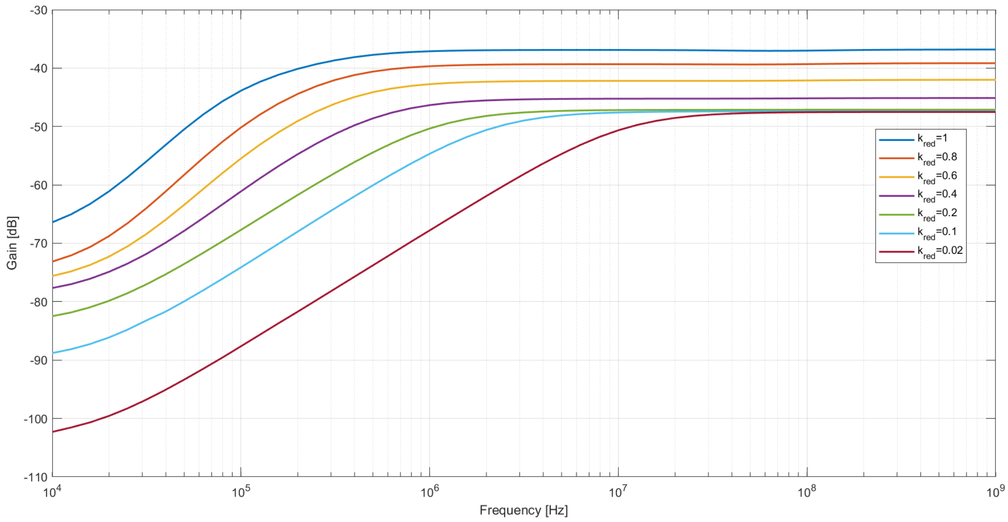

Figure 3.11: Voltage gain for reduction factor from 1 to 0.02

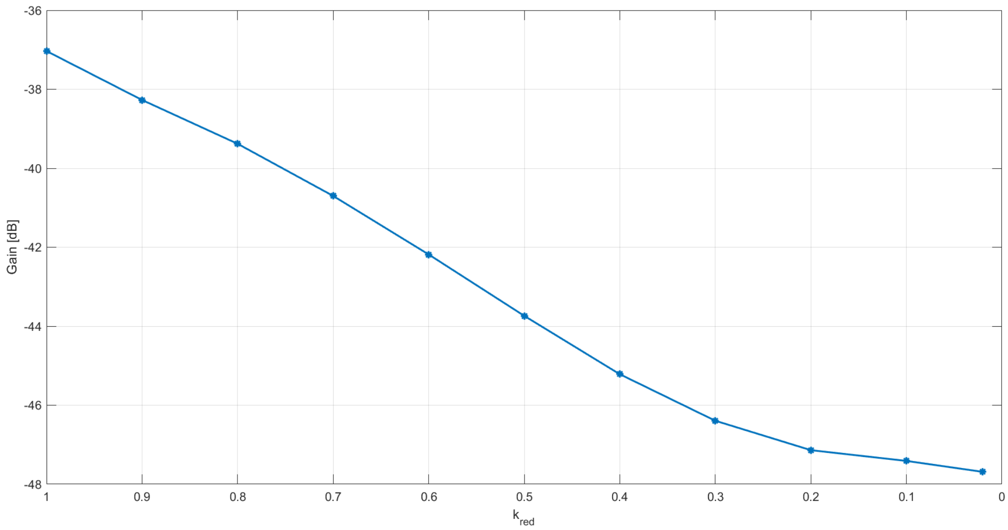

Figure 3.12: Variation of voltage gain peak for reduction factor from 1 to 0.02

and then decrease. There are two similarities with the behavior of G_V. The first is that the amplitude of the peaks decreases with smaller dimensions but it reaches saturation for $k_{red} = 0.2$, and the second is that the peaks appear exactly at the cut-off frequencies of the different G_V curves seen above. Fig. **??** highlights these aspects.
Reducing the size of the implants comes with the drawback of lower G_V and V_R peak but, on the other hand, since V_R peak shifts to higher frequency values, some benefits can be obtained in high data-rate communications. For instance, when

considering a data carrier frequency of 10 MHz, the smallest receiving sensitivity is required for $k_{red} = 0.02$ compared to larger scaling factors.

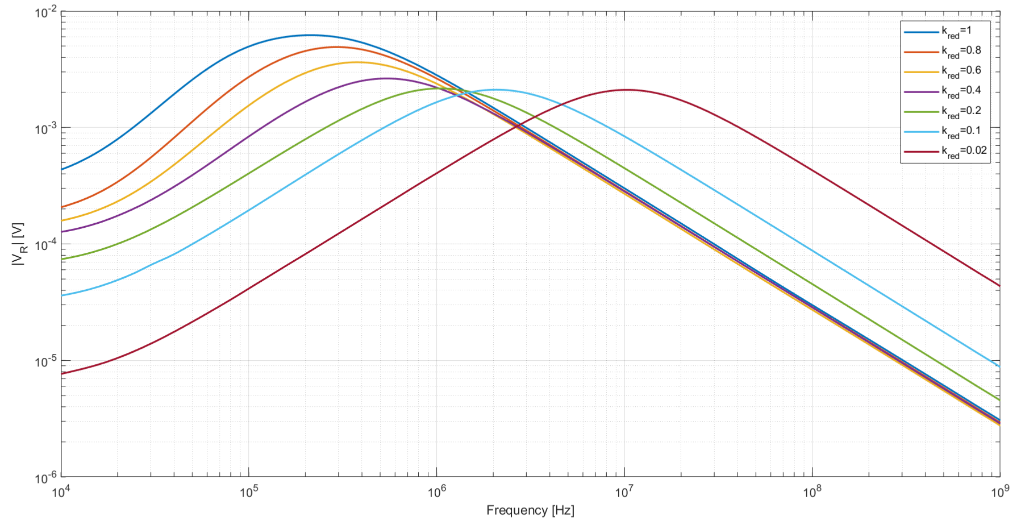

Figure 3.13: Received voltage for reduction factor from 1 to 0.02

Once the acceptable value of 1 mm for the overall dimension of the device has been reached, that has been fixed as the starting point to investigate the variation of the parameters involved in the BCC communication, looking for the limits of the galvanic coupling in an implantable wireless BCI scenario. As common in the literature, in the beginning, simulations have focused on purely geometrical variations of the electrodes in MODEL_1, like channel length, inter-electrode distance, misalignments, and location. For each of those, the simulations have been run over the entire frequency range of $[10\,\text{kHz} - 1\,\text{GHz}]$ to check whether the transfer function changes, but to save time and memory required to extract the results, a simpler model has been built. This consists of a 50 mm x 50 mm x 71 mm box with the layers from white matter to bone only (Fig. 3.15a), where the ground has been fixed on the outermost surface and with all the electrical and circuital settings unchanged. It has been found that the simple model offers the same results as the complete one, as proven in Fig. 3.15b.

Working on the simple model, the dependence of the gain on the channel length has been investigated keeping the other parameters as in MODEL_1. At first, placing the two devices at the same depth (11 mm below the interface between white and grey matter) with the pairs of electrodes parallel one to the other, L_c has been increased up to = 9 mm with 1 mm steps and the results are shown in Fig. 3.16, where some artifacts occur between 100 kHz and 1 MHz. They come from the simplification of the model and its coarser mesh and affect the transmission in a

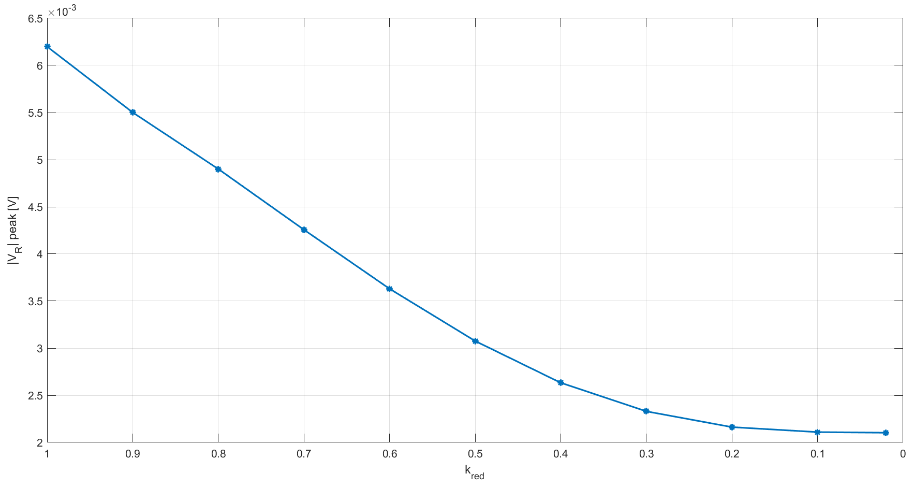

(a)

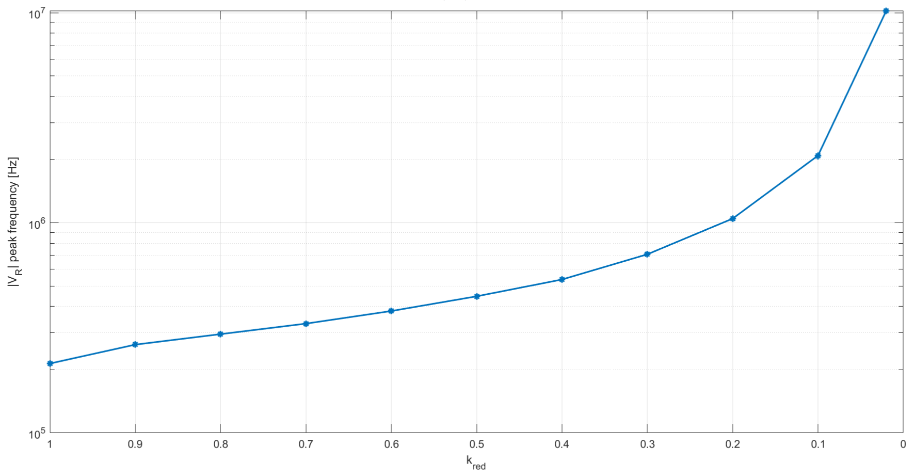

(b)

Figure 3.14: Variation of (a) received voltage peak, (b) frequency of the received voltage peak for reduction factor from 1 to 0.02

frequency range not that relevant for this study, so they can be ignored. Regarding the amplitude of the voltage gain, as expected, a larger distance means higher attenuation of the received electric field so a lower voltage gain at the receiver, but this does not affect the shape of the transfer function. The same happens also in the variation of D_e and the misalignments, so from now on only the values of the G_V's peak will be presented. That allows a better focus on the behavior of gain at its peak as a function of the treated parameter, and also to collect a larger amount of data in the same graph. The voltage distribution on the plane where the electrodes lay is shown in Fig. 3.17, where the color and data ranges are manually

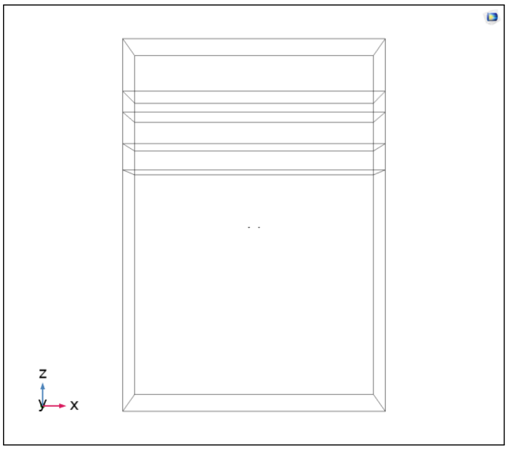

(a)

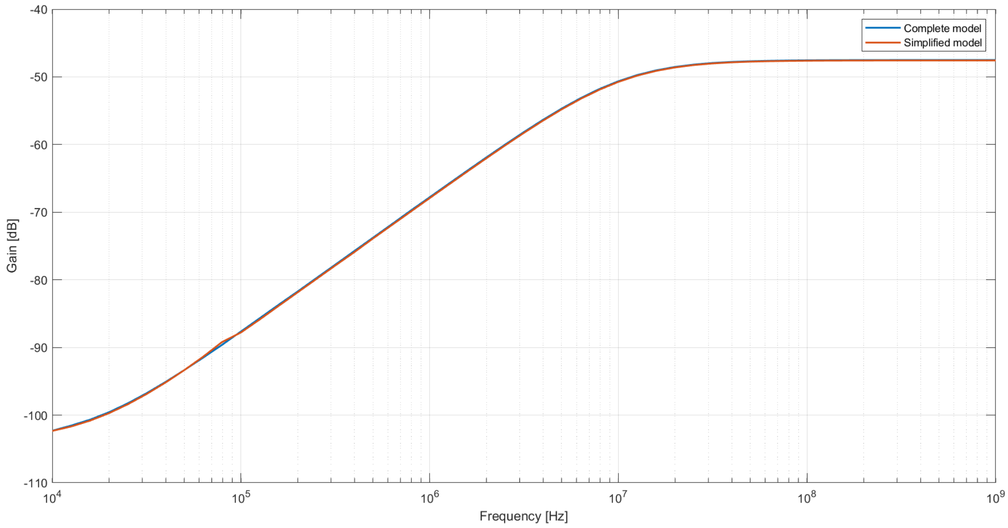

(b)

Figure 3.15: (a) Geometry of the simplified model (b) Comparison of the voltage-gain obtained with the complete model and the simplified one

limited to the minimum value of $-100\,\mathrm{dB}$ and the channel length is $5\,\mathrm{mm}$.

Fig. 3.18 presents an extension of the previous graph, enlarging the range of the channel lengths to $50\,\mathrm{mm}$. From that, it is possible to appreciate a decay of the voltage gain, which reflects the electric field distribution in space, as described in 2.1. Starting from the value of $-47\,\mathrm{dB}$ for $L_c = 2\,\mathrm{mm}$, the gain becomes $-70\,\mathrm{dB}$ for $L_c = 5\,\mathrm{mm}$ and then exactly $-100\,\mathrm{dB}$ for $L_c = 16\,\mathrm{mm}$, so a loose of $53\,\mathrm{dB}$ in less than $1.5\,\mathrm{cm}$. After that, just an additional attenuation of $22\,\mathrm{dB}$ happens if L_c is increased up to $50\,\mathrm{mm}$. This suggests that it is preferable to work with devices closer to each other not to incur an extremely high attenuation of the

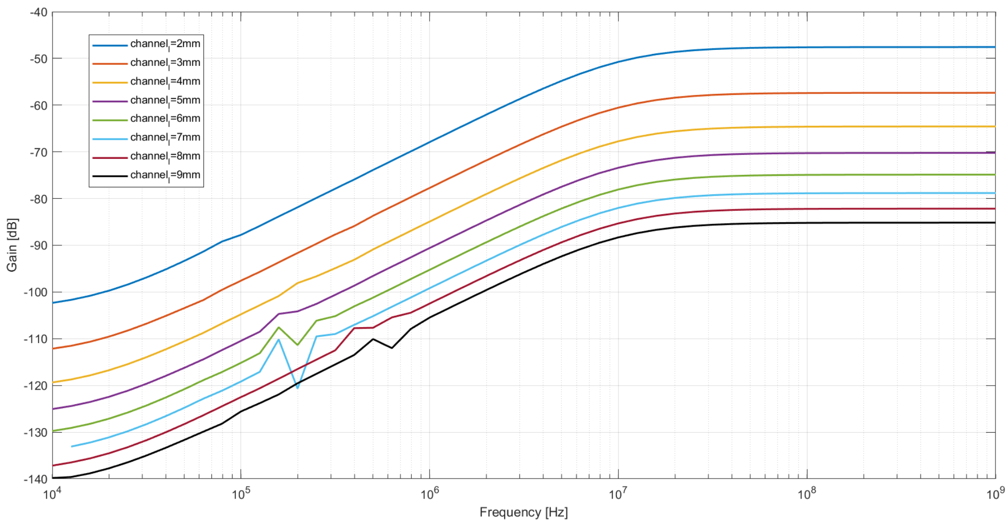

Figure 3.16: Voltage gain for channel length from 2mm to 9mm

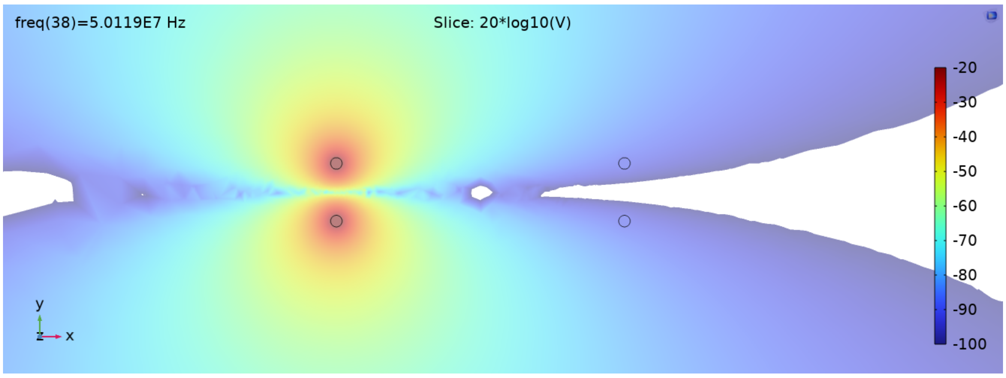

Figure 3.17: Voltage potential distribution on the electrodes' plane

transmitted signal, even if it must be taken into account that small misalignments in the proximity of the input can have a larger impact on the voltage gain.

The second key parameter to vary is the inter-electrode distance, fixing the channel length to a constant value. Since an acceptable gain is still possible to achieve with a distance between two different implants of 5 mm, that has been chosen to be the value of L_c for the next configurations. Remember that the dimensions of the electrodes themselves are the same as the ones in MODEL_1. The variation of D_e has been done in the range $[0.5\,\text{mm} - 2\,\text{mm}]$, and Fig. 3.19 depicts its consequences on the voltage gain peak: larger distances lead to lower attenuation with a fixed length of the communication. This can be explained by the fact that the closer are the input electrodes the higher is the current density focused

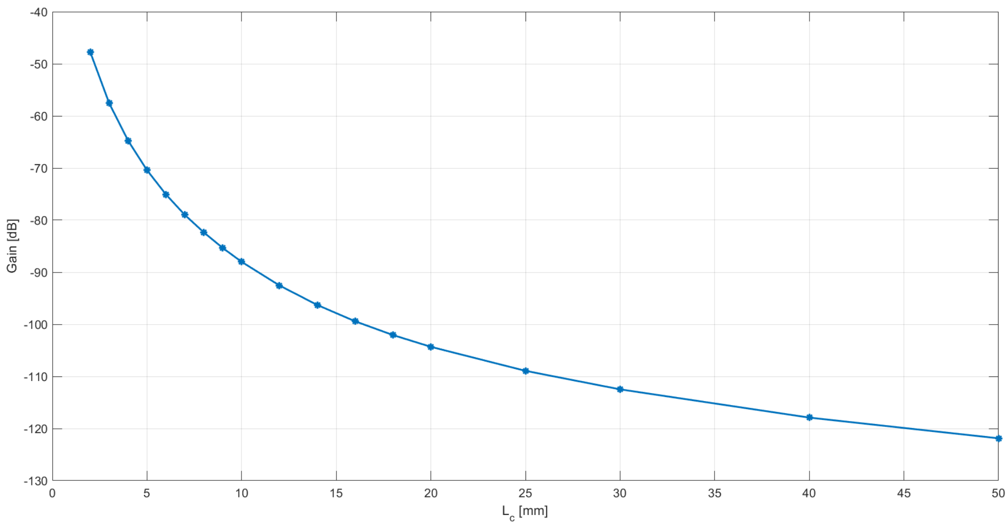

Figure 3.18: Variation of voltage gain peak for channel length from 2mm to 50mm

in the space between them, leading to a smaller amount of ionic current induced in the surrounding portion of the tissue. Since in galvanic BCC the secondary current flow is the one exploited to create the communication with the receiver, the phenomenon is then explained. As proof of the concept, a qualitative comparison of the current density distribution with $D_e = 0.5\,\text{mm}$ and $D_e = 2\,\text{mm}$ is shown in Fig. 3.20. In both images, the normalized current density ($[\,\text{A}\,\text{m}^{-2}]$) and the arrow lines of the current flows are superimposed on the plane of the two implants to appreciate at the same time the intensity of the current (which is also related to the intensity of the electric field) and the path followed by it. As the colors are assigned to the same values in (a) and (b), it is possible to notice that with a larger distance between the electrodes, the receiver is reached by a higher current density, but also that the current density in the space around the transmitter is much higher in the case of closer electrodes. This leads to a higher electric field between the transmitting electrodes in (a) and between the receiving electrodes in (b), meaning a higher chance of harmful effects on the tissue in (a) and higher voltage gain in (b). If the constraints on the dimension of the device were not strict, it is possible to conclude that a larger separation between the electrodes would be much more beneficial for both the transmission efficiency and the safety of the patient.

Another aspect that must be studied is the presence of some misalignments between the transmitter and the receiver that can happen during implantation. Up to now, it has been supposed that the two are perfectly aligned, which means

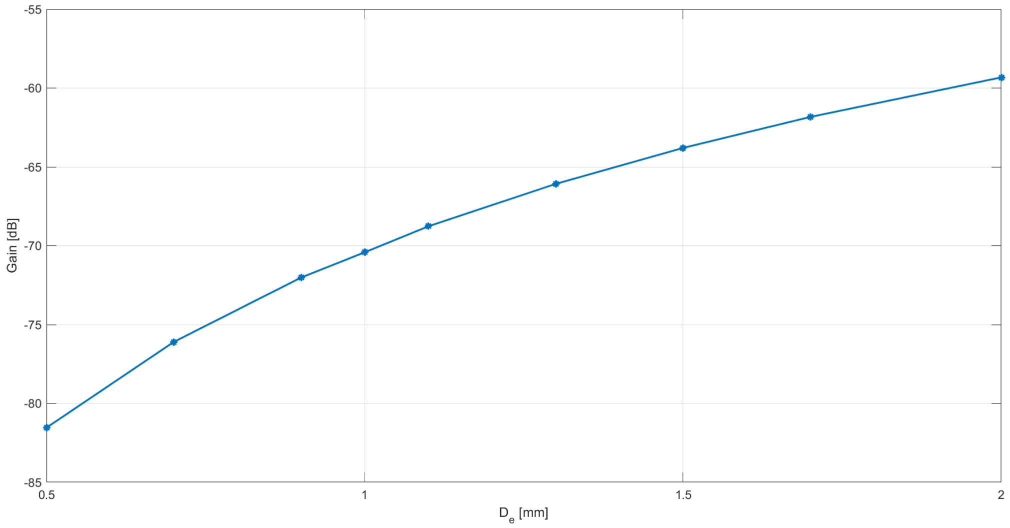

Figure 3.19: Variation of voltage gain peak for inter-electrode distance from 0.5mm to 2mm

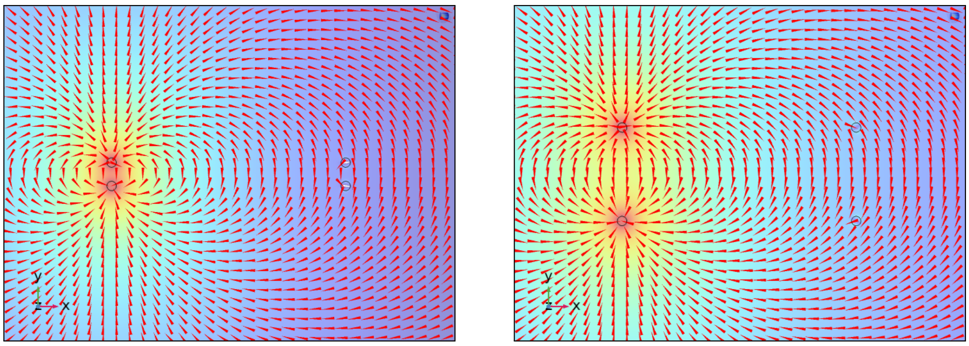

(a) **(b)**

Figure 3.20: Current density and current flows for (a) $D_e = 0.5\,\text{mm}$, (b) $D_e = 2\,\text{mm}$

laying on the same plane, parallel and in front one to the other. To be clearer, the model has been built with the vertical direction assigned to the z-axis, the channel length along the x-axis, and the devices, so the two electrodes, aligned in the direction of the y-axis. So, supposing the upper electrode of the transmitter in position (x_{t1}, y_{t1}, z_{t1}) the others has been placed as in Fig. 3.21. In order to simulate some deflections from this ideal situation two kinds of misalignments have been simulated: angular misalignment, making the receiver rotate around an axis, and spatial misalignment, moving it on the y or z direction and fixing the transmitter.

Regarding the angular misalignment, the rotation angle around the x-axis that moves the electrodes on the plane orthogonal to the one of the transmitter has been called θ, while the rotation angle around the z-axis that produces a movement of the electrodes on the same plane as the transmitter has been called α. The values of the voltage gain peak have been investigated for both θ and α ranging between $-90\,°$ and $90\,°$, obtaining Fig. 3.22 and 3.23. From those, it is possible to observe how the transmission is not affected by angular misalignments in a relevant manner up to $\pm 60\,°$, losing only around 5 dB. Then, for an increase of other $25\,°$ until $\pm 85\,°$, the gain changes from -76 dB to -91 dB. The worst case happens from $\pm 85\,°$ to $\pm 90\,°$, with a sudden drop of about 80 dB. The huge decrease only for angles very close to $\pm 90\,°$ is well explained by looking at Fig. 3.17. Due to the differential communication, the upper electrode transmits a positive voltage and the lower electrode a negative voltage, both with almost the same amplitude. Therefore, it happens that on the points in the middle of the couple of transmitting electrodes and along the plane orthogonal to the direction of the device, the voltage nearly cancels out in a sort of destructive interference. With $\pm 90\,°$ misalignments, the receiving electrodes lay exactly on those points where the absolute value of the voltage is at the minimum.

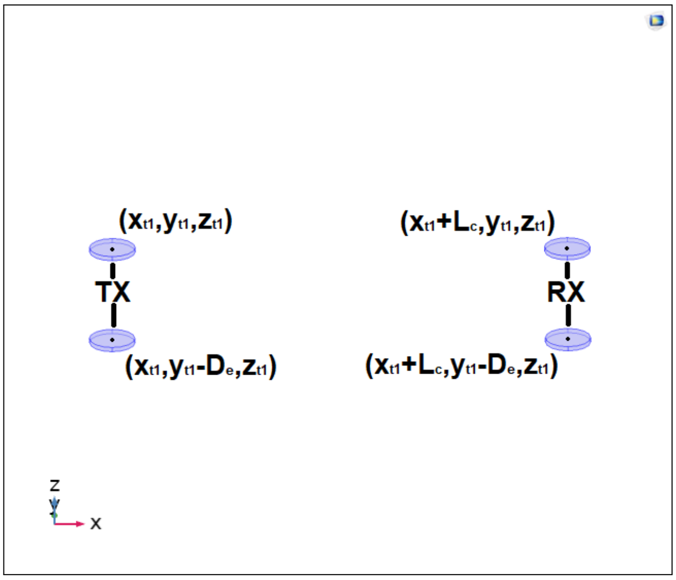

Figure 3.21: Coordinates of the transmitting and receiving electrodes before misalignments

As for spatial misalignment, the effect of an unwanted shift of the receiver in the y or in the z direction has been analyzed. Working with 1 mm devices, the range of misalignments has been taken up to ± 1 mm, referring with the quantities Δy and Δz to the values of the shift from the default position. Fig. 3.24 and 3.25

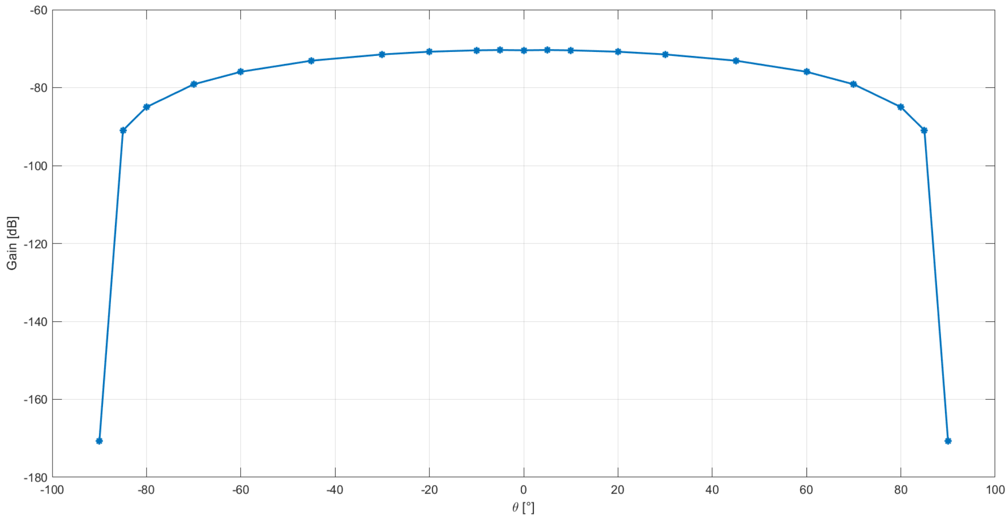

Figure 3.22: Variation of voltage gain peak for planar angular misalignment from -90° to +90°

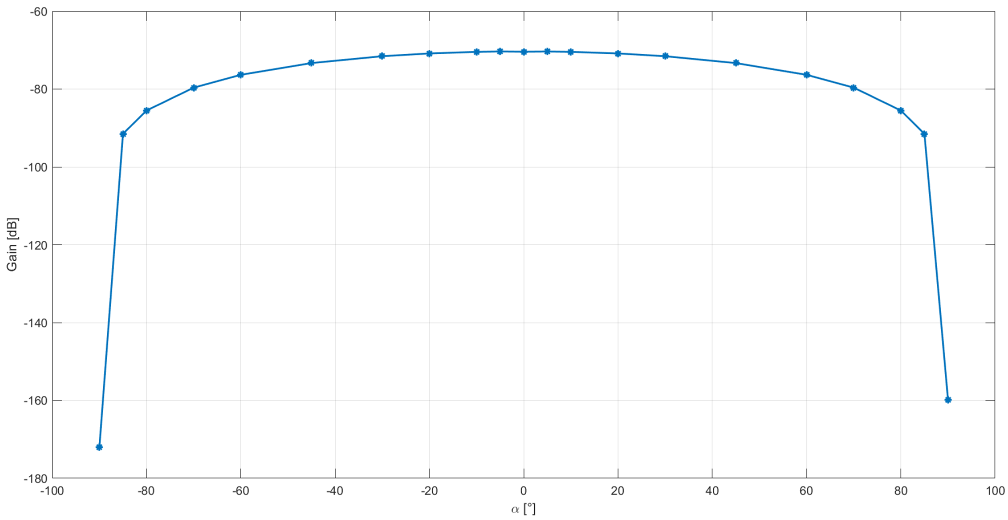

Figure 3.23: Variation of voltage gain peak for orthogonal angular misalignment from -90° to +90°

present the results from the simulations, from where it is possible to notice that the robustness against misalignments is maintained and also improved with the respect to the angular case. In the observed range, only a 1 dB maximum loss can be appreciated in both directions, but while in the y direction the curve of the gain is perfectly symmetrical for negative and positive Δy, it seems that positive Δz lead to slightly higher attenuation. Another interesting aspect is that for Δy equal to ±0.1 mm and ±0.2 mm the gain appears higher than the optimal alignment case, even if it can be an artifact of the simulation and the improvement is less than 0.1 dB, so it is not prudent to draw consequences from that.

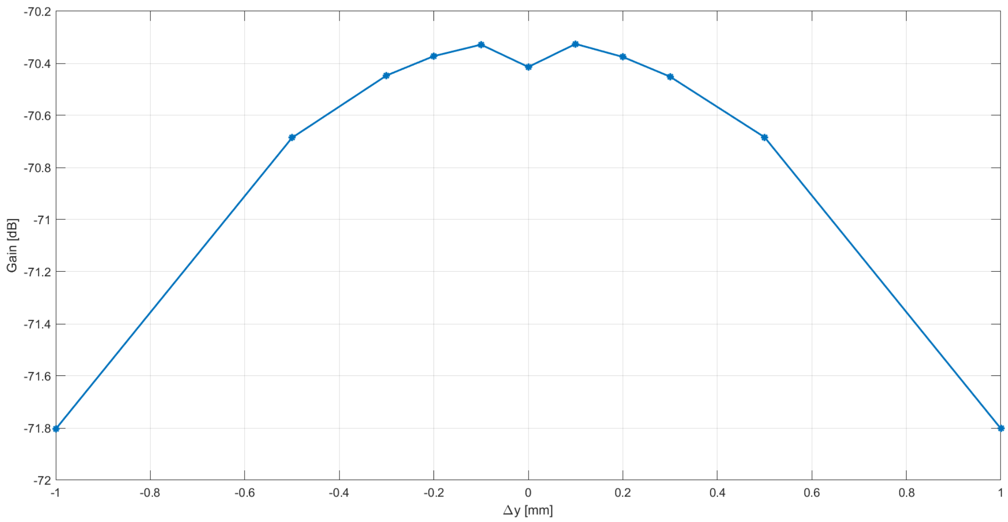

Figure 3.24: Variation of voltage gain peak for planar spatial misalignment from -1mm to +1mm

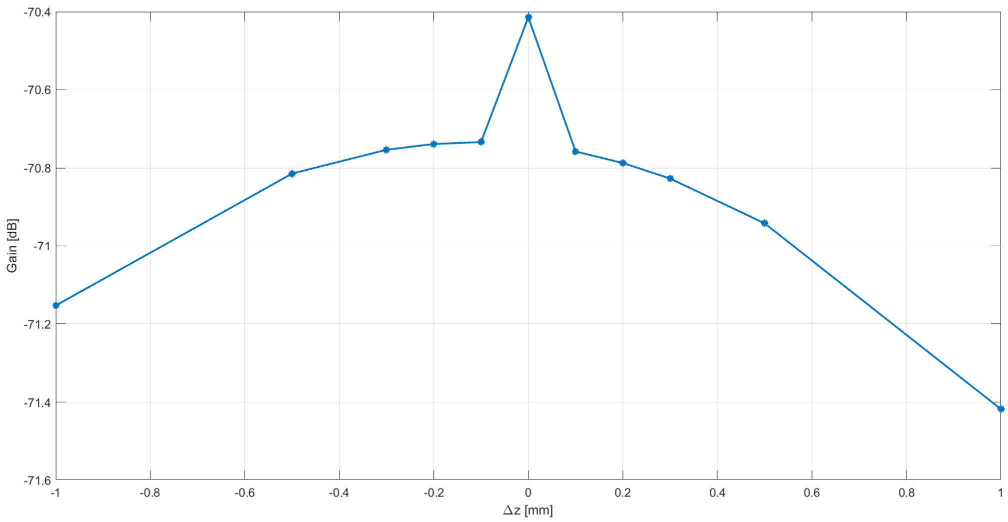

Figure 3.25: Variation of voltage gain peak for orthogonal spatial misalignment from -1mm to +1mm

After the purely geometrical tests, other studies have been carried out. One is related to the tissue the devices are implanted into, since up to this point they have been placed in the white matter only. Taking again MODEL_1, where L_c is just 2 mm, the depth of the implants has been changed to place them into the grey matter instead, modifying their z coordinate and leaving all the other parameters as they are. Fig. 3.26 compares the transfer functions obtained in the two cases. The gain achievable with transmission through the grey matter tissue is comparable even if to some degree higher (less than 1 bB) in the flat region after the cut-off frequency, but considerably higher in the region before it, with an improvement of almost 10 dB in some points. This is given by the higher conductivity of the grey matter, as shown in Fig. 3.3. Also, a shift of the cut-off frequency to around 4.6 MHz can be noted, useful to obtain a wider flat curve at the peak value of the gain. The cause is probably the difference in the tissues' relative permittivity too.

With the knowledge of the characteristics of transmission through grey matter, a communication between two different layers has been investigated. To do so, three different devices have been implanted one on top of the other with 2 mm separation, thinking of a vertical channel instead of horizontal, similar to the one in [30]. The geometry of such disposition is displayed in Fig. 3.27a. The first test has been done by making the device in grey matter transmit and looking at the received voltage of the upper device in white matter, the second simulates the inverse, and in the last one, a vertical transmission in the white matter only has been tested from the upper to the downer device. The obtained transfer functions (Fig. 3.27b) have a similar shape to the ones seen up to now, but the cut-off frequency of the second configuration changes from 10 MHz to 4.5 MHz. That is expected with a channel composed of different media since different dielectric characteristics must be combined and they can also lead to some reflections at the interface, but it is not found in the first case. Looking at the peak values of the gain in the three situations, the highest is obtained with the transmitter in the grey matter (-44 dB) due to the fact that the electric field decays with a decreasing ratio moving far from the source, so placing the transmitter in the more conductive material helps to get lower attenuation where the field is stronger. The lowest gain occurs in the second test (-51 dB), maybe due to some phenomena at the interface that can get the signal attenuated in the second medium or produce interference with reflections. Finally, comparing the horizontal and the vertical transmissions with a channel length of 2 mm in Fig. 3.28, it can be deduced that, as far as the devices are well aligned, the communication is independent on its direction with a fixed channel length.

A different material for the electrodes has been tried to see whether it has a noticeable impact on the transfer function. Using the values in Tab. 3.2 for Z_P and assigning the proper dielectric properties ($\epsilon_r = 1$ and $\sigma = 9.43 \times 10^6$ S/m) to the cylinders representing the electrodes, Platinum has been used to replace Copper in

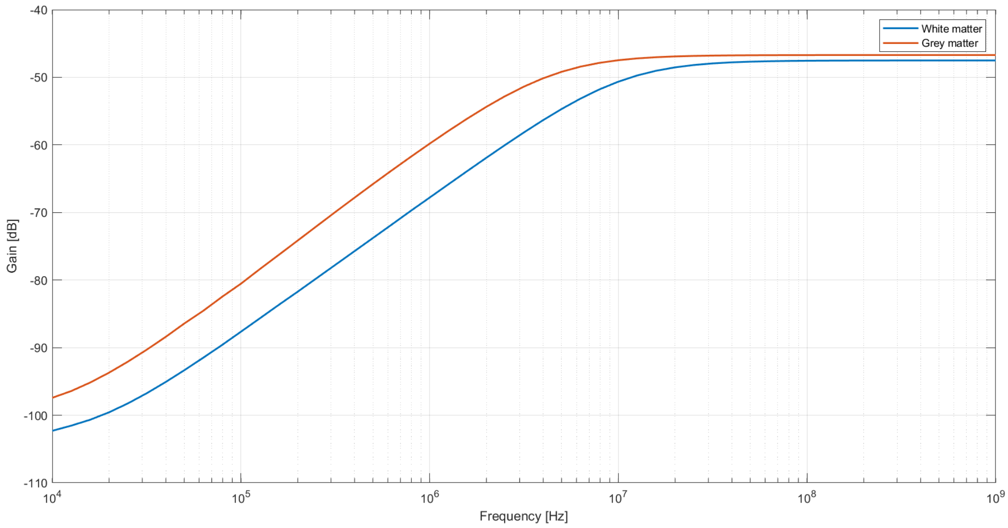

Figure 3.26: Voltage gain for implantation in white matter and grey matter

the simulation. Despite that, no noticeable changes can be observed in Fig. 3.29, because both Cu and Pt have an electrical conductivity several orders of magnitude greater than the biological tissues.

Moving to some variations in the coupled circuits, some values in the ranges $[50\,\Omega - 1\,\mathrm{M}\Omega]$ and $[20\,\Omega - 1\,\mathrm{k}\Omega]$ have been assigned to R_L and R_S respectively. This study has been limited to the frequency values in $[100\,\mathrm{kHz} - 100\,\mathrm{MHz}]$ to make the huge number of parametric simulations lighter. The results of that are not appreciable on the gain in the case of R_S (Fig. 3.31), while it happens that for increasing values of R_L the transfer function changes its shape, flattening and shifting the cut-off frequency to lower values, but keeping the same peak value. This can be useful for some applications where a lower operating frequency can be exploited, without the disadvantage of a non-flat gain over the specific bandwidth.

The last set of simulations has focused on introducing a higher number of implants, instead of looking at the transmission between a couple of them only. The main reason for this analysis is to understand whether the quality of the received signal can be influenced by the presence of many scattered devices in the interested region. To do that, models with three and four devices have been built, where there is only one transmitter and two or three receivers, each one coupled with a load resistance $R_L = 50\,\Omega$.

The first model has three couples of electrodes with the same $D_e = 1\,\mathrm{mm}$ placed on a circumference so that the central point of each device is $2\,\mathrm{mm}$ distant from the others (Fig. 3.32a). In other words, the center of each implant is on a vertex of

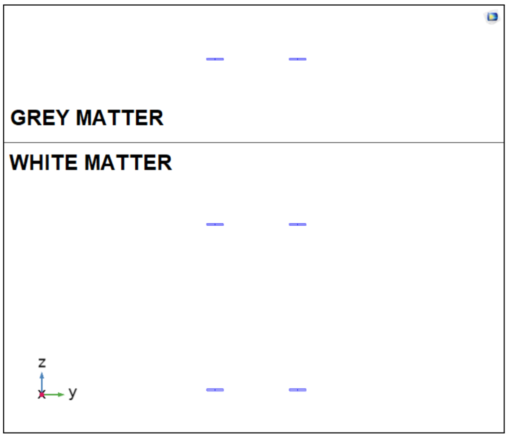

(a)

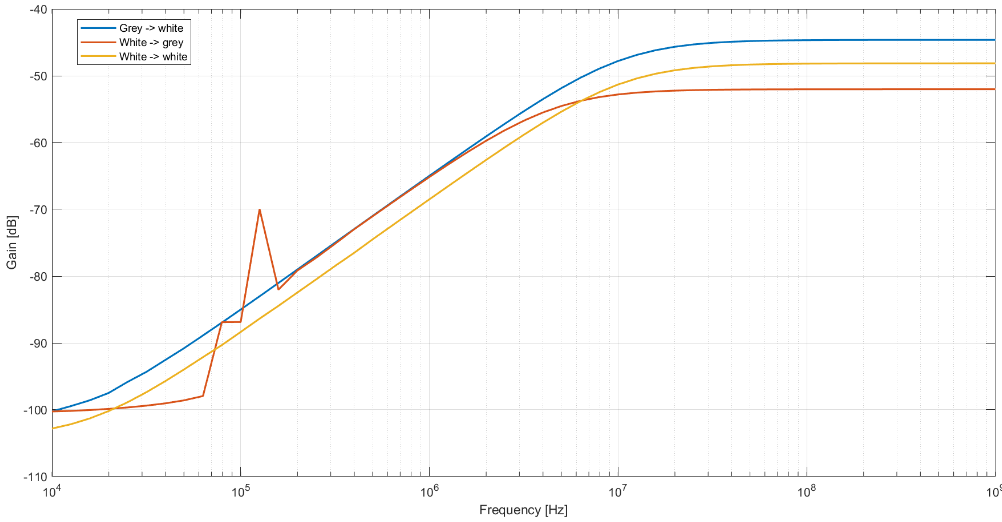

(b)

Figure 3.27: (a) Geometry of three devices in different media (b) Voltage gain for vertical transmissions between grey matter and white matter

an equilateral triangle with 2 mm edge. The transmitter is on the left side, while the two receivers (called "RX1" and "RX2") are on the right side. Looking at the gain of both RX1 and RX2, it is interesting to see that their curves are exactly the same and the peak value is even 2 dB higher that the one obtained with a single receiver with a channel length of 2 mm.

In the second model, another device is added and they all are placed on each side of a 2 mm x 2 mm square as in Fig. 3.33a. The transmitter is still on the left, and the three receivers RX1, RX2, and RX3 on the right, but this time the channel lengths are not equal. The distance TX-RX2 is exactly 2 mm, while the

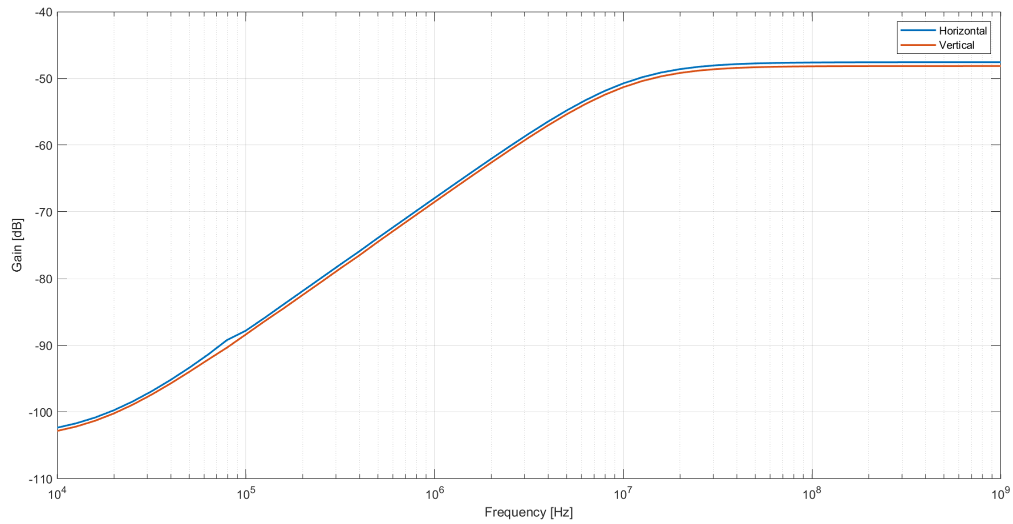

Figure 3.28: Voltage gain for horizontal and vertical channel of 2 mm in white matter

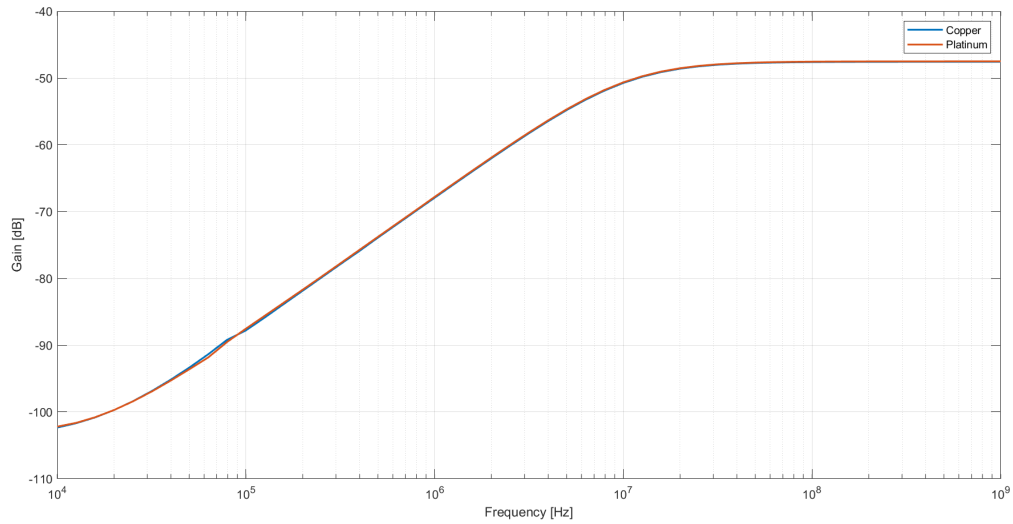

Figure 3.29: Voltage gain for copper and platinum electrodes

other two, TX-RX1 and TX-RX3, are shorter. Another difference is that RX2 is perfectly aligned and faces TX, while it is like RX1 and RX3 have gone into a shift Δy and a rotation θ, referring to the misalignments treated before, but starting from a position where the channel length would have been only 1 mm. These considerations reflect on the voltage gain curves in Fig. 3.33b: RX1 and RX3, being closer to TX, show a higher gain, although the misalignments, with the same transfer function, and RX2 seems not to have consequences from the

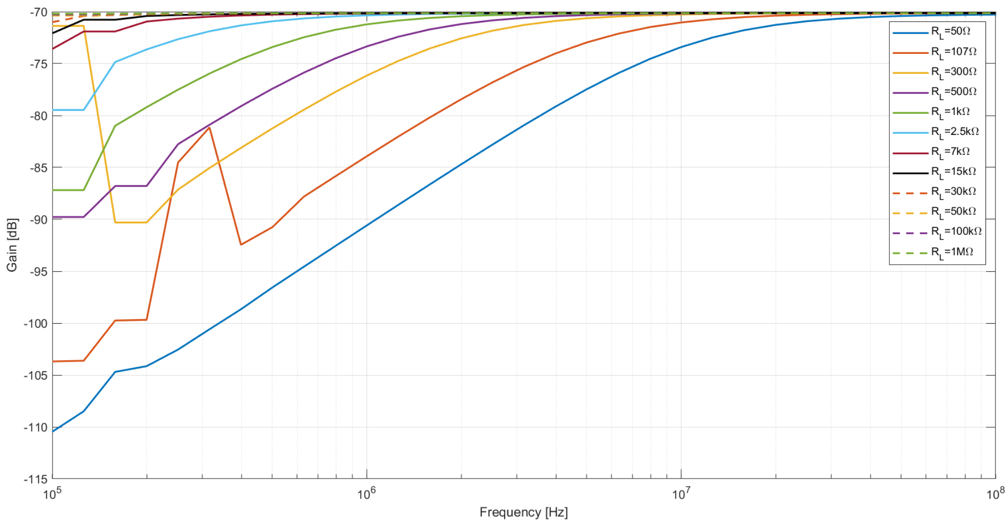

Figure 3.30: Voltage gain for variations of R_L value

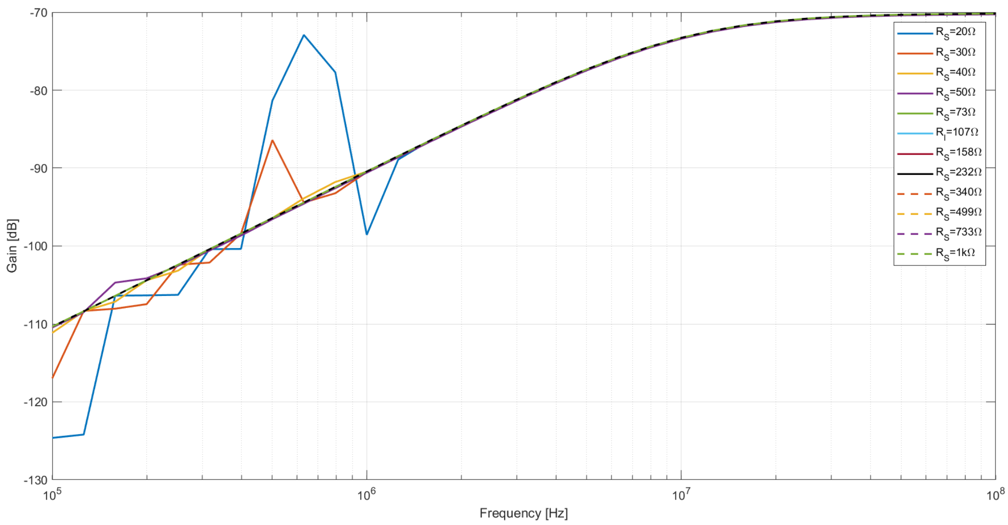

Figure 3.31: Voltage gain for variations of R_S value

presence of the other devices. Its gain has been compared to the one of the device in the same position without the other implants (from Fig. 3.16), and indeed they are very similar in Fig. 3.34. The transfer function of the device in the network looks slightly shifted to lower frequencies, with a few dB increase in the slope and a quite lower cut-off frequency.

The third model with a sort of network of implants tests the presence of three devices in line to look at a possible shadowing effect between the two receivers. Starting with the first receiver RX1 at a channel length of 2 mm, a second one has

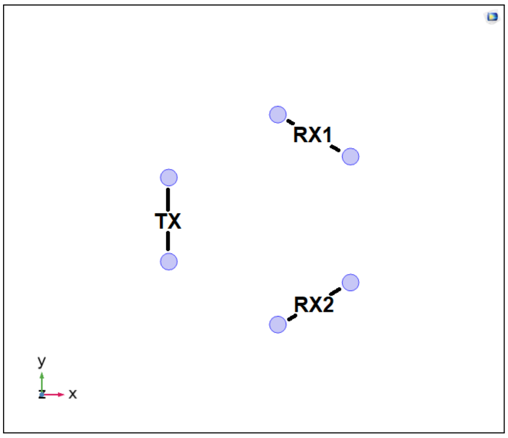

(a)

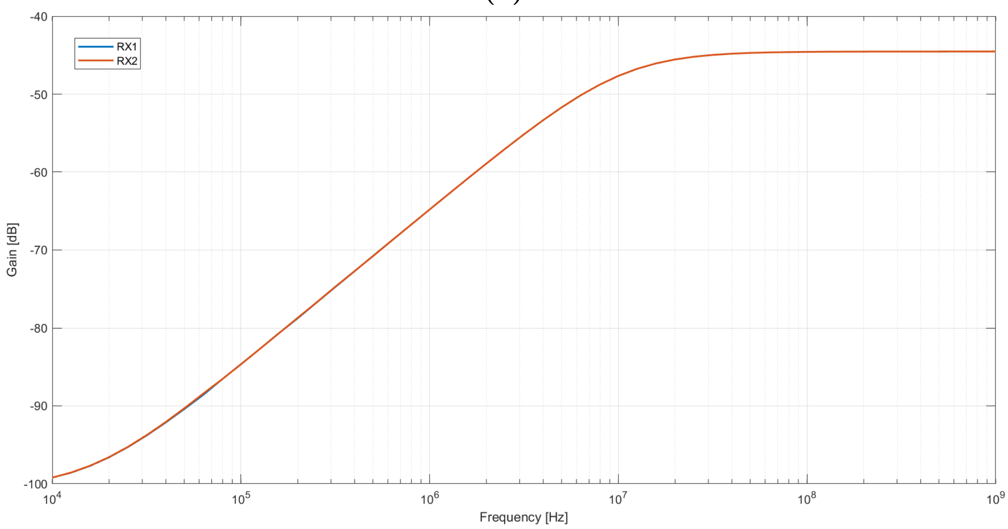

(b)

Figure 3.32: (a) Geometry of the three devices network (b) Receivers' voltage gain in the three devices network

been placed with a channel length of 5 mm. The geometry of this arrangement is shown in Fig. 3.35a. The gain of both RX1 and RX2 has been directly plotted together with the one of single devices with $L_c = 2\,\text{mm}$ and $L_c = 5\,\text{mm}$ respectively in Fig. 3.35b, and they match perfectly. This avoids the presence of shadowing effects, as in the previous cases.

In the end, looking at the results of multiple implants, it is possible to derive the fact that in the receiving phase, the devices do not interfere with each other, maintaining the same values of voltage gain as they were alone. Even more, small changes happen only when multiple devices share the same current flow created by

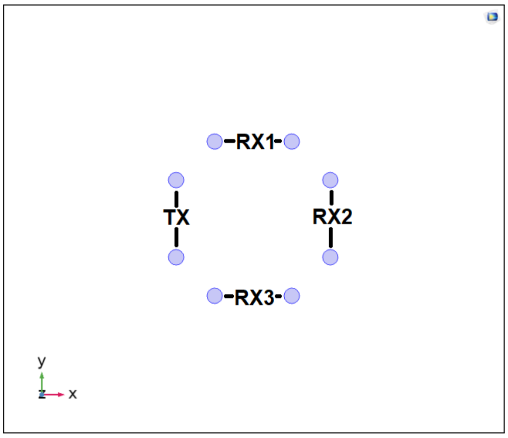

(a)

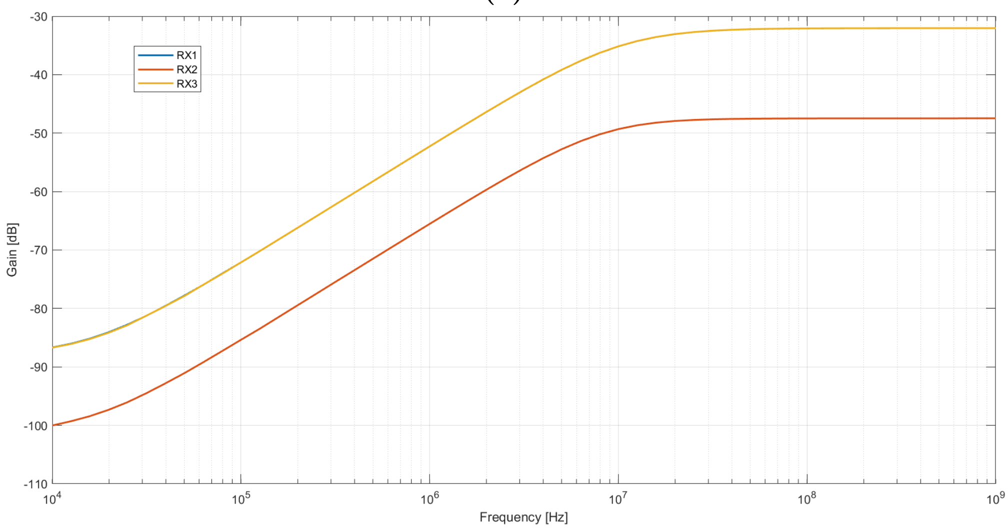

(b)

Figure 3.33: (a) Geometry of the four devices network (b) Receivers' voltage gain in the four devices network

the source. This is the reason behind the frequency shift in Fig. 3.34 where the devices' alignment follows the path of the current, but not in 3.35b.

After the analysis of the variations of the parameters and the configurations, compliance with the safety regulations has been briefly studied. As expressed in 2.3.2 the two quantities to look at are the spatial average (as RMS) of the electric field over a 2 mm x 2 mm x 2 mm volume of contiguous tissue and the spatial average (as RMS) of the SAR over a 10 g volume of contiguous tissue. The two equations 2.7 and 2.8 have been used to make the calculations, where the volume integrals can

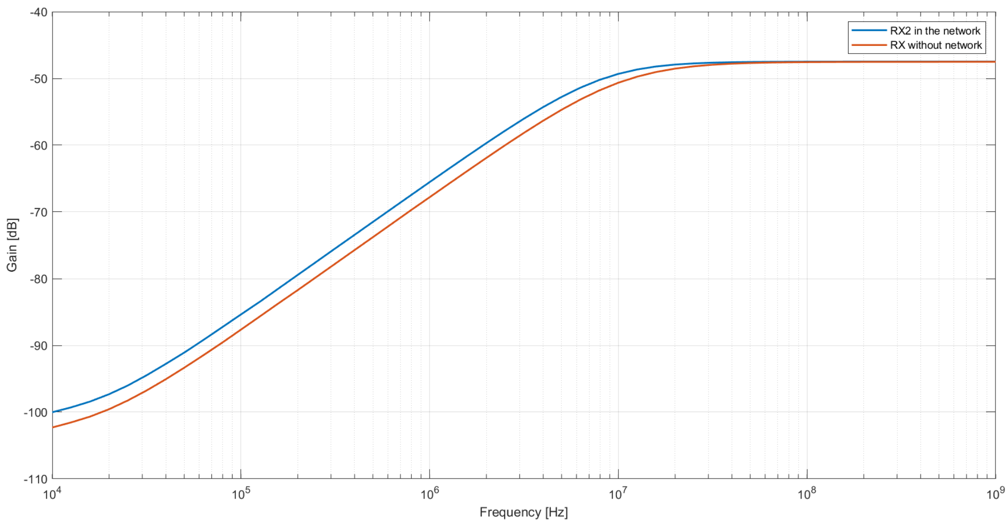

Figure 3.34: Voltage gain with and without the other devices in the network

be extracted from COMSOL®, defining geometrical boxes of the specific dimension during the first steps of the model building. Those boxes have been placed around the transmitting electrodes since the highest values of the electric field are localized right on their surface. The dimension of the box containing 10 g of white matter has been calculated from the average density of the material taken from [39], which is 1041 kg/m^3. Therefore, the volume containing 10 g of white matter has been defined as a 2.12 cm x 2.12 cm x 2.12 cm box around the transmitting electrodes. Also, different input voltages have been simulated, making the amplitude of the voltage generator V_{IN} vary from 0.3 V to 1 V. The results are shown in Fig. 3.36 and 3.37 for the electric field and SAR respectively, together with the related basic restrictions from ICNIRP. While the SAR limitations are respected for any frequency value and input voltage, the electric field values exceed the maximum allowed value for frequencies up to around 1 MHz. Clearly, the higher the input voltage in the circuit the higher the average electric field induced in the tissue, so for increasing V_{IN} the compliance is achieved for higher frequency values only. Regarding the contact current, it has been assumed to be the current injected into the tissue from the positive electrode of the transmitter. That has been compared with the reference levels in Fig. 3.38. For any input voltage considered and within the entire frequency range, the values are lower than the maximum allowed, even if very close around 10 MHz for $V_{IN} = 1$ V, suggesting that only a small increase in the input voltage could be permitted.

However, an additional surprising phenomenon appears in the behavior of the average electric field and SAR with respect to frequency. Indeed, for high frequency starting from about 10 MHz the curves drop, while the opposite was expected since

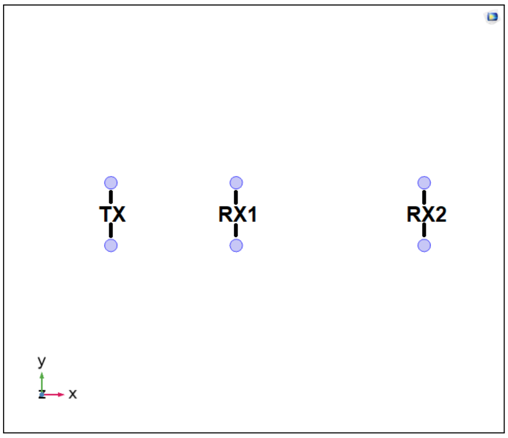

(a)

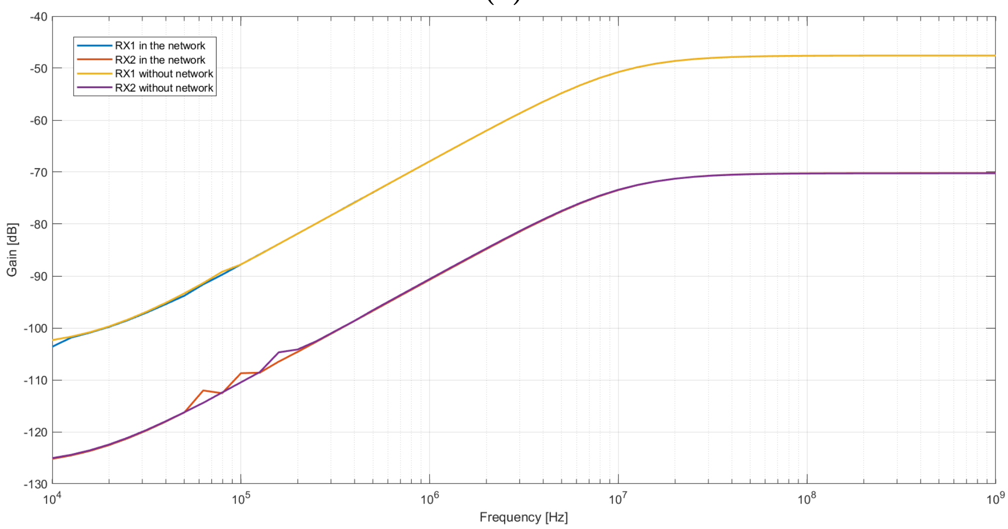

(b)

Figure 3.35: (a) Geometry of the three devices in line network (b) Receivers' voltage gain in the three devices in line network and without the network

the gain peak is in that range. To investigate more, the transmitted voltage V_T has been observed for different channel lengths, inter-electrode distances, and internal and load resistances. Where it is not explicit, the resistors have been left at the default value of $50\,\Omega$. In Fig. 3.40 it can be noted that, unless a change in R_S from the default value, the transmitted voltage is constant for low frequencies and then decreases starting from 10 MHz. A higher value of R_S leads to a drop for lower frequencies, and a lower value of R_S leads to a drop for higher frequencies.
From Fig. 3.31 it has been previously deduced that a variation of R_S does not affect the voltage gain, so to understand the reason for the shape of G_V the received

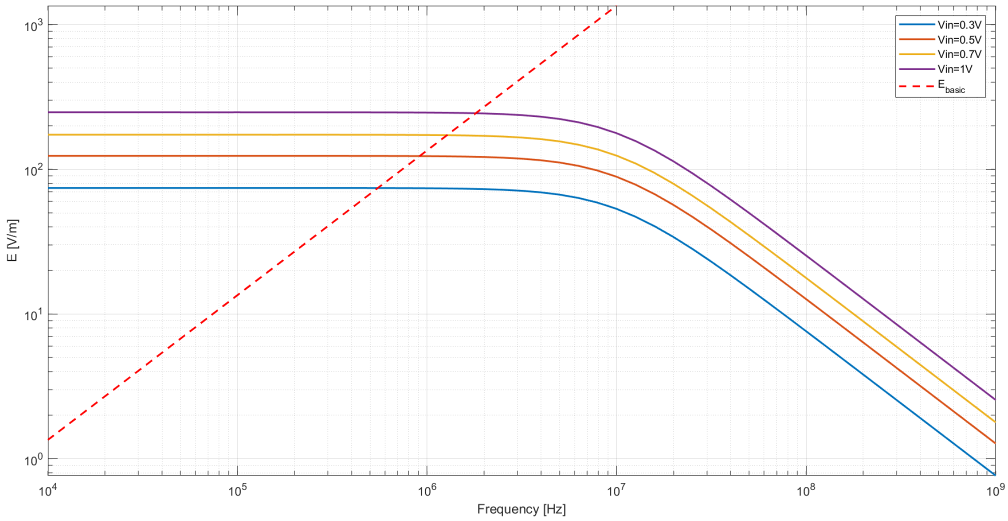

Figure 3.36: Electric field intensity for different input voltages and related basic restrictions

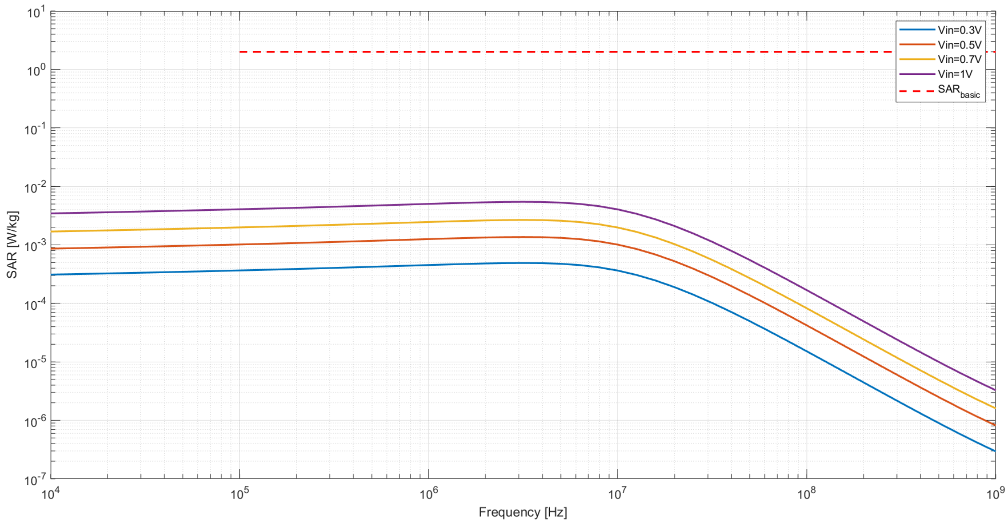

Figure 3.37: SAR_{10g} for different input voltages and related basic restrictions

voltage V_R has been analyzed as well, for the same configurations as V_T. Fig. 3.40 depicts the behavior of V_R as a function of frequency for different configurations. The same drop of the voltage gain just after 10 MHz is observed in the cases where the 50 Ω resistors have been used. When R_S is increased or decreased with respect to the default value, the same effect as in V_T is shown. Differently from V_T, an increase of R_L has an impact on V_R. Exactly as the effect on G_V seen in Fig. 3.30, an increase of R_L means a reduction in the slope of the received voltage before the

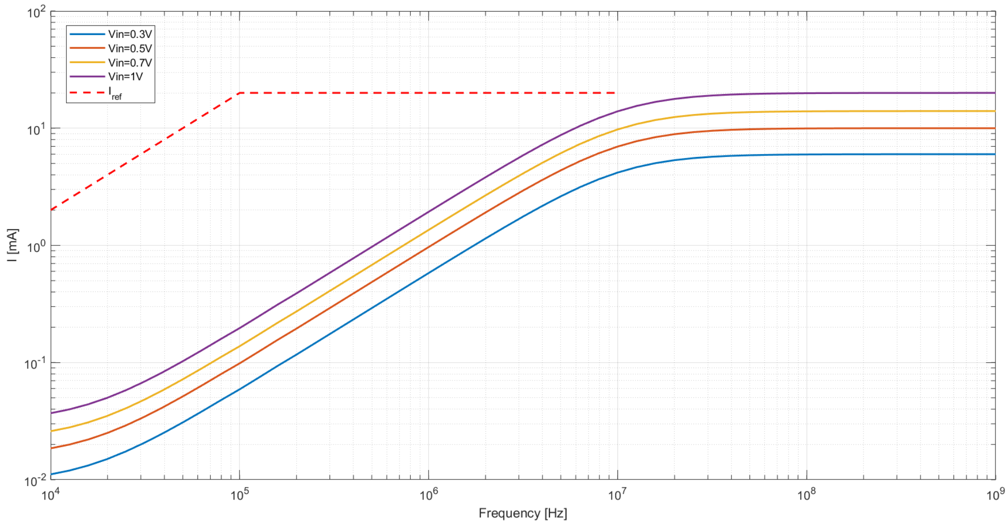

Figure 3.38: Contact current for different input voltages and related reference level

peak and for $R_L = 1\,\mathrm{M\Omega}$ it is completely flat.
The reason behind the flat gain after 10 MHz is explained by the decrease in V_T and V_R with the same ratio starting from this frequency value. However, the cause of the unexpected sudden drop of the electric field in the model still has no explanation and further research has to be done in this direction.

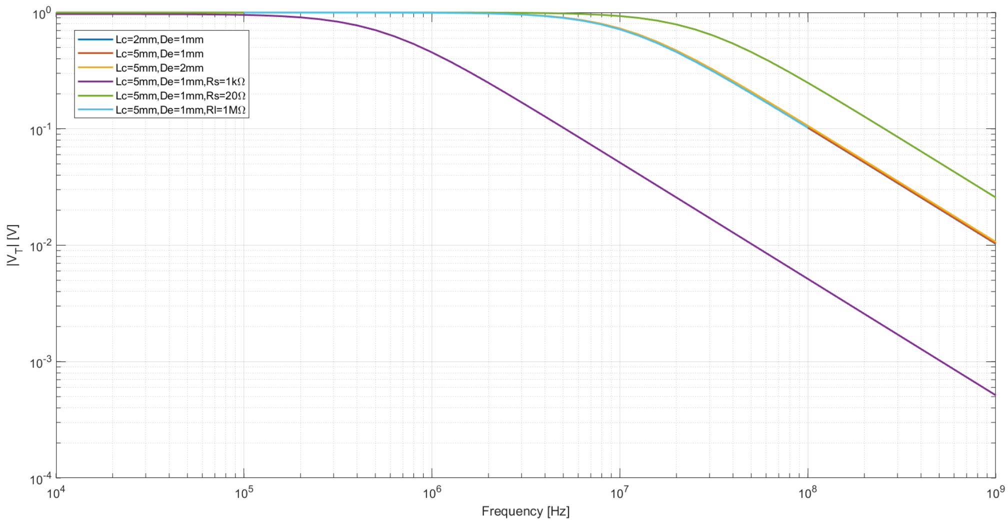

Figure 3.39: Transmitted voltage for different configurations

Taking into account such results, a final simulation with both $R_S = 20\,\Omega$ and

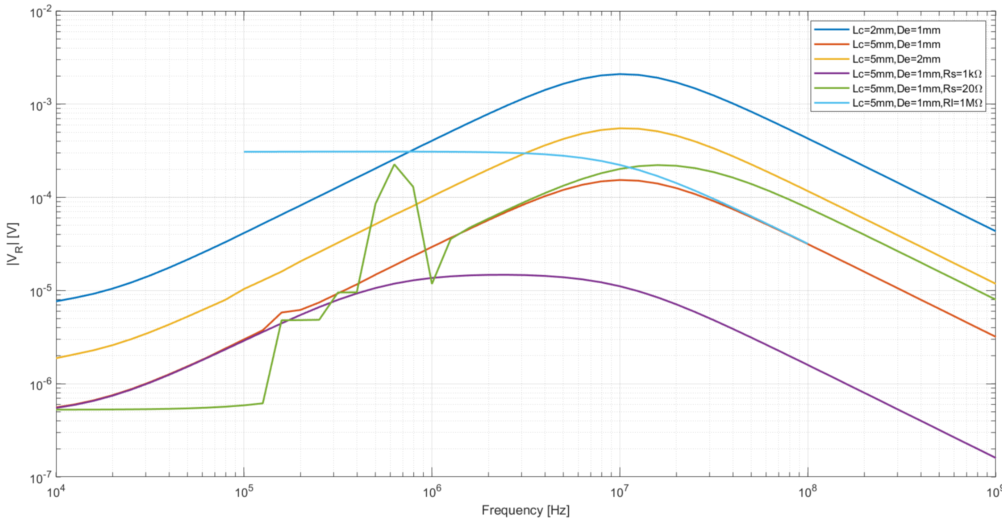

Figure 3.40: Received voltage for different configurations

$R_L = 1\,\mathrm{M\Omega}$ has been carried out, supposing it could merge the benefits coming from a higher R_L and a lower R_S. From Fig. 3.41 and 3.42 it is possible to see some improvements in both G_V and V_R with respect to the default configuration. The transfer function is completely flat for the entire frequency range and the received voltage is slightly higher at the peak around 10 MHz, 0.3 mV instead of 0.16 mV, even though the drop happens starting from the same frequency and not how Fig. 3.40 shows for $R_S = 20\,\Omega$.

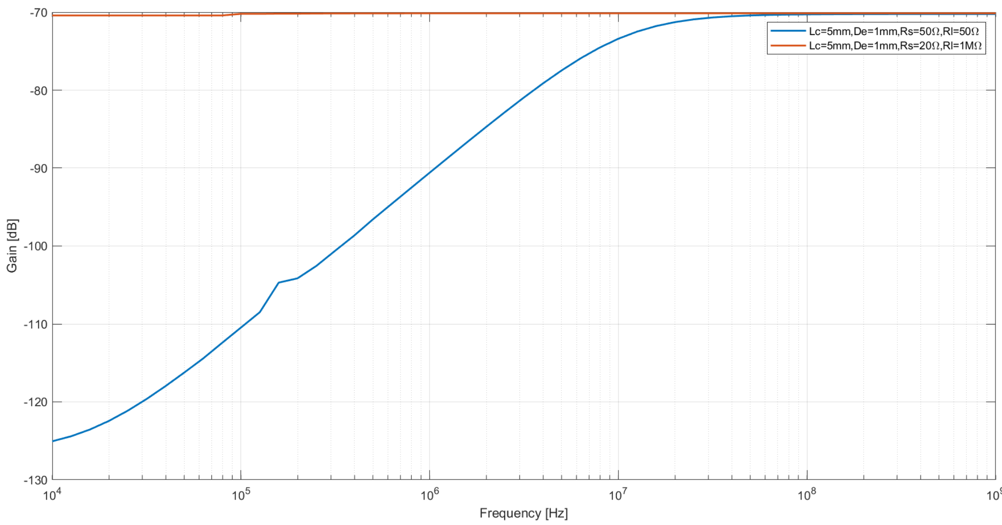

Figure 3.41: Transmitted voltage for the supposed optimal configuration

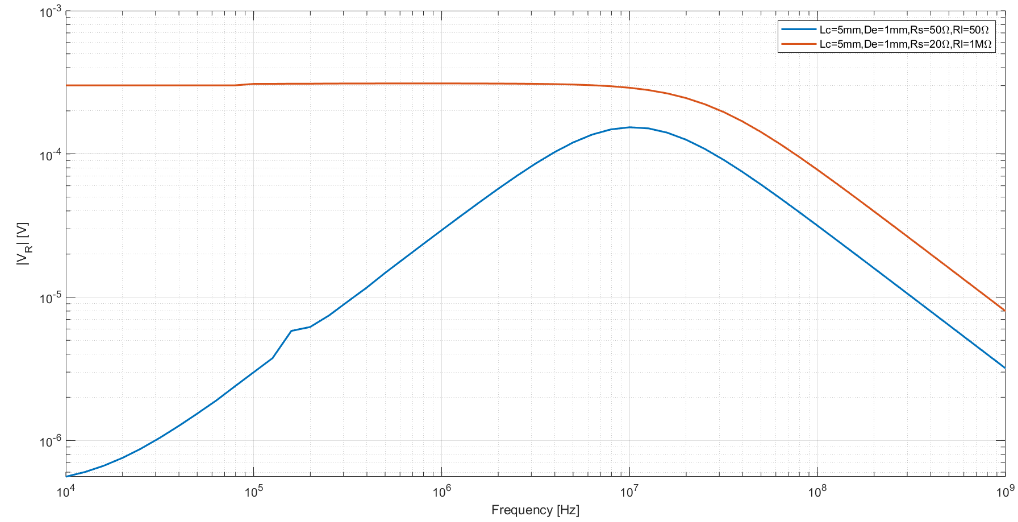

Figure 3.42: Received voltage for the supposed optimal configuration

In the end, Fig. 3.43 and 3.44 display the input impedance Z_{IN}, evaluated as the ratio between the transmitted voltage V_T and the current injected into the tissue, i.e. the current flowing out of the positive transmitting electrode. From those, it is interesting to notice that Z_{IN} does not change either its shape or values for any configuration, it decreases almost constantly for increasing frequency in a range from tens of kΩ to less than $1\,\Omega$, and its phase is always negative, showing a resistive and capacitive characteristic. This is in agreement with the findings in [16].

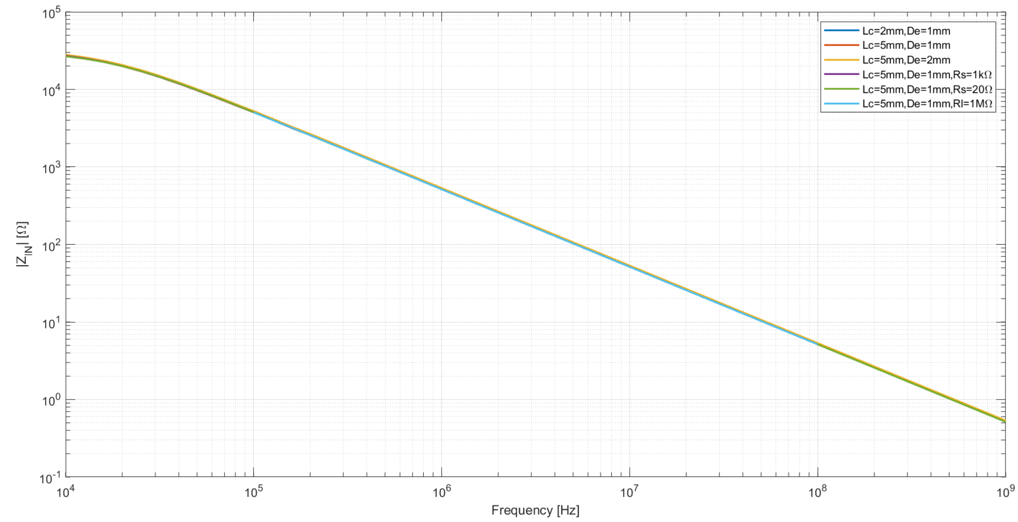

Figure 3.43: Input impedance amplitude

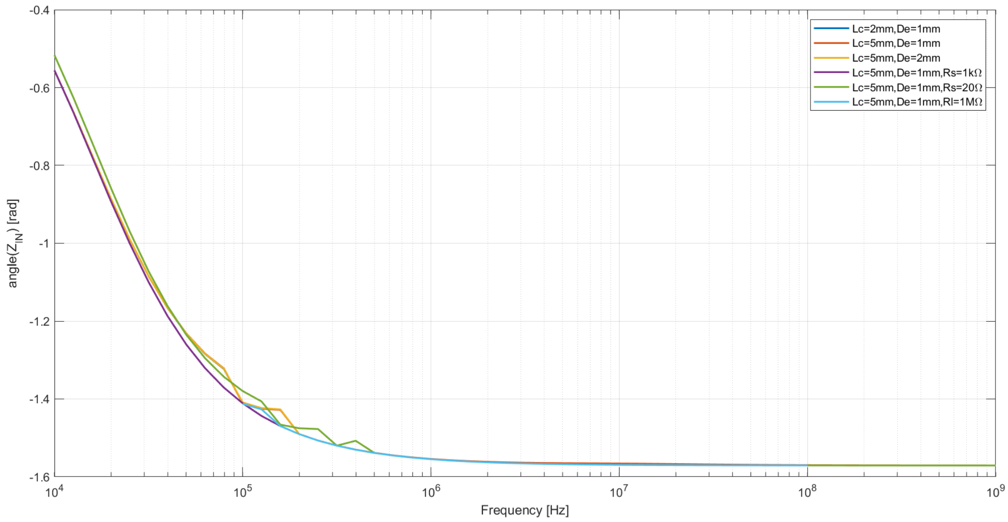

Figure 3.44: Input impedance amplitude

Chapter 4

Conclusions And Future Works

This thesis presents a detailed study of adopting galvanic BCC for a network of wireless micro-scale brain implants, using FEM simulations. The study involves the construction of a layered sphere model, representing the human head, and pairs of copper electrodes, representing the implants, using COMSOL Multiphysics®. Various factors including electrode geometry, channel length, misalignments (both angular and spatial), and source/load resistances are examined to analyze their impact on the voltage gain between the transmitting and receiving electrodes.
The simulations show that proportional scaling of the channel and electrode dimensions toward micro-scale implants degrades the absolute peak of G_V, necessitating higher sensitivity at the receiver. At the same time, the peak of the received voltage moves to higher frequencies, allowing for an improvement in the data rate. The communication channel shows great robustness against different misalignments and shading by other implants, making it suitable for freely floating micro-scale implants in the brain. Finally, compliance with safety regulations is explored which shows no safety hazard for operating frequencies exceeding 1 MHz and input signal amplitude lower than 1 V.

4.1 Discussions About Results

The main contributions of this work are:

- characterization of the frequency response of galvanic coupling signal excitation in the two main tissues of the human brain, the grey and the white matter
- analysis of the impact of the miniaturization of a couple of galvanic BCC devices up to 1 mm on the voltage gain

- analysis of the impact of the variations of some geometrical parameters, like channel length, inter-electrode distance, different misalignments, location of the implants whitin ranges suitable for the specific application
- analysis of the impact of the variations of the generator's internal resistance and the load resistance on the voltage gain
- analysis of the impact of the introduction of additional devices, up to four, in a galvanic BCC small network
- analysis of the compliance with safety regulations in terms of electric field intensity and SAR for micro-scale implants.

In light of the numerous results shown in 3.3 it is possible to conclude that: This thesis presents a detailed description of the characteristics of a galvanic BCC transmission between a few micro-scale devices in the human brain. The results obtained are in part in line with the expectations and in part not predicted. In particular, the electric field decrease in the whole model for high frequency shows an unexpected behavior and still needs to be deeper investigated. Taking into account such behavior, the best configuration obtained in this work is shown to be the combination of a low and a high value of R_S and R_L respectively, and the choice of 10 MHz as transmitting frequency to obtain the best performance between the configurations analyzed. That allows for a transmission with acceptable values in terms of voltage gain up to a few cm between devices. Also, this is sustained by the good robustness against misalignment which is useful for the movement of the implants in the brain. Regarding safety, no harmful effects of electrostimulation and temperature increase are observed if the operating frequency is higher than 1 MHz. However, additional effects related to the current density must be studied.

4.2 Missing Considerations And Possible Extensions

Some aspects of this work can be deepened and some others can be extended. Here is a list of suggestions:

- investigation of the minimum voltage or current value required at the receiver side to allow for robust transmission of data from the transmitter
- evaluation of the order of magnitude of the power consumed by transceivers with the characteristics explored in this thesis
- deeper study on the electric field drop for frequencies higher than 10 MHz

- deeper study on the polarization impedance values, and the effects of the phenomena at the electrodes' interfaces
- further analysis of the effects produced by current density with values in the range obtained with the scaling
- comparison with the characteristics achievable with a capacitive coupling implant at the maximum dimension scaling

4.3 In The Future

Starting from the conclusions obtained, the next steps that could continue the investigation of this thesis are:

- verification of the results with measurements
- investigation of the modulation technique to use depending on the characteristics described to enhance the transmission
- study of the effects of a simultaneous transmission from more than one device
- definition of a network protocol that allows for an increase in the number of the considered device and the management of the conflicts between them.

Appendix A

Details Of COMSOL Model

A practical guide on how to properly configure COMSOL to obtain the model used in this thesis.

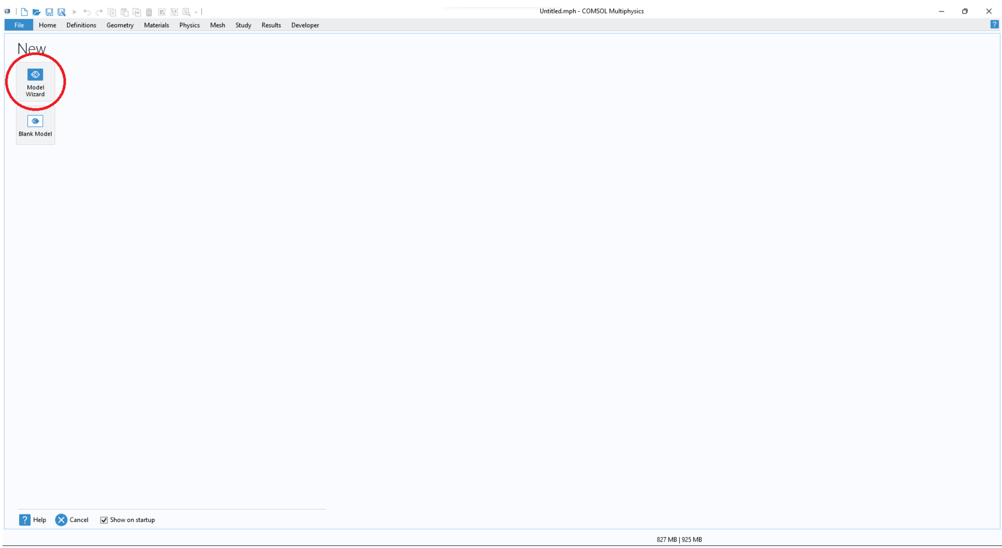

Figure A.1: STEP 1: Open a new file and select Model Wizard

.

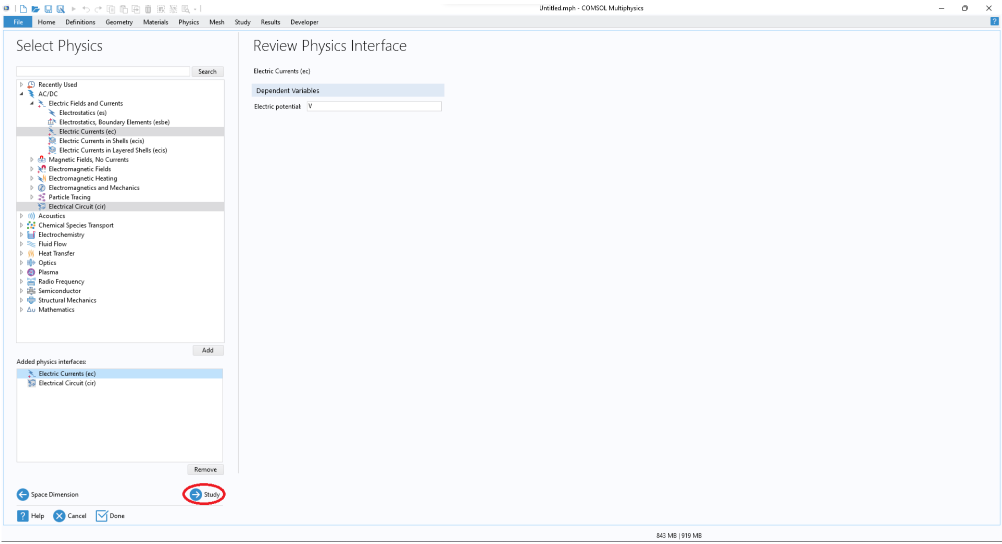

Figure A.2: STEP 2: Select AC/DC - Electric Fields and Currents - Electric Currents(ec), then Add and AC/DC - Electrical Circuit (cir), then Add. Once they are in the Added physics interfaces list, select Study

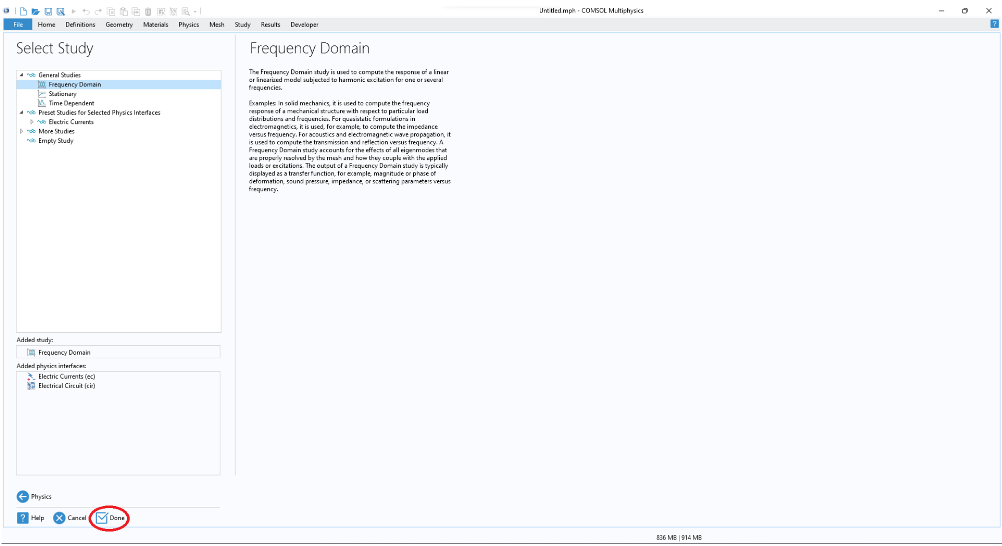

Figure A.3: STEP 3: Select General Studies - Frequency Domain, then Done

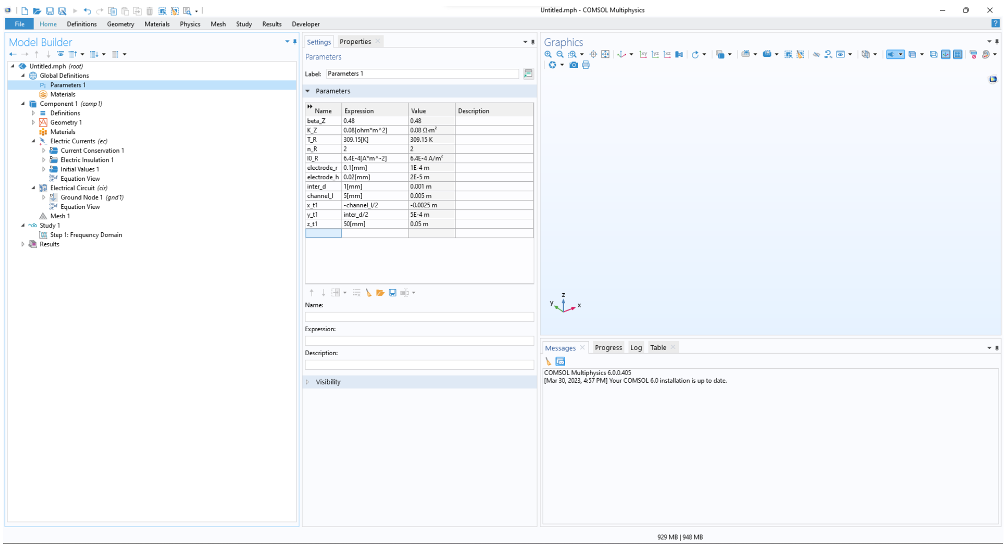

Figure A.4: STEP 4: In Model Builder select Global Definitions - Parameters 1. In Settings tab select Parameters and insert the fields Name and Espression as in Tab. A.1

Name	Expression
beta_Z	0.48
K_Z	0.08[ohm*m^2]
T_R	319.15[K]
n_R	2
I0_R	6.4E-4[A*m^-2]
electrode_r	0.1[mm]
electrode_h	0.02[mm]
inter_d	1[mm]
channel_l	5[mm]
x_t1	-channel_l
y_t1	inter_d/2
z_t1	50[mm]

Table A.1: COMSOL Parameters

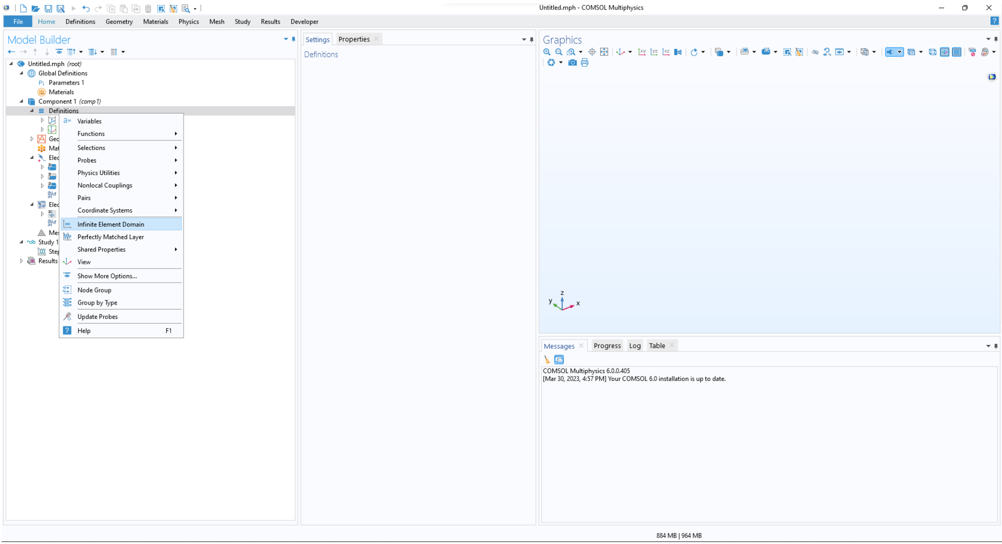

Figure A.5: STEP 5: In Model Builder right-click on Definitions, then select Infinite Element Domain

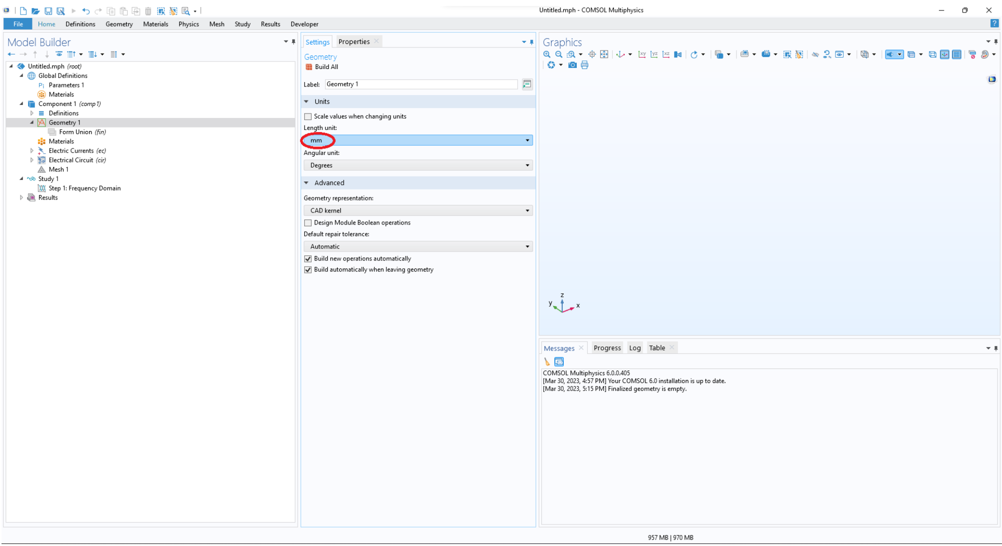

Figure A.6: [

STEP 6: In Model Builder select Geometry 1. In Settings tab select Units, then choose mm under Length unit:

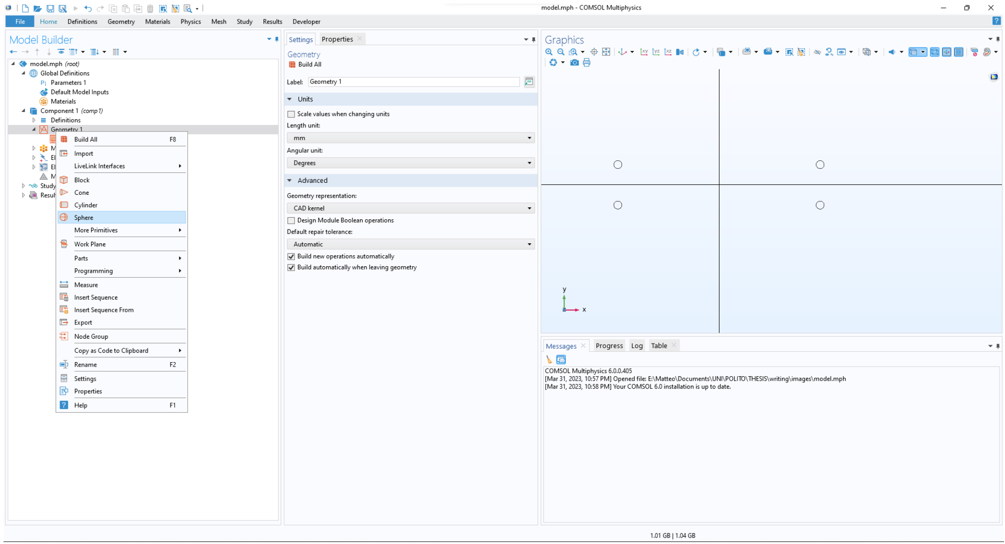

Figure A.7: STEP 7: In Model Builder right-click on Geometry 1, then select Sphere

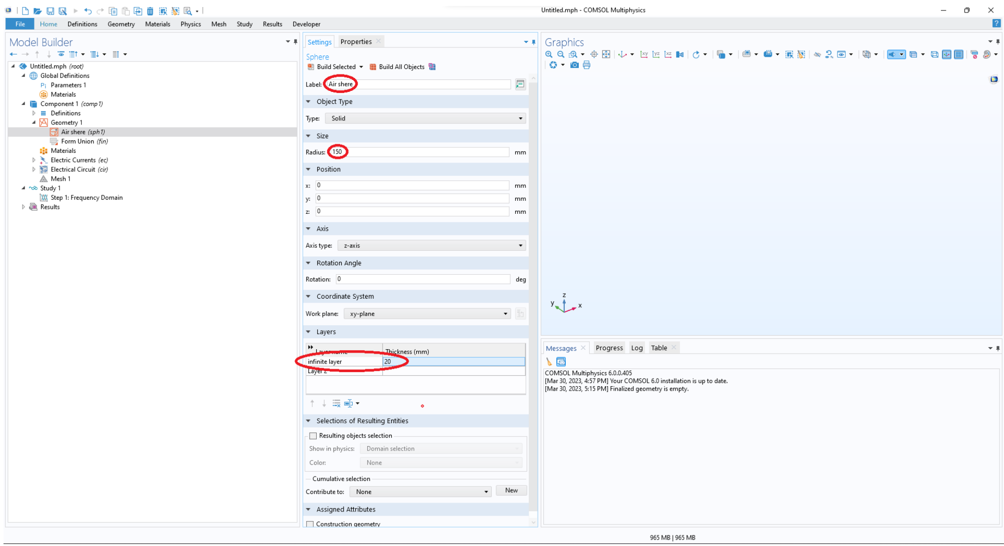

Figure A.8: STEP 8: In Settings tab fill Label and Radius as in the picture, then select Layers and fill Layer name and Thickness (mm) as in the picture

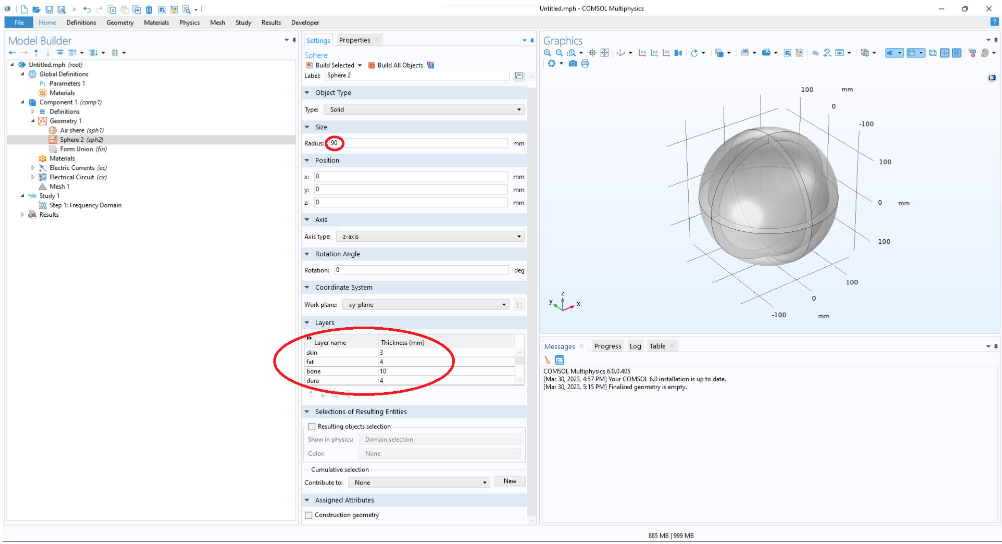

Figure A.9: STEP 9: Add another Sphere, then in Settings tab fill Radius as in the picture, then select Layers and fill Layer name and Thickness (mm) as in Tab. 3.1

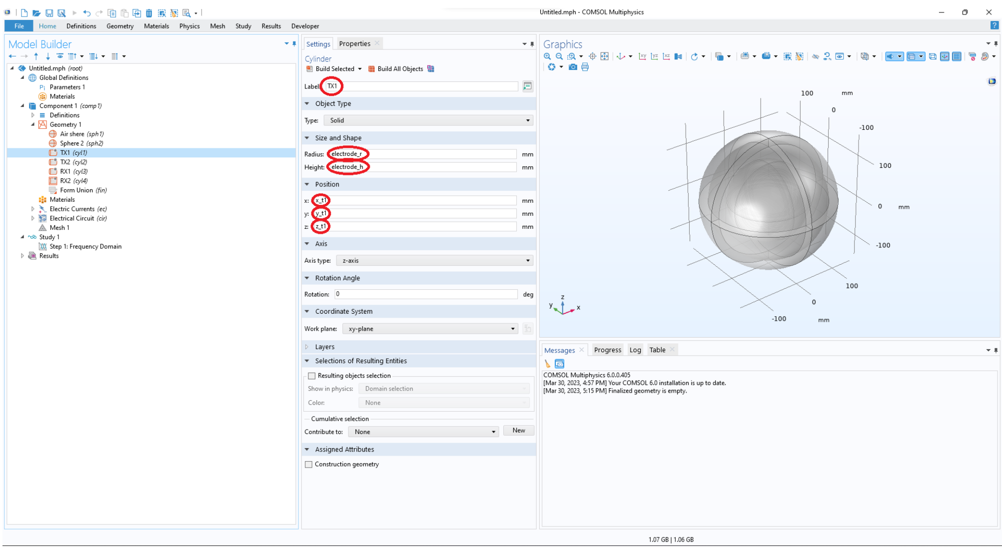

Figure A.10: STEP 10: Add a Cylinder, then fill Label, Radius, Height, x, y, and z as in the picture

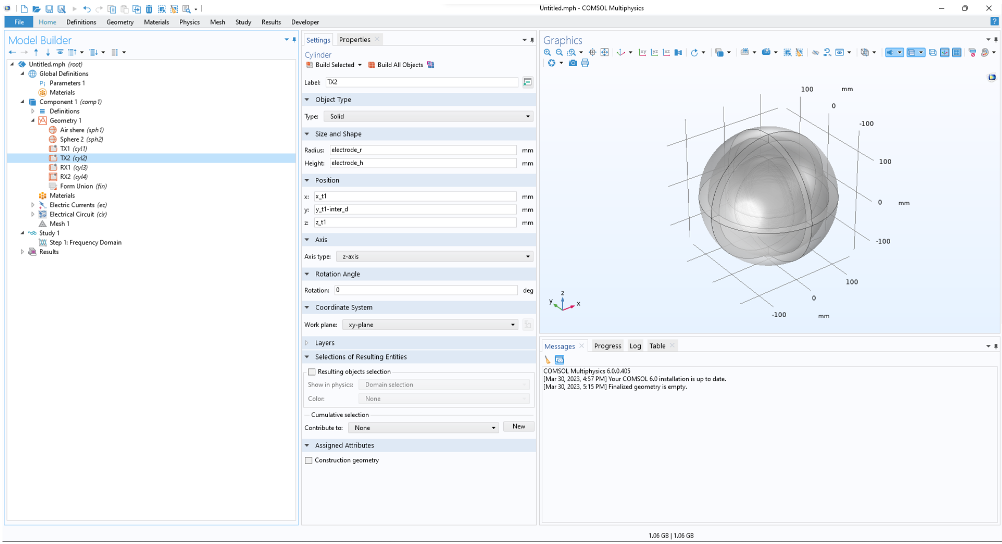

Figure A.11: STEP 11: Add another Cylinder, then fill Label, Radius, Height, x, y, and z as in the picture

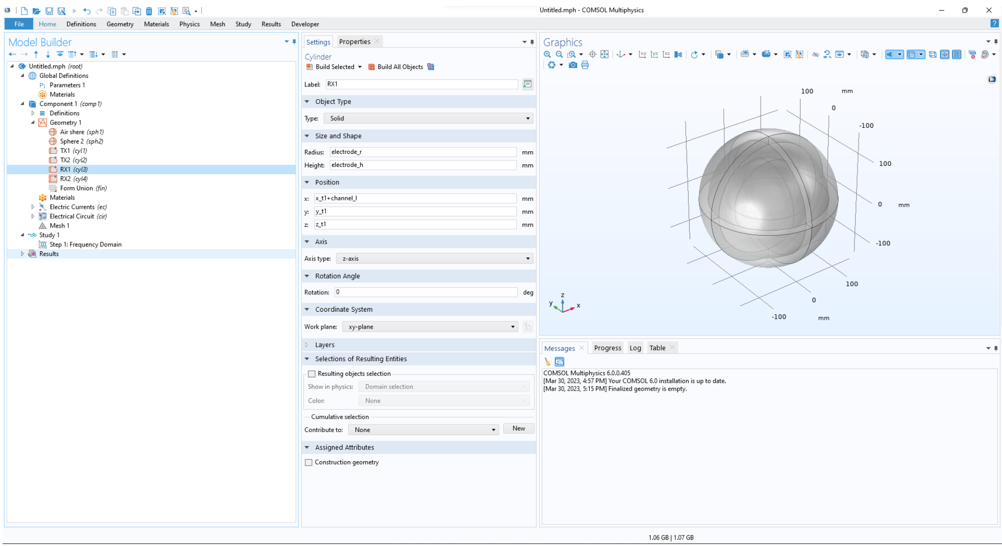

Figure A.12: STEP 12: Add anothe Cylinder, then fill Label, Radius, Height, x, y, and z as in the picture

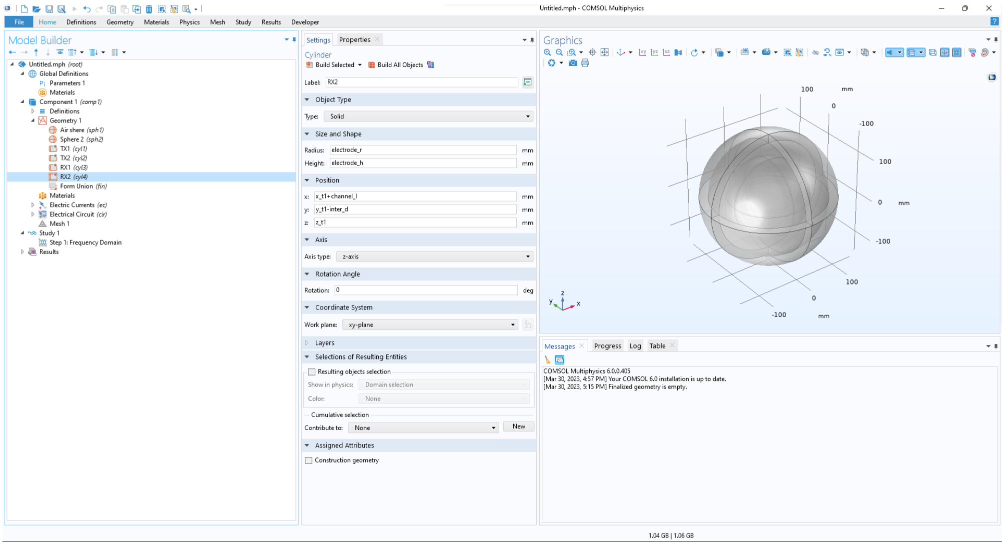

Figure A.13: STEP 13: Add another Cylinder, then fill Label, Radius, Height, x, y, and z as in the picture

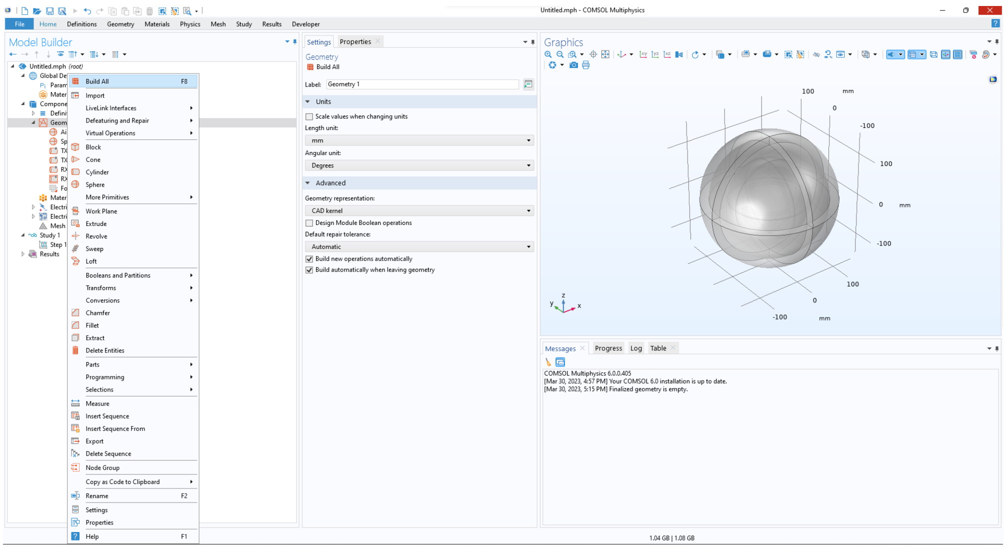

Figure A.14: STEP 14: In Model Builder right-click on Geometry 1, then select Build All

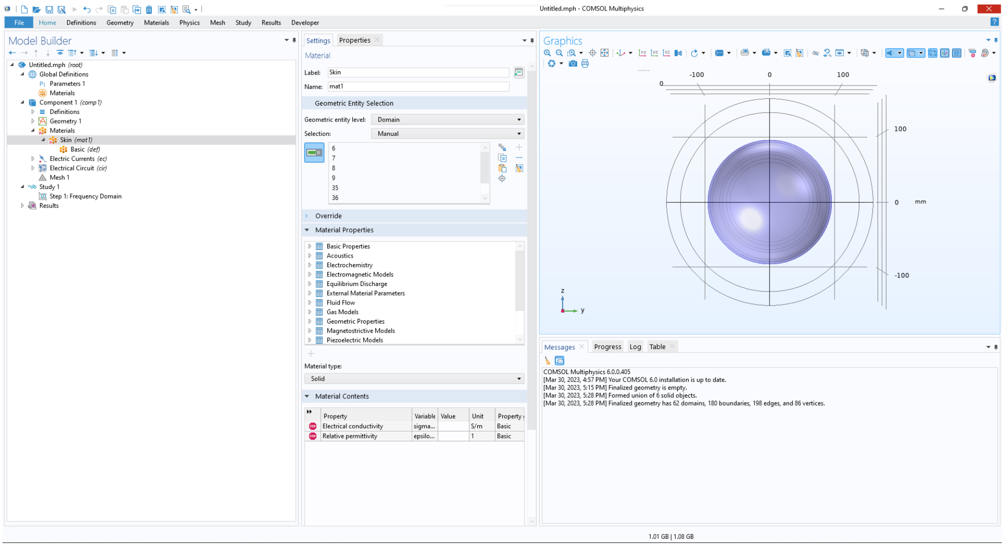

Figure A.15: STEP 15: In Model Builder right-click on Materials, then select Blank Material. In Settings tab fill Label as in the picture. In Graphics tab manually left-click on all the Domains related to the skin, i.e. the first layer of the inner Sphere. Then expand Skin (mat 1) to show Basic (def)

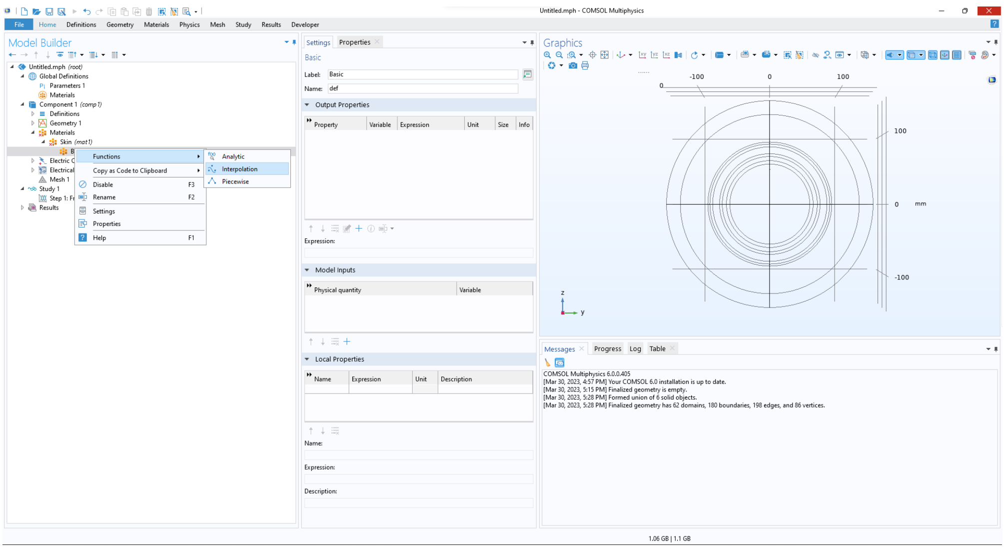

Figure A.16: STEP 16: In Model Builder right-click on Materials - Skin (mat 1) - Basic (def), then select Functions - Interpolation

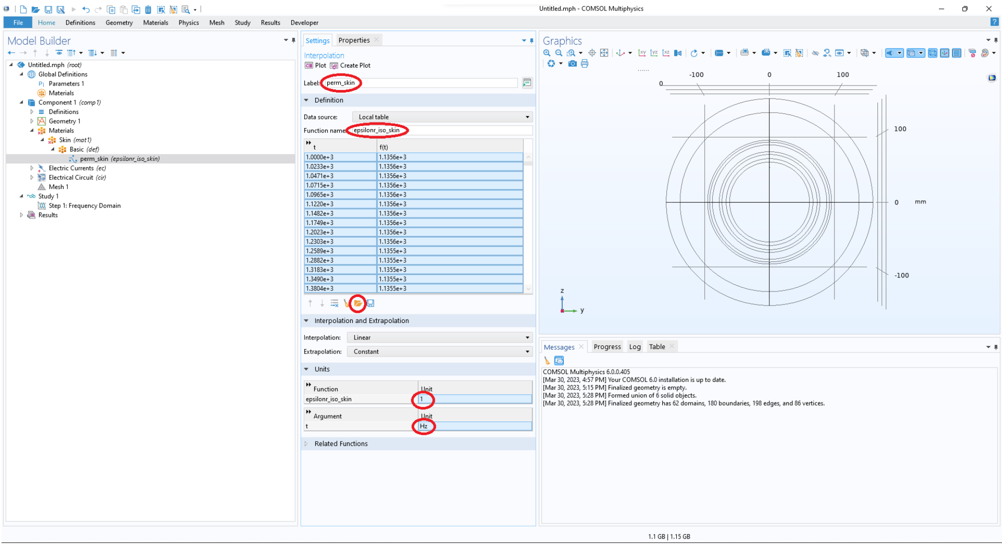

Figure A.17: STEP 17: In Settings tab fill Label, Function name, and Units as in the pictures. Then select the Folder icon under Definitions and import the .txt file with the first column indicating the frequency values, the second column the relative permittivity values related to the skin tissue

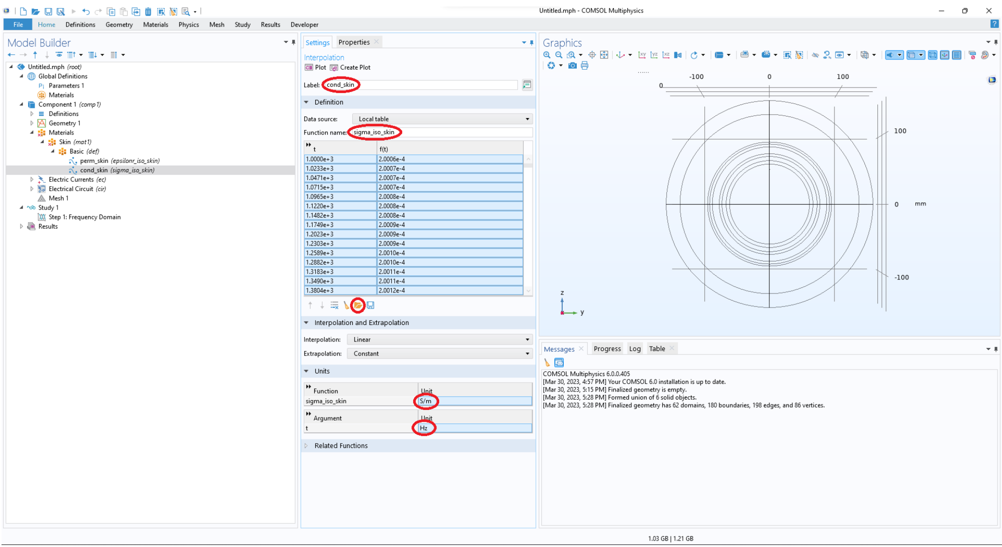

Figure A.18: STEP 18: Repeat STEP 16. In Settings tab fill Label, Function name, and Units as in the pictures. Then select the Folder icon under Definitions and import the .txt file with the first column indicating the frequency values, the second column the conductivity values related to the skin tissue

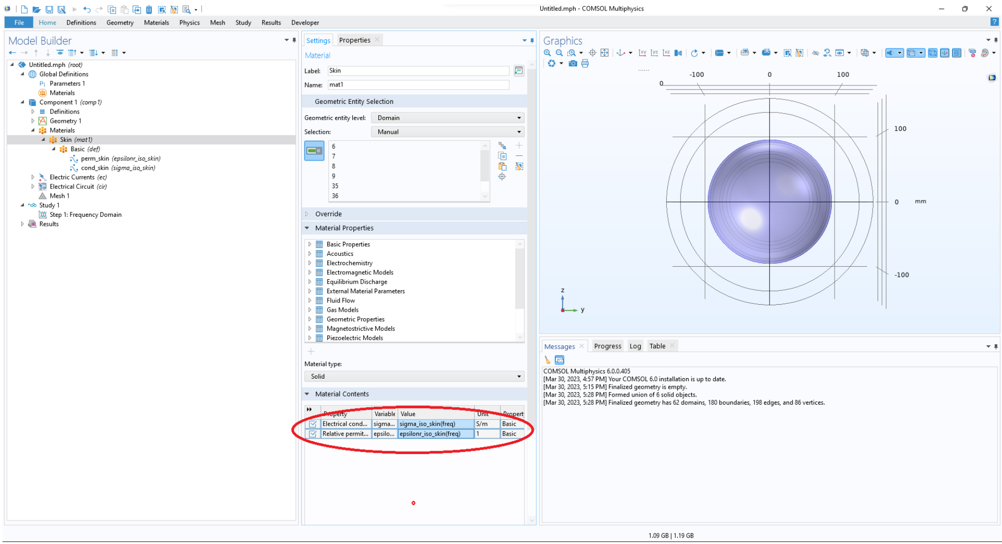

Figure A.19: STEP 19: In Model Builder select Materials - Skin (mat 1). In Settings tab fill Material Contents as in the picture

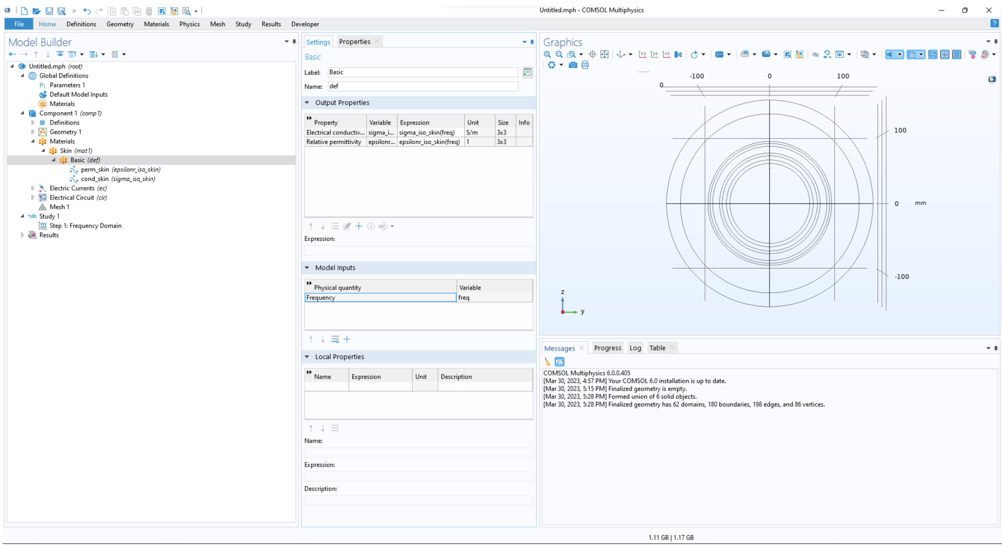

Figure A.20: STEP 20: In Model Builder select Materials - Skin (mat 1) - Basic (def). In Settings tab click on the + icon under Model Inputs, then select General - Frequency (Hz)

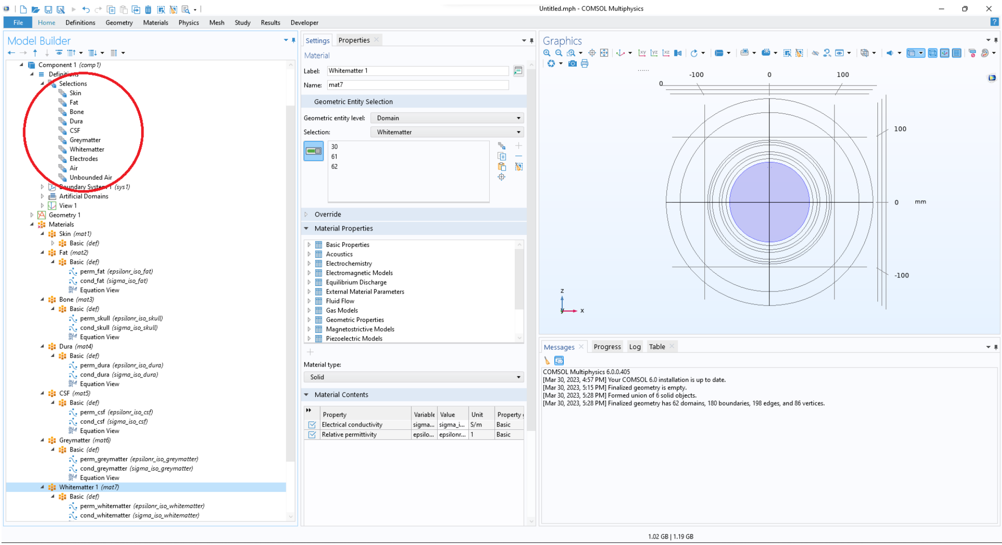

Figure A.21: STEP 21: Repeat STEPS 15-20 for all the materials related to the other tissues. An alternative to manually selecting the Domains for each of them is creating Explicit Selections under Definitions as in the picture. Then for each material, it is enough to select the relative Selection under Geometry Entity Selection

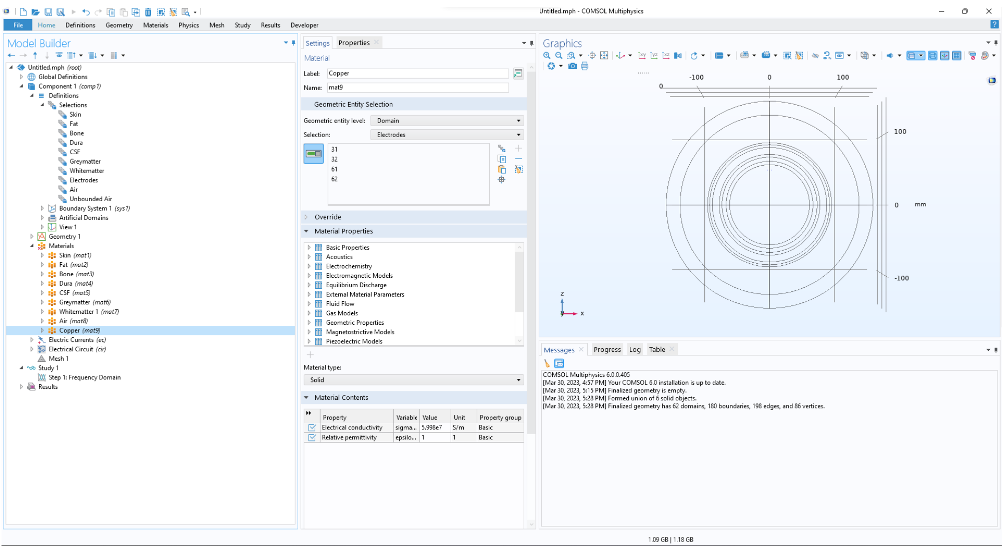

Figure A.22: STEP 22: Add two Blank Materials for Air and Copper too, filling the values of Electrical conductivity and Relative permittivity under Material Contents with 0 and 1 for Air and 5.998e7 and 1 for Copper

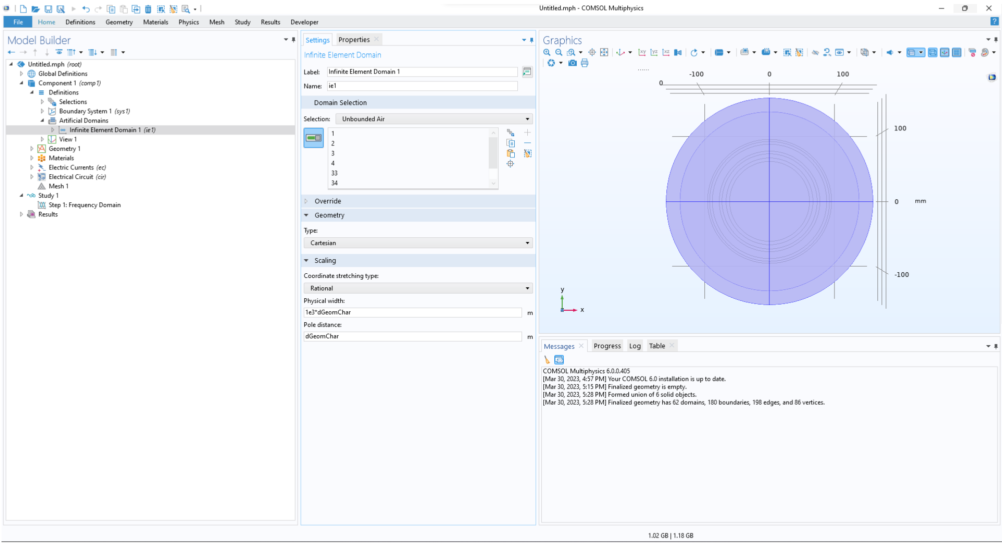

Figure A.23: STEP 23: In Model Builder select Definitions- Artificial Domains - Infinite Element Domain 1 (ie1). In Graphics tab select the Domains of the outer layer of the Air Sphere under Domain Selection, or just choose the relative selection in Settings tab

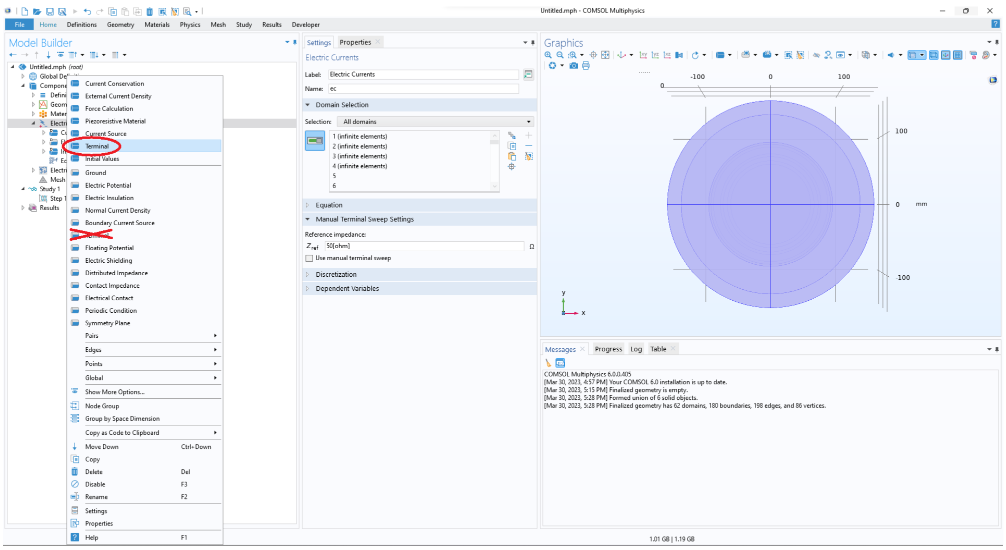

Figure A.24: STEP 24: In Model Builder right-click on Electric Currents (ec), then select the domain Terminal, and not the boundary Terminal, as in the picture

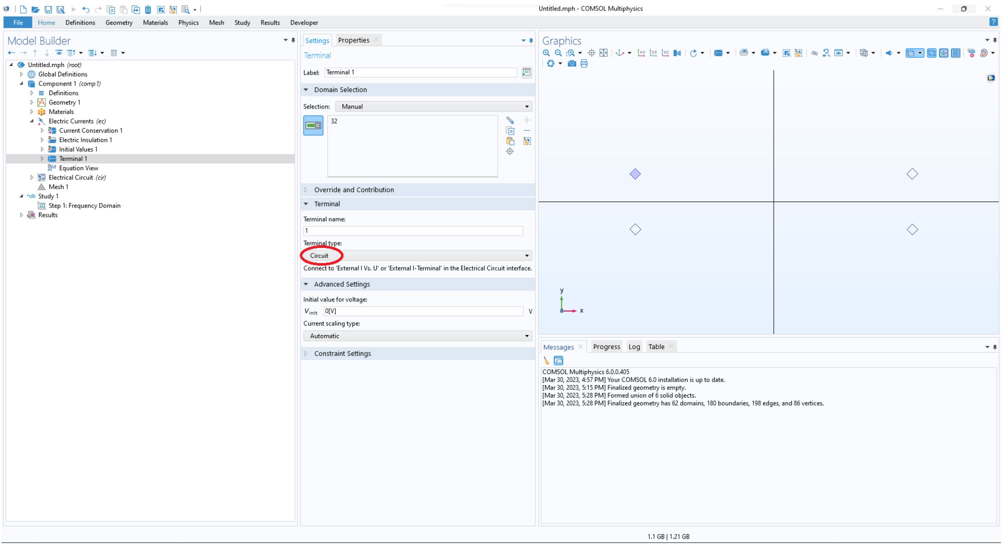

Figure A.25: STEP 25: In the Graphics tab zoom on the electrode Cylinders, then left-click on the one in the upper-left corner. Choose Circuit under Terminal type. Repeat STEPS 24-25 for the other three terminals, selecting the lower-left Cylinders for Terminal 2, the upper-right Cylinders for Terminal 3, and the lower-right Cylinders for Terminal 4

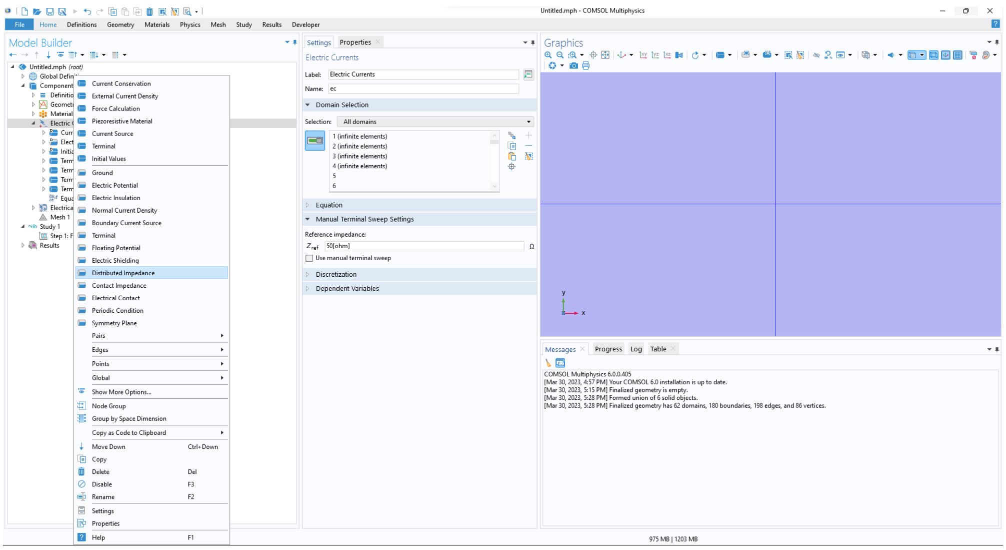

Figure A.26: STEP 26: In Model Builder right-click on Electric Currents (ec), then select Distributed Impedance

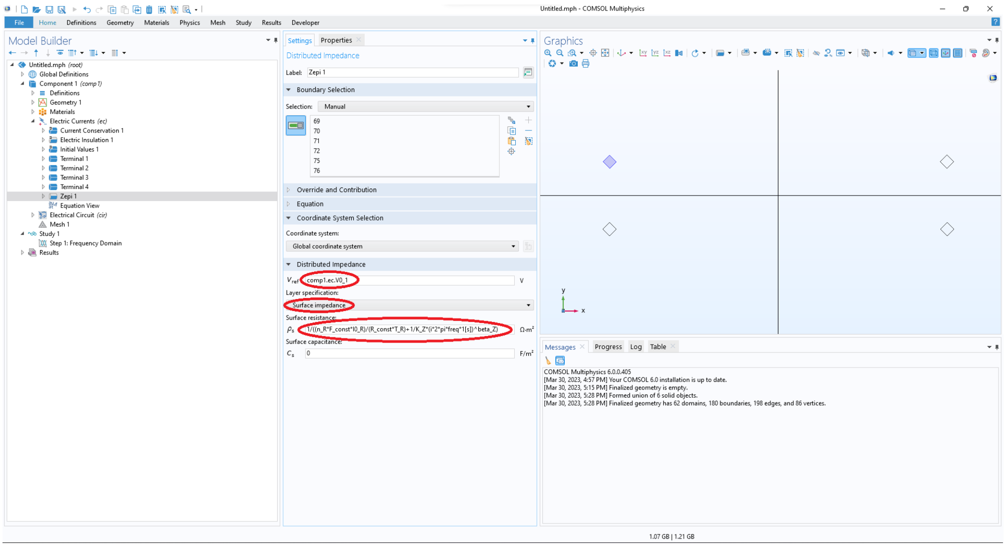

Figure A.27: STEP 27: In the Settings tab, choose Surface impedance under Layer specification, then fill Label, V$_{ref}$, and ρ_s as in the picture. In Graphics tab left-click on all the Boundaries of the Terminal 1 electrode. Repeat STEPS 26-27 for the other three terminals, increasing the value of V$_{ref}$ from comp1.ec.V0_2 to comp1.ec.V0_4 and selecting the relative Boundaries. The value of ρ_s is reported here also: 1/((n_R*F_const*I0_R)/(R_const*T_R)+1/K_Z*(i*2*pi*freq*1[s])^beta_Z)

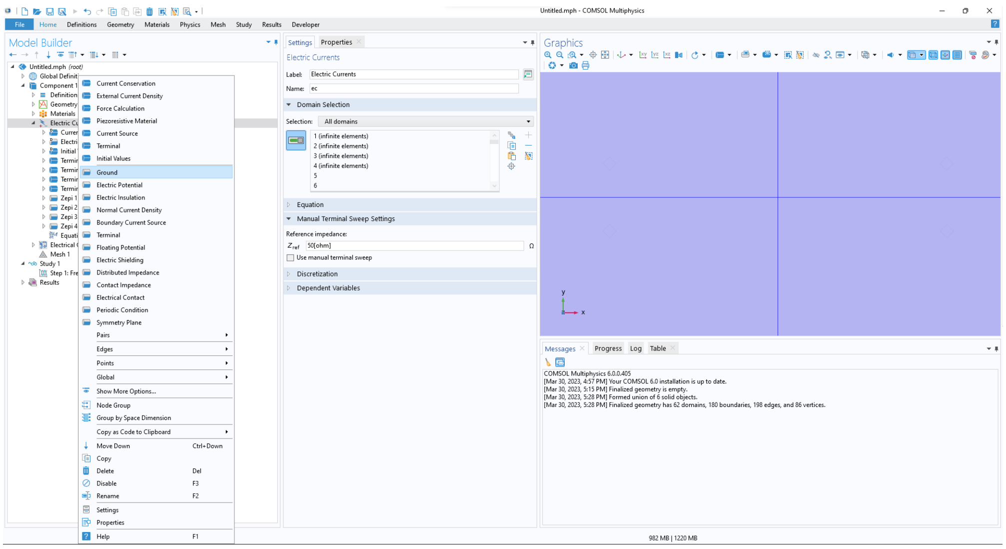

Figure A.28: STEP 28: In Model Builder right-click on Electric Currents (ec), then select Ground

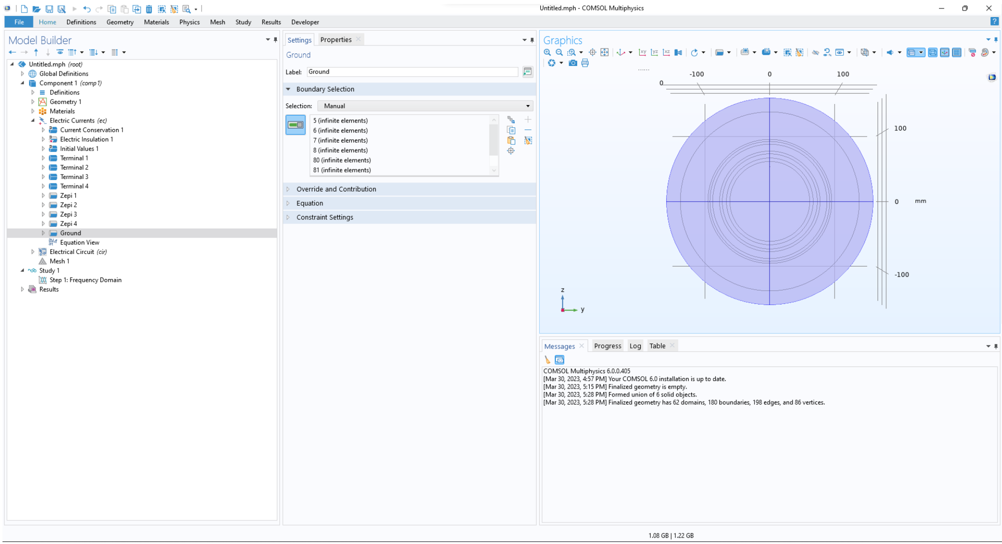

Figure A.29: STEP 29: In Graphics tab, left-clink on all the outermost Boundaries of the Air Sphere

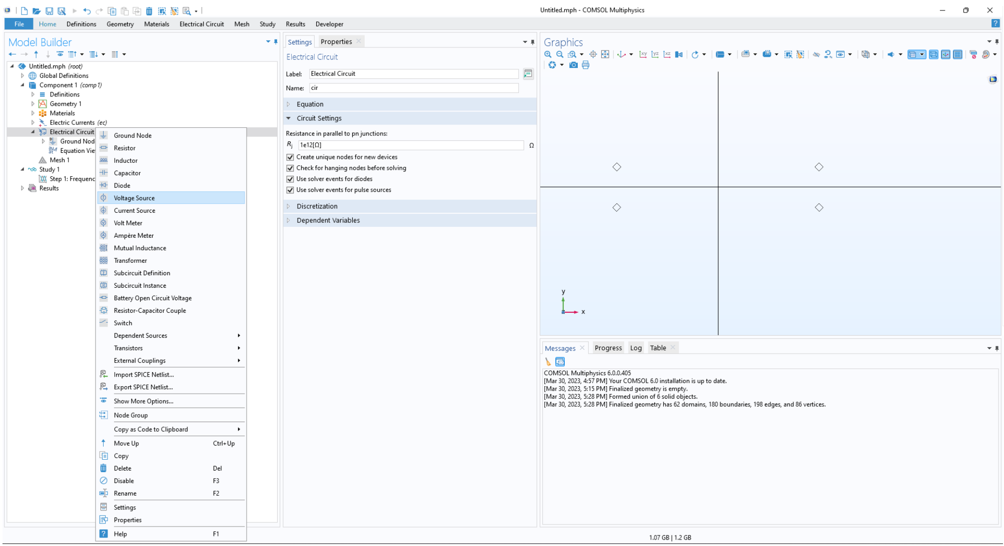

Figure A.30: STEP 30: In Model Builder right-click on Electrical Circuit (cir), then select Voltage Source

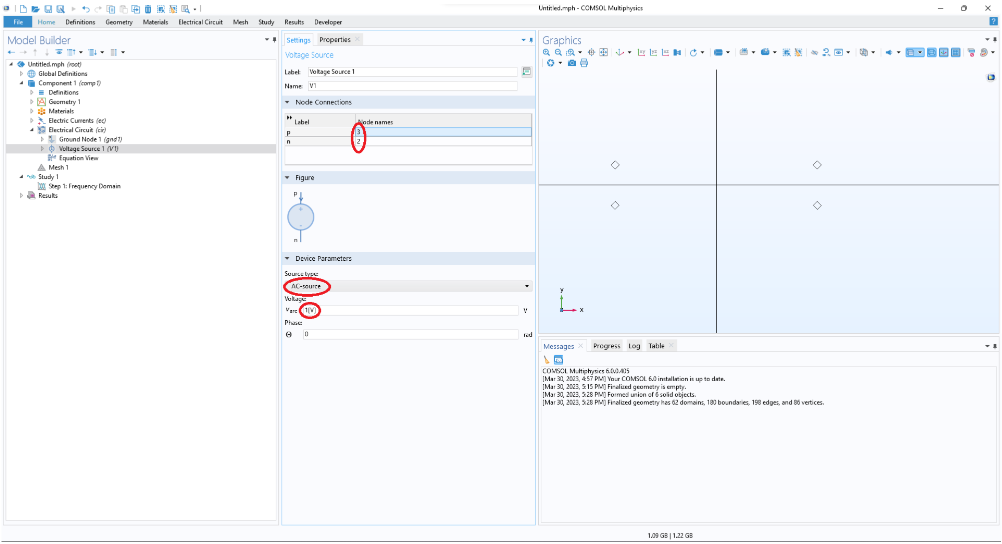

Figure A.31: STEP 31: In Settings tab choose AC-source under Source type, then fill Node Connections and Voltage as in the picture. Then add a Resistor, fill Node Connections with 3 and 1 in the p and n fields respectively, and Device Parameters with 50 in the R field

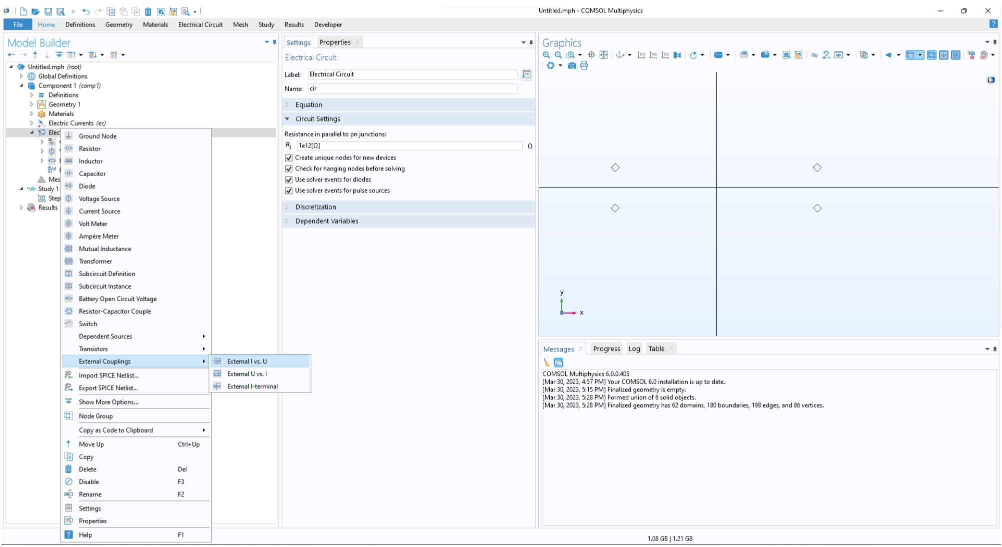

Figure A.32: STEP 32: In Model Builder right-click on Electrical Circuit (cir), then select External Couplings - External I vs. U

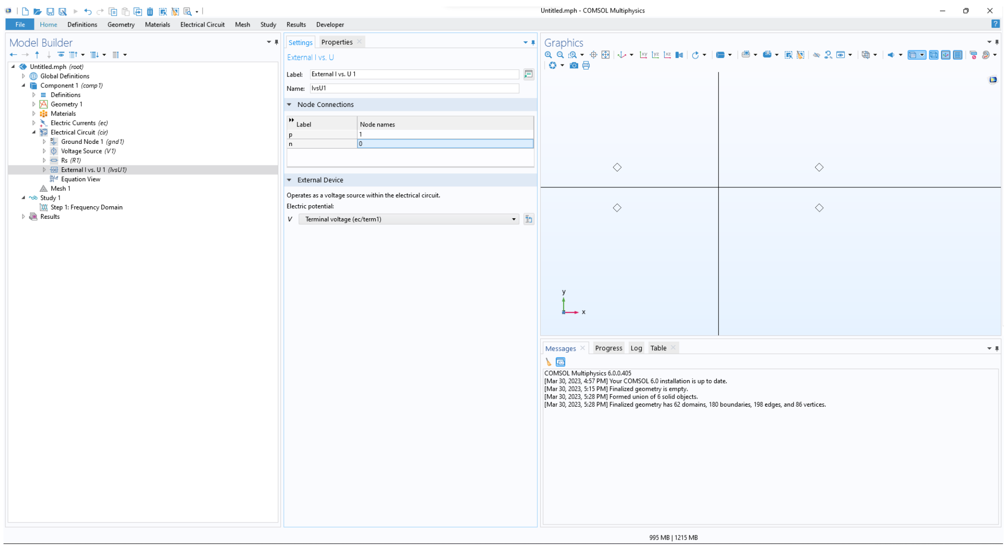

Figure A.33: STEP 33: In Settings tab fill Node Connections as in the picture and choose Terminal voltage (ec/term1) under Electric potential. Repeat STEPS 32-33, filling Node Connections with 2 and 0 in the p and n fields respectively, and choosing Terminal voltage (ec/term2) under Electric potential

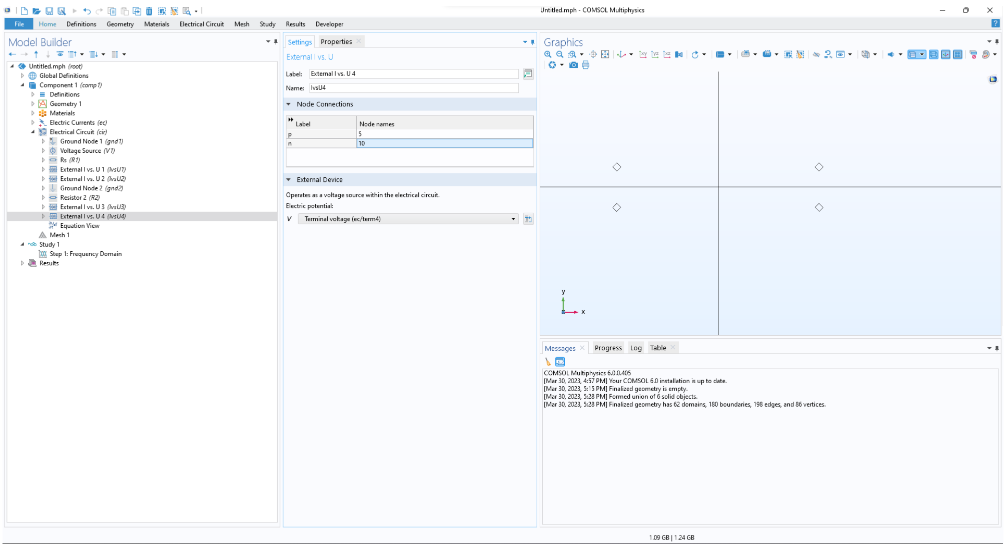

Figure A.34: STEP 34: Add another Resistor, another Groung Node, and other two External I vs. U.. In Settings tab of Ground Node 2 fill Node Connections with 10 in the p field. In Settings tab of Resistor 2 fill Node Connections with 4 and 5 in the p and n fields respectively, and Device Parameters with 50 in the R field. In Settings tab of External I vs. U. 3 fill Node Connections with 4 and 10 in the p and n fields respectively, and choose Terminal voltage (ec/term3) under Electric potential. In Settings tab of External I vs. U. 4 fill Node Connections with 5 and 10 in the p and n fields respectively, and choose Terminal voltage (ec/term4) under Electric potential

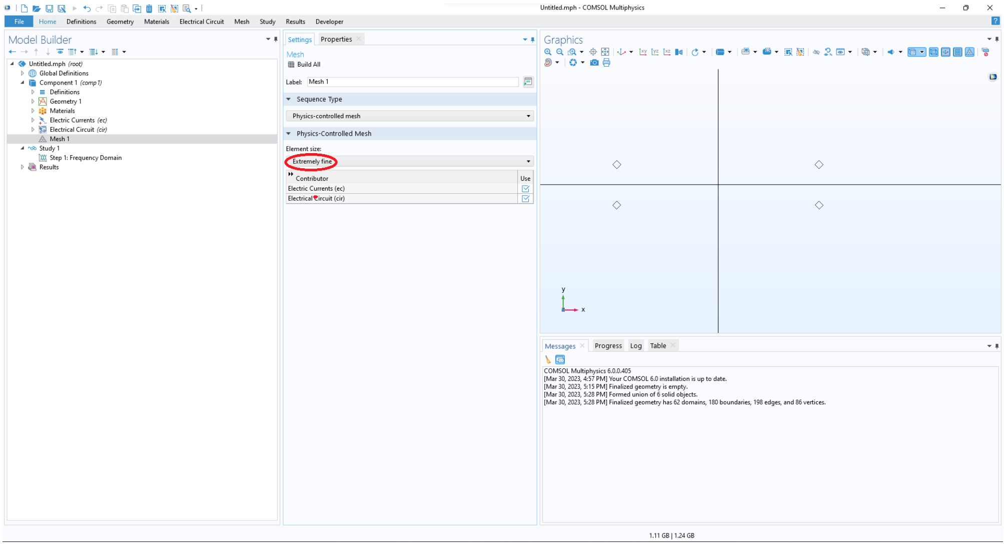

Figure A.35: STEP 35: In Model Builder select Mesh 1. Then choose Extremely fine under Element size

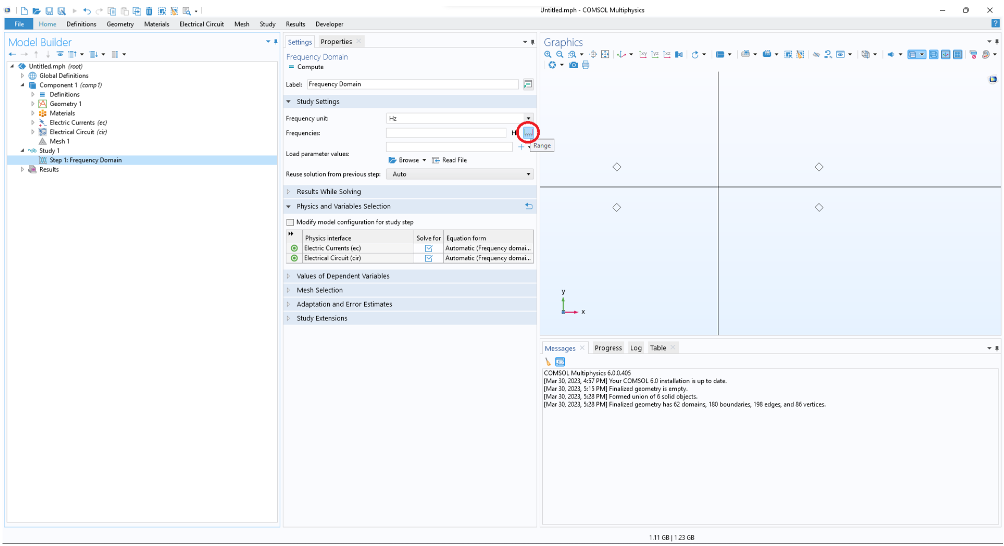

Figure A.36: STEP 36: In Model Builder select Study 1 - Step 1:Frequency Domain. In Settings tab click on the Range icon on the right of the Frequencies field as in the picture

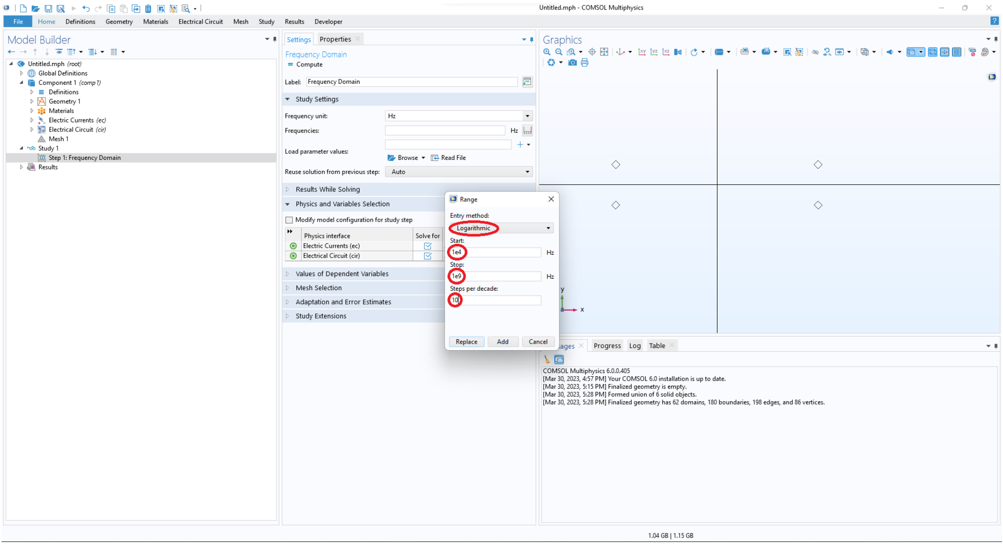

Figure A.37: STEP 37: In the Range window, choose Logarithmic under Entry method, then fill Start, Stop, and Steps per decade as in the picture

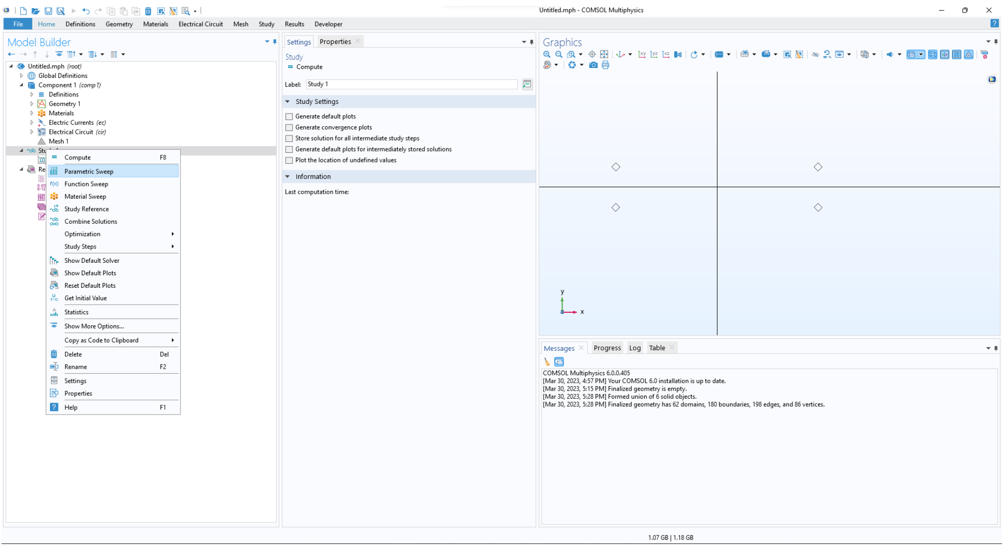

Figure A.38: STEP 38 (OPTIONAL): In Model Builder right-click on Study 1 and select Parametric Sweep

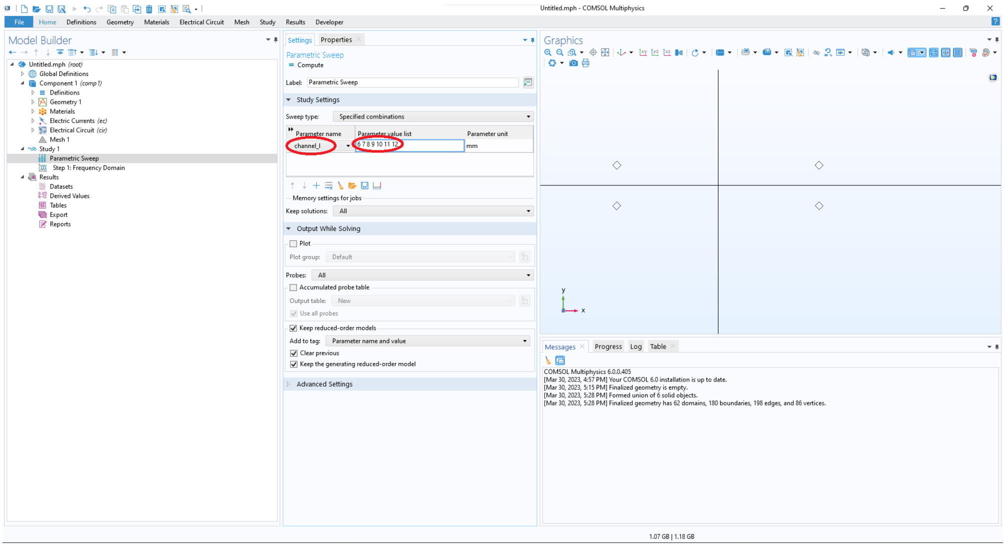

Figure A.39: STEP 39 (OPTIONAL): In Settings click the + icon under Study Settings, then choose the parameter under Parameter name and fill Parameter value list with the desired values separated by a space as in figure

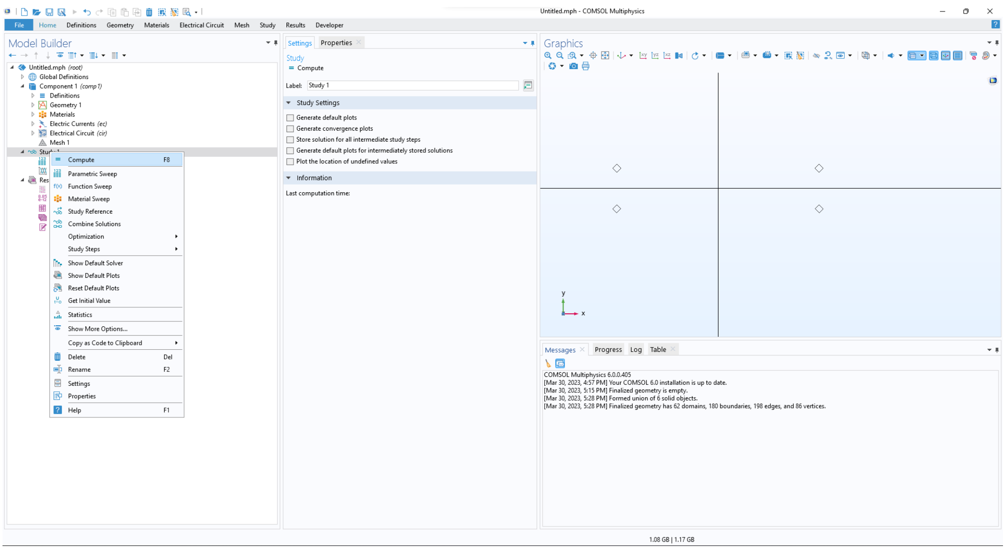

Figure A.40: STEP 40: To run the simulation in Model Builder right-click on Study 1 and select Compute

Bibliography

[1] Dongjin Seo, Jose M. Carmena, Jan M. Rabaey, Elad Alon, and Michel M. Maharbiz. «Neural Dust: an ultrasonic, low power solution for chronic brain-machine interfaces». In: (July 2013) (cit. on p. 2).

[2] Adam Khalifa, Yuxin Liu, Yasha Karimi, Qihong Wang, Adebayo Eisape, Milutin Stanaćević, Nitish Thakor, Zhenan Bao, and Ralph Etienne-Cummings. «The Microbead: a 0.009 mm3 implantable wireless neural stimulator». In: *IEEE Transactions on Biomedical Circuits and Systems* 13 (5 Oct. 2019), pp. 971–985 (cit. on p. 2).

[3] Elon Musk and Neuralink. «An integrated brain-machine interface platform with thousands of channels». In: *Journal of Medical Internet Research* 21 (10 Oct. 2019) (cit. on p. 2).

[4] Jihun Lee et al. «Neural recording and stimulation using wireless networks of microimplants». In: *Nature Electronics* 4 (8 Aug. 2021), pp. 604–614 (cit. on p. 2).

[5] Thomas Guthrie Zimmerman and Stephen A Benton. «Personal Area Networks (PAN): Near-Field Intra-Body Communication». Massachusetts Institute of Technology, 1995 (cit. on p. 4).

[6] K. Hachisuka, A. Nakata, T. Takeda, Y. Terauchi, K. Shiba, K. Sasaki, H. Hosaka, and K. Itao. «Development and performance analysis of an intra-body communication device». In: IEEE, 2003, pp. 1722–1725 (cit. on p. 5).

[7] T. Handa, S. Shoji, S. Ike, S. Takeda, and T. Sekiguchi. «A very low-power consumption wireless ECG monitoring system using body as a signal transmission medium». In: IEEE, 1997, pp. 1003–1006 (cit. on p. 5).

[8] Marc S Wegmüller. «Intra-body communication for biomedical sensor networks». ETH Zurich, 2007 (cit. on p. 5).

[9] Takayuki Ogasawara, Ai Ichiro Sasaki, Koji Fujii, Makoto Yaita, Hiroki Morimura, Yousuke Fujino, Takafumi Fujita, and Masashi Shimizu. «A circuit parameter identification of personal area networks under the magnetic coupling». In: 2012 (cit. on p. 5).

[10] C. A. Balanis. *Antenna Theory, Analysis, and Design*. 3rd. Wiley, 2005 (cit. on p. 7).

[11] Kai Zhang, Qun Hao, Yong Song, Jingwen Wang, Ruobing Huang, and Yue Liu. «Modeling and characterization of the implant intra-body communication based on capacitive coupling using a transfer function method». In: *Sensors (Switzerland)* 14 (1 Jan. 2014), pp. 1740–1756 (cit. on pp. 9–11, 15).

[12] Maoyuan Li, Yong Song, Xu Zhang, Yu Chen, and Chenqiong Tang. «A Review of Implant Intra-Body Communication». In: *Journal of Beijing Institute of Technology (English Edition)* 31 (1 Feb. 2022), pp. 1–29. ISSN: 10040579. DOI: `10.15918/j.jbit1004-0579.2021.076` (cit. on p. 10).

[13] Assefa K. Teshome, Behailu Kibret, and Daniel T.H. Lai. «Galvanically coupled intrabody communications for medical implants: a unified analytic model». In: *IEEE Transactions on Antennas and Propagation* 64 (7 July 2016), pp. 2989–3002 (cit. on p. 10).

[14] Meenupriya Swaminathan, Ferran Simon Cabrera, Joan Sebastia Pujol, Ufuk Muncuk, Gunar Schirner, and Kaushik R. Chowdhury. «Multi-path model and sensitivity analysis for galvanic coupled intra-body communication through layered tissue». In: *IEEE Transactions on Biomedical Circuits and Systems* 10 (2 Apr. 2016), pp. 339–351 (cit. on pp. 10, 11).

[15] Lukas Bereuter, Timon Kuenzle, Thomas Niederhauser, Martin Kucera, Dominik Obrist, Tobias Reichlin, Hildegard Tanner, and Andreas Haeberlin. «Fundamental Characterization of Conductive Intracardiac Communication for Leadless Multisite Pacemaker Systems». In: *IEEE Transactions on Biomedical Circuits and Systems* 13 (1 Feb. 2019), pp. 237–247 (cit. on pp. 12, 14, 16, 32, 34).

[16] Maoyuan Li, Yong Song, Yongtao Hou, Ning Li, Yurong Jiang, Muhammad Sulaman, and Qun Hao. «Comparable investigation of characteristics for implant intra-body communication based on galvanic and capacitive coupling». In: *IEEE Transactions on Biomedical Circuits and Systems* 13 (6 Dec. 2019), pp. 1747–1758 (cit. on pp. 12, 15, 16, 26, 28, 29, 34, 36, 60).

[17] Khaled M. Al-Ashmouny, Chris Boldt, John E. Ferguson, Arthur G. Erdman, A. David Redish, and Euisik Yoon. «IBCOM (Intra-Brain Communication) microsystem: Wireless transmission of neural signals within the brain». In: IEEE Computer Society, 2009, pp. 2054–2057 (cit. on p. 12).

[18] Kiyotaka Sasagawa, Takashi Matsuda, Peter Davis, Bing Zhang, Keren Li, Takuma Kobayashi, Toshihiko Noda, Takashi Tokuda, and Jun Ohta. «Wireless intra-brain communication for image transmission through mouse brain». In: 2011, pp. 2917–2920 (cit. on p. 12).

[19] Changuk Lee et al. «A Miniaturized Wireless Neural Implant With Body-Coupled Power Delivery and Data Transmission». In: *IEEE Journal of Solid-State Circuits* 57 (11 Nov. 2022), pp. 3212–3227 (cit. on p. 13).

[20] Mi Jeong Park, Taewook Kang, In Gi Lim, Kwang Il Oh, Sung Eun Kim, Jae Jin Lee, and Hyung Il Park. «Low-power, high data-rate digital capsule endoscopy using human body communication». In: *Applied Sciences (Switzerland)* 8 (9 Aug. 2018) (cit. on pp. 13, 16).

[21] Jaeeun Jang, Jihee Lee, Kyoung Rog Lee, Jiwon Lee, Minseo Kim, Yongsu Lee, Joonsung Bae, and Hoi Jun Yoo. «A four-camera VGA-resolution capsule endoscope system with 80-Mb/s body channel communication transceiver and sub-centimeter range capsule localization». In: *IEEE Journal of Solid-State Circuits* 54 (2 Feb. 2019), pp. 538–549 (cit. on p. 13).

[22] Vivek Y. Reddy et al. «Permanent Leadless Cardiac Pacing». In: *Circulation* 129 (14 Apr. 2014), pp. 1466–1471 (cit. on p. 13).

[23] Ali Khaleghi, Reza Noormohammadi, and Ilangko Balasingham. «Conductive impulse for wireless communication in dual-chamber leadless pacemakers». In: *IEEE Transactions on Microwave Theory and Techniques* 69 (1 Jan. 2021), pp. 443–451 (cit. on pp. 13, 16).

[24] Nicolas Fahier and Wai-Chi Fang. «An HBC-based continuous bio-potential system monitoring using 30MHz OOK modulation». In: 2017 (cit. on p. 14).

[25] Nicolas Fahier, Cheng Jie Yang, and Wai Chi Fang. «Wearable cardiovascular monitoring system design using human body communication». In: vol. 2021-May. Institute of Electrical and Electronics Engineers Inc., 2021 (cit. on pp. 14, 16).

[26] William J. Tomlinson, Stella Banou, Shay Blechinger-Slocum, Christopher Yu, and Kaushik R. Chowdhury. «Body-guided galvanic coupling communication for secure biometric data». In: *IEEE Transactions on Wireless Communications* 18 (8 Aug. 2019), pp. 4143–4156 (cit. on pp. 14, 16).

[27] Wangwang Zhu, Taogeng Zhou, Ya Zhou, Maoyuan Li, Yu Chen, Yufei Zhao, and Yong Song. «An audio transmission system based on capacitive coupling intra-body communication». In: Institute of Electrical and Electronics Engineers Inc., May 2021, pp. 183–187 (cit. on p. 14).

[28] Stella Banou, Meenupriya Swaminathan, Guillem Reus Muns, Davy Duong, Farzana Kulsoom, Pietro Savazzi, Anna Vizziello, and Kaushik R. Chowdhury. «Beamforming galvanic coupling signals for IoMT implant-to-telay communication». In: *IEEE Sensors Journal* 19 (19 Oct. 2019), pp. 8487–8501 (cit. on pp. 14, 17).

[29] Reza Noormohammadi, Ali Khaleghi, and Ilangko Balasingham. «Galvanic Impulse Wireless Communication for Biomedical Implants». In: *IEEE Access* 9 (2021), pp. 38602–38610 (cit. on p. 14).

[30] Chengyao Shi, Minyoung Song, Zhenyu Gao, Andrea Bevilacqua, Guido Dolmans, and Yao Hong Liu. «Galvanic-coupled trans-dural data transfer for high-bandwidth intracortical neural sensing». In: *IEEE Transactions on Microwave Theory and Techniques* 70 (10 Oct. 2022), pp. 4579–4589 (cit. on pp. 15, 16, 29, 48).

[31] COMSOL Multiphysics$^{\text{ő}}v$.6.0. *AC/DC Module User's Guide*. COMSOL AB, Stockholm, Sweden. 2022, pp. 37–38 (cit. on p. 18).

[32] D. Andreuccetti, R. Fossi, and C. Petrucci. *An Internet resource for the calculation of the dielectric properties of body tissues in the frequency range 10 Hz - 100 GHz*. 1997. URL: `http://niremf.ifac.cnr.it/tissprop/` (cit. on p. 18).

[33] Yue Ming Gao et al. «Electrical exposure analysis of galvanic-coupled intra-body communication based on the empirical arm models». In: *BioMedical Engineering Online* 17 (1 June 2018) (cit. on p. 19).

[34] Shovan Maity, Mayukh Nath, Gargi Bhattacharya, Baibhab Chatterjee, and Shreyas Sen. «On the Safety of Human Body Communication». In: *IEEE Transactions on Biomedical Engineering* 67 (12 Dec. 2020), pp. 3392–3402 (cit. on p. 19).

[35] ICNIRP. «Guidelines for limiting exposure to time-varying electric, magnetic, and electromagnetic fields (up to 300 GHz)». In: *Health Physics* 74 (4 1998), pp. 494–522 (cit. on p. 19).

[36] ICNIRP. «Guidelines for limiting exposure to time-varying electric and magnetic fields (1 Hz to 100 kHz)». In: *Health Physics* 99 (6 Dec. 2010), pp. 818–836 (cit. on pp. 19–21).

[37] ICNIRP. «Guidelines for limiting exposure to electromagnetic fields (100 kHz to 300 GHz)». In: *Health Physics* 118 (5 May 2020), pp. 483–524 (cit. on pp. 19–21).

[38] S Gabriel, R W Lau, and C Gabriel. *The dielectric properties of biological tissues: III. Parametric models for the dielectric spectrum of tissues*. 1996, pp. 2271–2293 (cit. on pp. 25, 26).

[39] PA Hasgall, F Di Gennaro, C Baumgartner, E Neufeld, B Lloyd, MC Gosselin, D Payne, A Klingenböck, and N Kuster. *IT'IS Database for thermal and electromagnetic parameters of biological tissues*. 2022. URL: `itis.swiss/database` (visited on 03/13/2023) (cit. on pp. 26, 55).

[40] Robert Plonsey and Dennis B Heppner. «Considerations of quasi-stationarity in electrophysiological systems». In: *Bullettin Of Mathematical Biophysics* 29 (1967), pp. 657–664 (cit. on p. 26).

[41] M. Amparo Callejon, Javier Reina-Tosina, David Naranjo-Hernandez, and Laura M. Roa. «Galvanic coupling transmission in intrabody communication: A finite element approach». In: *IEEE Transactions on Biomedical Engineering* 61 (3 Mar. 2014), pp. 775–783 (cit. on p. 31).

[42] A. Richardot and E. T. McAdams. «Harmonic analysis of low-frequency bioelectrode behavior». In: *IEEE Transactions on Medical Imaging* 21 (6 2002), pp. 604–612 (cit. on pp. 32, 33).

[43] Larryisgood. URL: `https://commons.wikimedia.org/w/index.php?curid=17639292` (visited on 04/06/2023) (cit. on p. 33).

[44] Donald R. Cantrell, Samsoon Inayat, Allen Taflove, Rodney S. Ruoff, and John B. Troy. «Incorporation of the electrode-electrolyte interface into finite-element models of metal microelectrodes». In: *Journal of Neural Engineering* 5 (1 Mar. 2008), pp. 54–67 (cit. on p. 33).